

FINAL REPORT

Grant Number:
DAAL03-86-K-0145

Principal Investigator:
R. LHERMITTE

Project Title:
REMOTE SENSING USING A GROUND BASED 94 GHZ RADAR

**Best
Available
Copy**

REPORT DOCUMENTATION PAGE			Form Approved OMB No. 0704-0188	
Public reporting burden for this collection of information is estimated to average 1 hour per response, including the time for reviewing instructions, searching existing data sources, gathering and maintaining the data needed, and completing and reviewing the collection of information. Send comments regarding this burden estimate or any other aspect of this collection of information, including suggestions for reducing this burden, to Washington Headquarters Services, Directorate for Information Operations and Reports, 1215 Jefferson Davis Highway, Suite 1204, Arlington, VA 22202-4302 and to the Office of Management and Budget, Paperwork Reduction Project (0704-0188), Washington, DC 20503.				
1. AGENCY USE ONLY (Leave blank)	2. REPORT DATE 5 Sept 1991	3. REPORT TYPE AND DATES COVERED Final 15 Aug 86-24 Aug 90		
4. TITLE AND SUBTITLE Remote Sensing Using a Ground Based 94GHz Doppler Radar			5. FUNDING NUMBERS DAAL03-86-K-0145	
6. AUTHOR(S) R. Lhermitte				
7. PERFORMING ORGANIZATION NAME(S) AND ADDRESS(ES) University of Miami 4600 Rickenbacker Causeway Miami, Florida 33149-1098			8. PERFORMING ORGANIZATION REPORT NUMBER	
9. SPONSORING/MONITORING AGENCY NAME(S) AND ADDRESS(ES) U. S. Army Research Office P. O. Box 12211 Research Triangle Park, NC 27709-2211			10. SPONSORING/MONITORING AGENCY REPORT NUMBER ARO 24062.5-GS	
11. SUPPLEMENTARY NOTES The view, opinions and/or findings contained in this report are those of the author(s) and should not be construed as an official Department of the Army position, policy, or decision, unless so designated by other documentation.				
12a. DISTRIBUTION/AVAILABILITY STATEMENT Approved for public release; distribution unlimited.			12b. DISTRIBUTION CODE	
13. ABSTRACT (Maximum 200 words) The original purpose of this research was to explore the usefulness and performance of a 94 GHz pulse Doppler radar for the remote sensing of clouds and precipitation. The approach was first to design and assemble a 94 GHz Doppler radar. Then observations of clouds and precipitation with that radar were conducted along with the interpretations of the observational data in an effort to make contributions toward a better understanding of the physics and dynamics of clouds and precipitation systems.				
14. SUBJECT TERMS			15. NUMBER OF PAGES	
			16. PRICE CODE	
17. SECURITY CLASSIFICATION OF REPORT UNCLASSIFIED	18. SECURITY CLASSIFICATION OF THIS PAGE UNCLASSIFIED	19. SECURITY CLASSIFICATION OF ABSTRACT UNCLASSIFIED	20. LIMITATION OF ABSTRACT UL	

Final report Grant No DAAL03-86-K-0145

Principal Investigator: R. Lhermitte, University of Miami

Project title:

REMOTE SENSING USING A GROUND BASED 94 GHZ RADAR

1. INTRODUCTION

The original purpose of this research was to explore the usefulness and performance of a 94 GHz pulse Doppler radar for the remote sensing of clouds and precipitation. The approach was first to design and assemble a 94 GHz Doppler radar. Then observations of clouds and precipitation with that radar were conducted along with the interpretation of the observational data in an effort to make contributions toward a better understanding of the physics and dynamics of clouds and precipitation systems.

This project was originally based on the design and fabrication of the 94 GHz Doppler radar as well as the implementation of hardware and software methods for Doppler radar signal processing. This was initiated under a previous contract but, during the contract period covered by this report, the radar was substantially modified and upgraded.

Also, in order to place the 94 GHz radar in proper perspective, theoretical calculations of radar reflectivity and attenuation coefficient under various cloud and precipitation conditions were performed for radar frequencies ranging from 35 GHz to 240 GHz.

The field experiments were all conducted with the ground-based 94 GHz radar operated in a vertically pointing beam mode. The meteorological events observed with the radar were: cirrus clouds, fair weather cumuli and stratiform and convective rain. The data acquired with the radar were: vertical profiles of radar reflectivity, vertical profiles of mean Doppler velocity and occasionally Doppler spectra observed at vertical incidence.

This research was concerned solely with ground based atmospheric measurements. However, the experience acquired in gathering and analyzing

millimeter wave radar observations presented the opportunity to explore the capabilities and feasibility of a millimeter wave radar installed on an orbiting satellite platform for the purpose of remote sensing of earth cloud and precipitation.

The ARO supported research yielded more than ten published articles which are listed at the end of the report and numbered so that they can be used as references in this writing which essentially summarizes various aspects of the results. A copy of some of these articles is attached to this report. Reprints of any of the remaining papers is available on request.

2. RADAR AND SIGNAL PROCESSING

The radar, which was developed in-house using commercially available parts, is described in details in [1], [2], [3], and [5]. The first version was based on the use of two antennae, one for transmitting and the other for receiving. It was more recently redesigned to accommodate one antenna, using a circulator and two crystal protector switches along with pulse timing circuits designed and implemented for that purpose.

The main characteristics of the radar are:

- Peak power: 1.2 kW
- Pulse width is adjustable, but 400 ns and 100 ns were selected for vertical profiles and high resolution Doppler spectra, respectively.
- Pulse repetition rate: 10 kHz for all measurements reported here.
- Receiver noise: 6.5 db DSB noise figure
- Antenna: 90 cm cassegrain
- Doppler method: Coherent-on-receive
- Doppler signal processing: Pulse-Pair and FFT
- Minimum detectable reflectivity at 2 km with 3 s signal dwell time: -50 dBZ

The radar receiver circuits include an orthomode transducer yielding two separate orthogonal polarization channels. The transmitted pulse signal polarization is horizontal.

The radar sensitivity is expressed by the following equation:

$$10\log\eta = 10\log P_r - 10\log P_t + 10\log 4\pi R^2 - 10\log h - 10\log A_e \quad (1)$$

where η is the radar reflectivity, P_r is the received power, P_t is the transmitted peak power, h is the scattering volume radial dimension, A_e is the effective area of the receiving antenna, and R is the target distance. With the radar characteristics above, $h = 60m$ (400 ns pulse), and a 3.5 dB antenna efficiency correction, we have:

$$10\log\eta = P_r(\text{dbm}) - 23.5 + 20\log R \quad (2)$$

Or, in dBZ:

$$\text{dBZ} = P_r(\text{dBm}) + 53 + 20\log R \quad (3)$$

At a 3km range, a cloud reflectivity of -33 dBZ yields a signal equal to receiver noise. With a signal integration time of 3s, a radar reflectivity less than -50 dBZ can be measured. Presentation and discussion of the radar sensitivity parameters and the radar's ability to detect very small clouds can be found in more detail in [5], [6], [7], [8], [9].

The signal processing system includes a hardwired signal amplitude integrator and a hardwired Pulse Pair [8] processor delivering mean Doppler estimates. The system was designed to process and record mean signal intensity and mean Doppler at 250 gates spaced by 400 ns, thus covering a 15km range (altitude for vertically pointing). The mean Doppler and mean signal intensity data were processed and displayed in a format suitable for analysis (i.e. vertical profiles) using a PC/AT assigned to the project and equipped with a plotter.

A unit digitally recording the I and Q signals at 16 selected gates simultaneously was later added to the radar data acquisition system. This unit allows continuous digitization and recording on half-inch magnetic tape (1600 bpi), of 8192 samples simultaneously at each of 16 selected range gates. The minimum gate spacing is $0.1 \mu s$, which is equivalent to a range interval of 15 m. At the 10 kHz pulse repetition rate, the recording time (including data acquisition overhead) is approximately 1 s and a new set of 16 gates data (possibly automatically shifted to cover a greater range



For	
AI	<input checked="" type="checkbox"/>
ed	<input type="checkbox"/>
tion	<input type="checkbox"/>

by _____	
Distribution/	
Availability Codes	
Dist	Avail and/or Special
A-1	

interval) is acquired at approximately 2 s time intervals. Doppler spectra were calculated off line from the recorded samples with a PC/AT in which software developed FFT algorithms were implemented. An example of the excellent range resolution allowed by the method can be seen in [12, Fig.7].

3. ATTENUATION AND BACKSCATTERING OF MILLIMETER WAVE RADIATION BY CLOUD AND PRECIPITATION

The absorption and scattering of millimeter wave radiation by hydrometeors was investigated in an effort to provide the general background needed for meteorological interpretation of the 94 GHz radar observations. These investigations were also used for a comparison between the performance of the 94GHz radar and that of other radars using different wavelengths in the millimeter wave part of the spectrum. This work is presented and discussed in [15] and the following is a summary of the approach and results.

Only spherical droplets or raindrops (also spherical hailstones) were considered so that the absorption, scattering, and backscattering cross sections of these targets could be computed using the classical Mie functions. This was done for water and ice and for a particle diameter ranging from 10 μ m to a large raindrop size (6 mm diameter) and at selected frequencies between 35 to 240 GHz. The water and ice index of refraction data which were required for these computations, were determined from previously published results (see [15]). An example of the Mie backscattering calculations at 94 GHz is shown in Fig.1.

In order to apply these calculations to rainfall, a Marshall-Palmer raindrop size distribution was assumed. This together with the theoretically expressed Mie functions and a raindrop terminal velocity vs diameter function determined in an analytical form, allowed the determination of relationships between precipitation and millimeter wave radar observed parameters.

More precisely, absorption and scattering coefficients as well as radar reflectivity calculations were performed for precipitation of various intensity and related to rainfall rate or rain liquid water content. This included theoretical evaluation of Doppler spectra observed in various precipitation conditions at vertical incidence. The results are reported in detail in [15].

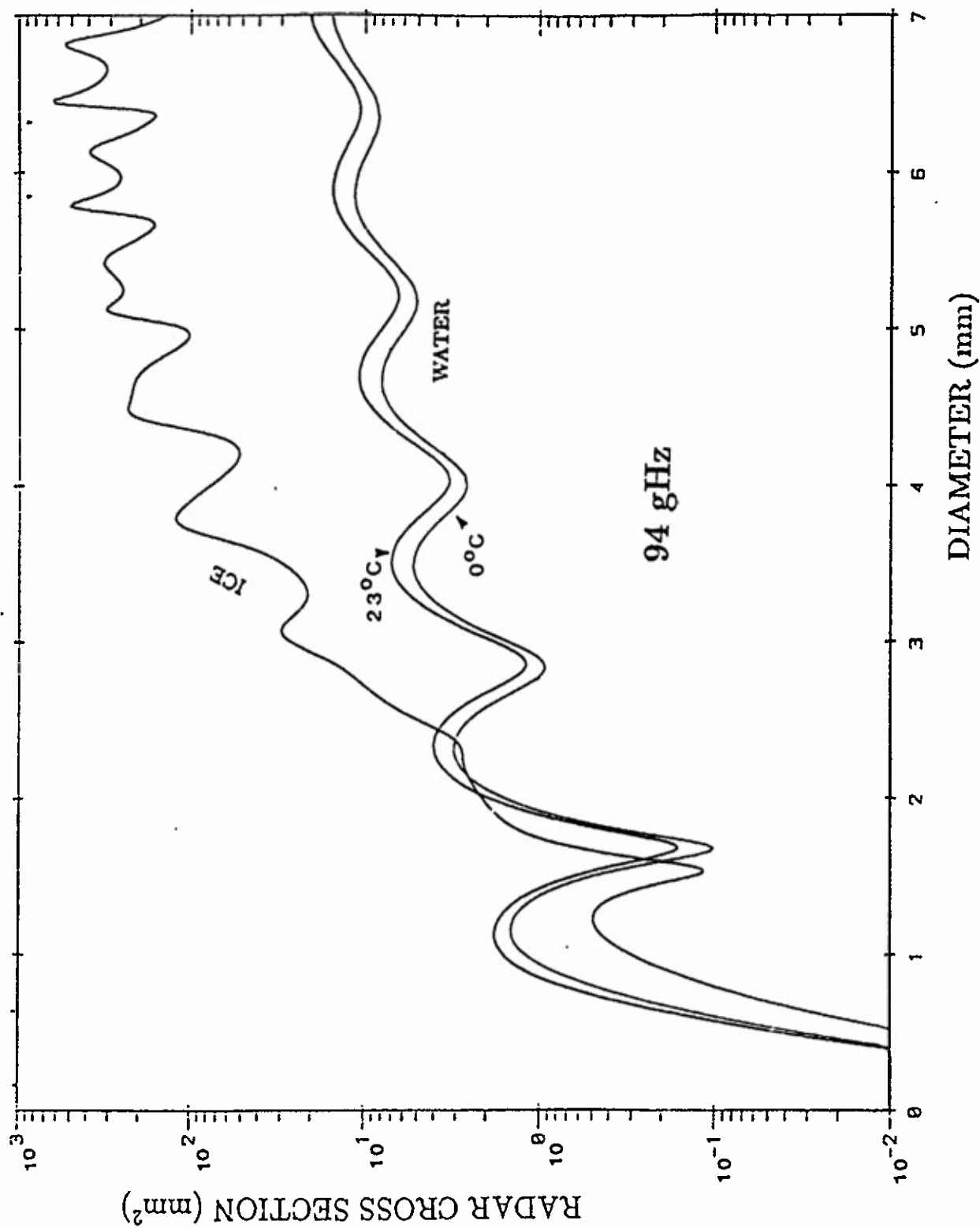


Fig. 1. Backscattering across section of water (0° and 23° C temperature) and ice spheres as a function of diameter. Frequency is 94 GHz.

4. OBSERVATION OF FAIR WEATHER CUMULI

Observing fair weather cumuli with the radar revealed its unique capability to map both the cloud's radar reflectivity (down to a -50 dBz detection threshold) and the mean Doppler velocity (beam vertical incidence) which, in that case of very low droplets' terminal velocity, can be identified with air vertical velocity (updrafts or downdrafts). These observations are presented and discussed in [9] and [11].

Observing these clouds with a vertically pointing beam yields vertical profiles of radar reflectivity and vertical velocity continuously observed during the cloud passage overhead. If there is no time evolution of the fields when the cloud is passing overhead, the variation of mean Doppler or radar reflectivity from one profile to the next only relates to the fixed radar beam intersecting different parts of the cloud due to the cloud motion. If the cloud translation speed, \bar{u} , is known, the time coordinate can thus be replaced by a space coordinate $x = \bar{u}t$. If the cloud is passing overhead with the fixed radar beam going through the cloud center, a representative vertical cross section of intra-cloud radar reflectivity and vertical velocity fields can be obtained. When conducting the cloud observations, we were fortunate to find that these conditions were met on certain occasions. Observations acquired in this manner are presented and discussed in [5] and [11].

Examples of the results are illustrated in Figs.2a and 2b. The radar reflectivity field is shown in Fig. 1a. The maximum reflectivity is -31 dBZ and the minimum detectable reflectivity -52 dBZ. There is a sharply defined cloud top due to a temperature inversion clearly indicated by the radiosonde data acquired that day. The cloud base, however, is not as well defined and exhibits a noticeable variability.

Inspection of the vertical velocity field cross section observed with the radar, which is shown in Fig.2b, reveals the presence of a strong updraft region (maximum updraft velocity 3 ms^{-1}). Comparing the velocity and the radar reflectivity fields indicates that the bulk of the updraft is just below (and slightly lagging in time) a region of high radar reflectivity, although the downdrafts are always in a region of very low radar reflectivity. The main updraft location coincides with a local rising of the cloud top (working against the temperature inversion lid), although the downdrafts are associated with a local lowering of the cloud bottom that can considerably distort the cloud base.

Maximum liquid water concentration in the cloud can be estimated

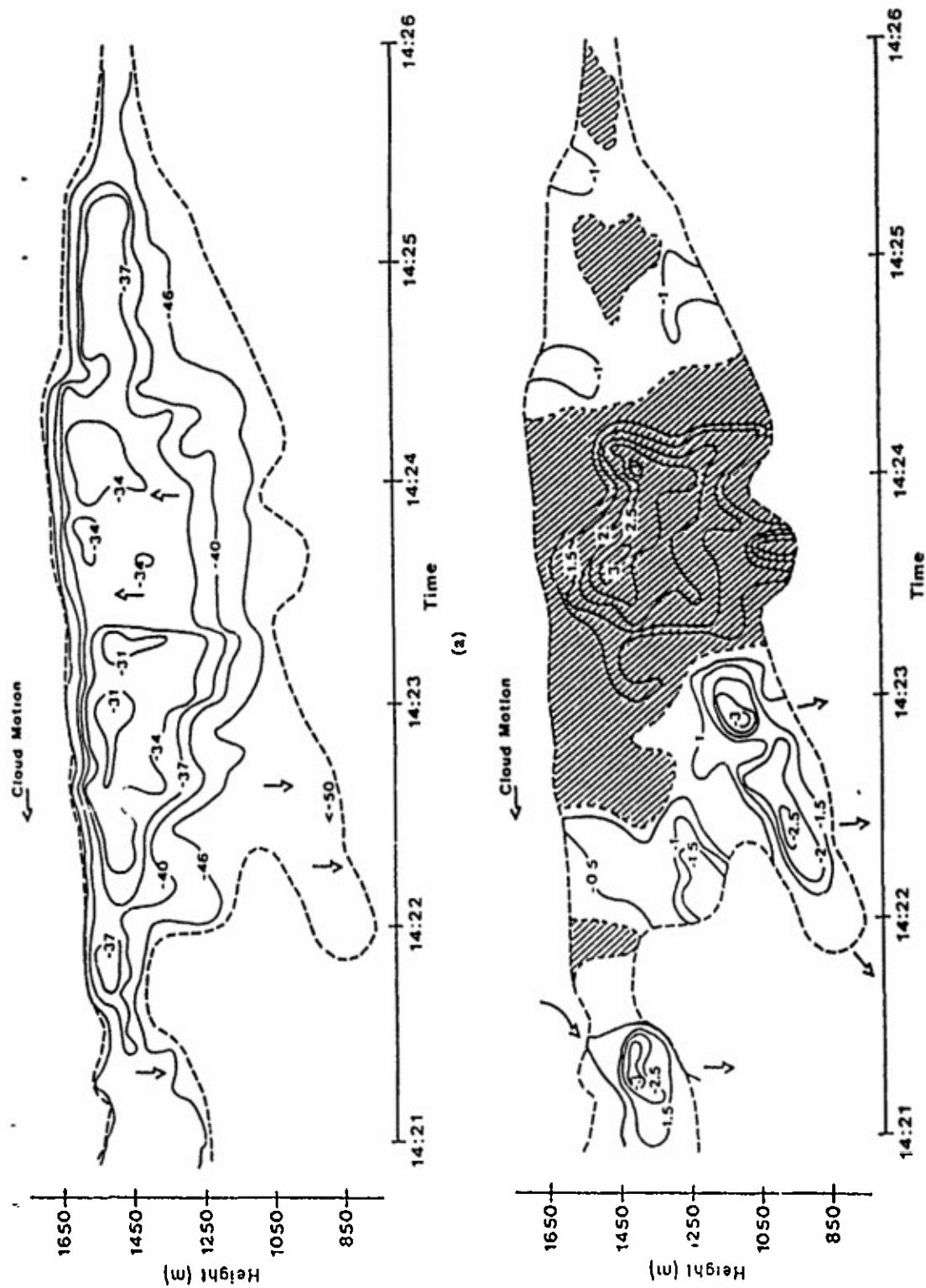


Fig. 2. (a) January 24, 1987 time-height presentation of radar reflectivity in dBZ observed in a small cumulus passing overhead. The cloud top is strongly limited by a capping inversion. Time is EDT. The cloud is moving at 10 ms^{-1} so that 1 min is equivalent to 600 m. (b) Same as (a) but for vertical air velocity. The dashed area indicates updraft regions. Updrafts tend to push the cloud top and downdrafts to lower the cloud base.

from radar reflectivity assuming a droplet size distribution function, or its general shape and a droplet size median diameter D_o . Simplifying further by assuming that all the droplets have the same diameter D_o provides a fairly representative estimate of the relationship between radar reflectivity and cloud liquid water, M (in gm^{-3}). In these conditions, we have: $M = 0.52D_o^3Z$. Assuming $D_o \simeq 10\mu m$ and applying the above relationship to the maximum radar reflectivity observed in the cloud ($\simeq -30dBZ$), indicates that the cloud liquid water in the vicinity of the cloud center in a region of maximum updraft is approximately $0.5 gm^{-3}$.

The fair weather cloud observations presented above, which are more extensively discussed in [5] and [11], have not been yet duplicated in any other radar experiment. Our results indicate that such new data can be very useful in the modelling of boundary layer "fair weather" cloud circulation and possibly their dynamics and physics if radiosonde and airplane measurements yielding observations of the cloud's environment are included in the project.

5. OBSERVATIONS OF HIGH ALTITUDE CIRRUS

Cirrus clouds were systematically observed with the millimeter wave radar. Nearly all high altitude clouds seen by the naked eye are detected and their radar reflectivity was found to be between approximately $\simeq -35dBZ$ (minimum detectable signal at a 10 km range) and $\simeq 0 dBZ$. The mean Doppler velocity was always observed and some of these observations revealed the presence of strong upward and downward velocities (possibly reaching $1 ms^{-1}$). Incidentally, observations of stratocumulus layers also revealed the presence of well organized updraft-downdraft cells.

6. OBSERVATION OF STRATIFORM PRECIPITATION

The general purpose of this part of our research was to observe and study the physics and dynamics of stratiform precipitation. Such a precipitation system is essentially characterized by very low air vertical velocity, as compared to convective rain in which updrafts and downdrafts are predominant features. Our approach was to acquire vertical profiles of mean Doppler velocity and backscattered signal intensity using the 94 GHz Doppler radar, again operated in a vertically pointing beam mode. This work is presented and discussed primarily in [10] and [12].

Examples of vertical profiles of signal intensity and mean Doppler are

shown in Figs.3a and 3b, respectively. Fig.3a shows that, from the ground up to approximately 2.3 km, the received signal profile exhibits a systematically decreasing intensity with a quasi-linear slope. Since the mean rainfall intensity did not vary appreciably from the ground up to the 2 km level (as indicated by the mean Doppler profile shown in Fig.3b), the signal intensity decrease with height is attributed to signal attenuation by precipitation. The slope of the function can then be interpreted in terms of the attenuation coefficient alone which, in this case, was found to be 8 dB km^{-1} (two-way path). This attenuation coefficient measurement was compared to measurements by other researchers and found in good agreement with their results. It was also compared to the theoretical attenuation coefficients based on Mie function that we calculated (see above). These investigations are discussed in more detail in [15].

For the data shown in Fig.3 the air temperature is below freezing above the 2.5 km altitude level and, beside the likely presence of very small size supercooled droplets "unseen" by the radar, the larger hydrometeors found there must be of the ice crystals and snowflakes type (graupel is more likely found in convective storms in which updraft velocity is significant). The experience acquired in observing stratiform precipitation with centimeter wave radars indicates that in such conditions, moving down from an altitude well above the freezing level, radar reflectivity increases suddenly due to the partial melting of snowflakes when falling in the transition zone where air temperature becomes above freezing. Below this altitude, the backscattering signal intensity decreases due to a lower particles' concentration associated with an increase of their fall speed occurring when they evolve from a wetted snowflake structure into a lower drag raindrop shape. The combination of these processes thus yields a reflectivity profile maximum at an altitude slightly below the freezing level. This characteristic feature of radar signal intensity vertical profile in stratiform precipitation was named "bright band" because of the association between signal intensity and radar display brightness. However, the bright band is not observed at 94 GHz. The drastic change in signal reflectivity due to snowflake melting appears clearly but there is no vertical profile maximum. Furthermore, a minimum of signal intensity ("dark band") just above the freezing level is often found in the vertical profiles. It was speculated that the difference between signal intensity profiles observed with centimeter wave opposed to that observed with millimeter wave radars may be attributed to the

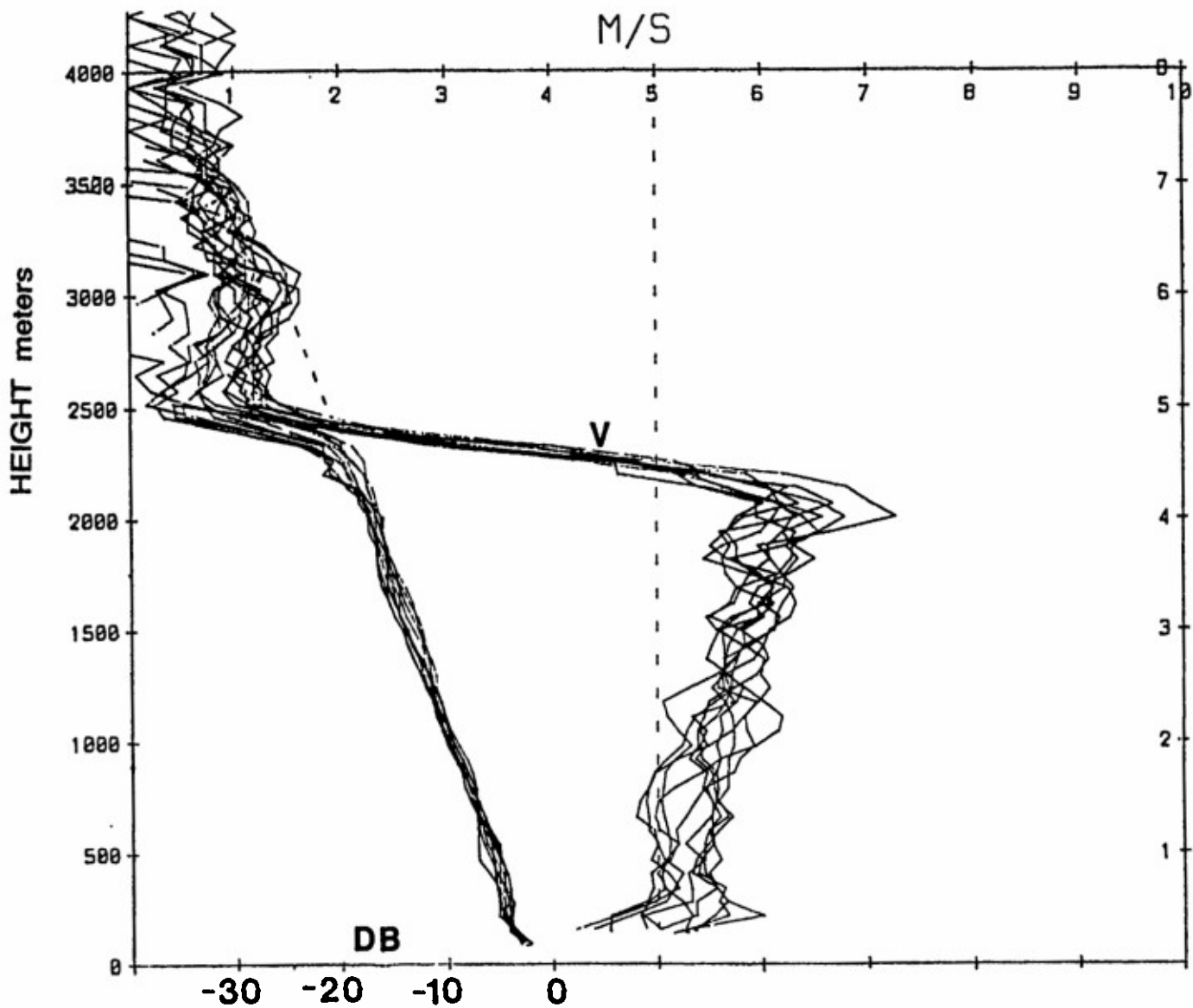


Fig. 3. Presentation of 10 profiles, derived from data acquired on 30 November at 5s time intervals, of signal intensity and mean Doppler. Signal intensity is corrected for R^2 but not for attenuation and indicated in relative units. Note the well defined signal intensity vs height slope equivalent to 8 dB km^{-1} two-way attenuation. Mean Doppler data are not corrected for air density.

peculiarities of Mie backscattering, i.e. an increase of particle size may be associated with a decrease of signal intensity. In the case of centimeter wave radars, Rayleigh backscattering prevails which thus implies that an increase of particle size is unquestionably associated with an increase of backscattering cross section. These considerations are discussed in more detail in [11] and to a lesser degree in [15].

Fig.3b shows the vertical profile of mean Doppler. The observed values appear to be much smaller than those observed with centimeter wave radars for the same precipitation intensity. This is due to the fact that the Rayleigh backscattering-raindrop diameter relationship, which has a D^6 form strongly enhancing the contribution from large raindrops, does not apply and must be replaced by Mie scattering functions. Indeed, the Mie functions emphasize contribution from raindrops having a diameter near the Mie maximum (1 mm) at the 94 GHz frequency. The observed mean Doppler velocity data are in agreement with the theoretical mean Doppler values determined in [15].

The systematic increase of mean Doppler with greater altitudes clearly seen in Fig.3b is attributed to the decrease of air density experienced when moving up in the atmosphere. The slope of the mean Doppler function is in agreement with a theoretical assessment of air density effects on raindrops' terminal velocity [10].

Comparing Fig.3a and Fig.3b indicates that the mean Doppler profiles variability (in both altitude and time) is not reproduced in the signal intensity profiles which are amazingly steady. This is attributed to the fact that most of the mean Doppler variability is due to the contribution of small-scale air velocity (updraft- downdraft) fluctuations which appear surprisingly high for data acquired in such steady rain conditions [10], [12].

In addition to the processing of spectral moments (signal intensity and mean Doppler) discussed above, complete Doppler spectra were calculated and displayed. This was accomplished by performing a FFT operation on the "coherent video" I and Q signals delivered by the phase coherent radar receiver, simultaneously sampled at 16 selected range gates. A high speed (15 MHz sampling rate) signal digitizer was used and, since there was no real-time processing of the radar signals, the spacing between range gates was reduced 100 ns. For these measurements, a 100 ns radar transmitter pulse was selected so that a 15m vertical resolution was effectively obtained.

The Doppler spectra calculated from the FFT procedure applied to

data collected in 10- 20 $mmhr^{-1}$ stratiform rain at vertical incidence using this method revealed the systematic presence of a well-defined notch in the spectrum. An example of such observations is shown in Fig.4. The spectral notch was found to be related to the first backscattering cross section minimum in the Mie function at 94 GHZ which is shown in Fig.1. This minimum occurs at a 1.6 mm raindrop diameter, and thus its position in the spectrum yields direct measurements of the vertical velocity of raindrops of that size. This also allows an objective determination of air velocity by comparing the observed spectrum to a theoretically predicted spectrum (shown in Fig. 4, see captions) based on Mie functions, a terminal velocity vs size relationship (corrected for the air density at the altitude at which the observations are made), and a Marshall-Palmer dropsize distribution.

This concept was implemented using a more refined correlation method [10],[12]. To avoid problems related to departure of an actual dropsize distribution from the M-P model (especially for very large or very small raindrop size), the correlation calculations were limited to a relatively small diameter interval around the Mie minimum occurring for a 1.6 mm raindrop diameter in the predicted spectrum. The procedure applied to our stratiform rain data showed that up- downdrafts with a magnitude sometimes reaching $\pm 40 \text{ cms}^{-1}$ were often observed. The correlation method yields an objective measurement of vertical air velocity which can be used to correct the Doppler velocity at vertical incidence so that a dropsize distribution, whose expression is necessarily based on a terminal velocity vs diameter relationship, be derived from the Doppler spectrum. An example of a dropsize distribution obtained using this procedure is shown in Fig.5.

The above considerations as well as more general results related to analysis and interpretation of the Doppler spectra including some application to downdraft measurements in convective storms are more extensively discussed in [10] and [12].

6. 94 GHZ RADAR ON A SATELLITE ORBITING PLATFORM

The experience acquired with the 94 GHz Doppler radar we developed and used extensively for observations of clouds and precipitation from the ground provided us the opportunity to explore the capability of such a radar for remote sensing of cloud and precipitation from space. The proposal of a 94 GHz radar installed aboard a low orbit satellite was thus considered and

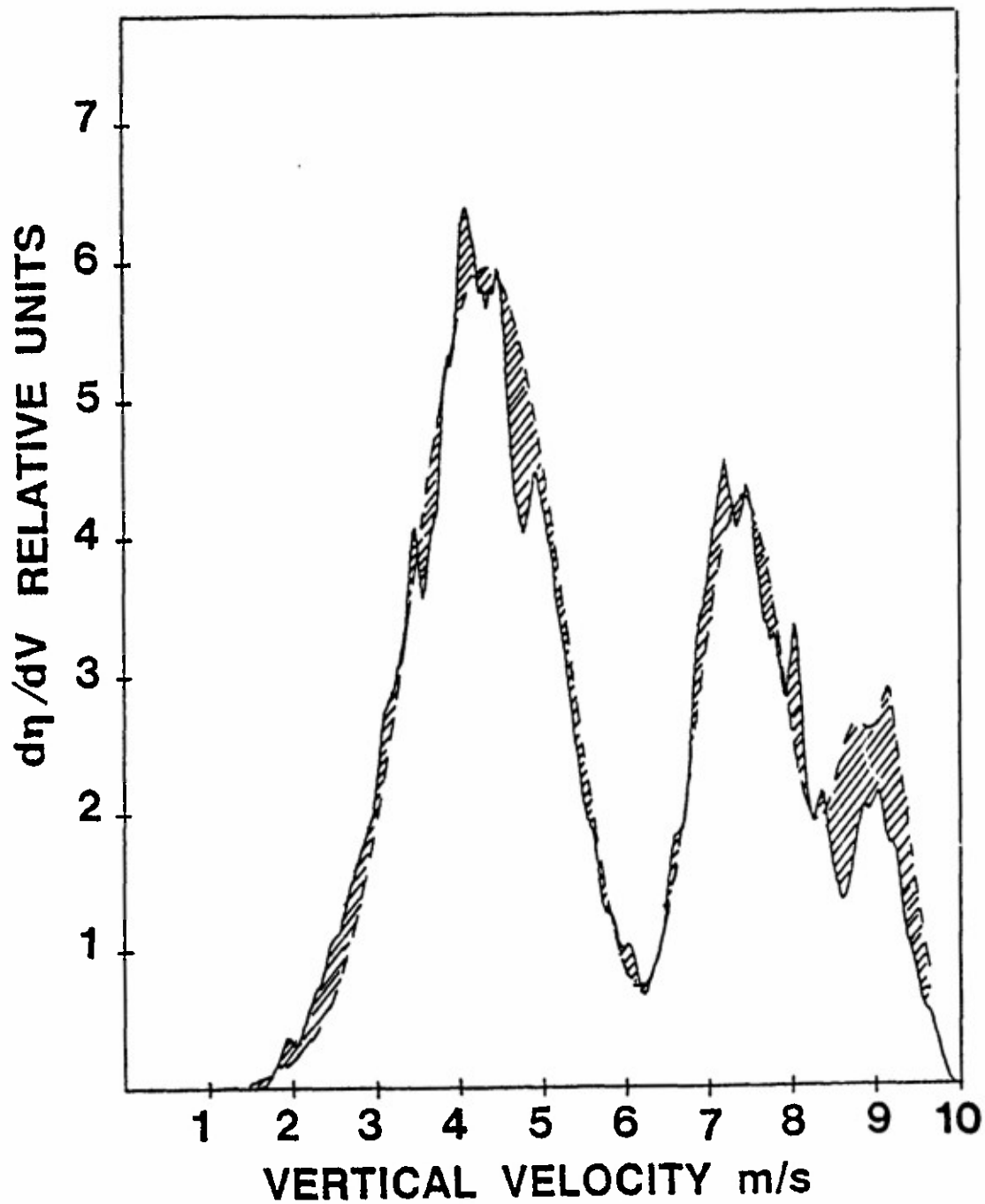


Fig. 4. Radial velocity (Doppler) spectrum observed in a 15 mm/hr rain at vertical incidence together with a predicted spectrum (dashed line) based on Mie backscattering cross section and an exponential dropsize distribution with the slope, Λ , adjusted for best fit. The shaded area shows the difference between the observed and predicted spectrum. The most noticeable feature is the spectral dip at 6.2 m/s.

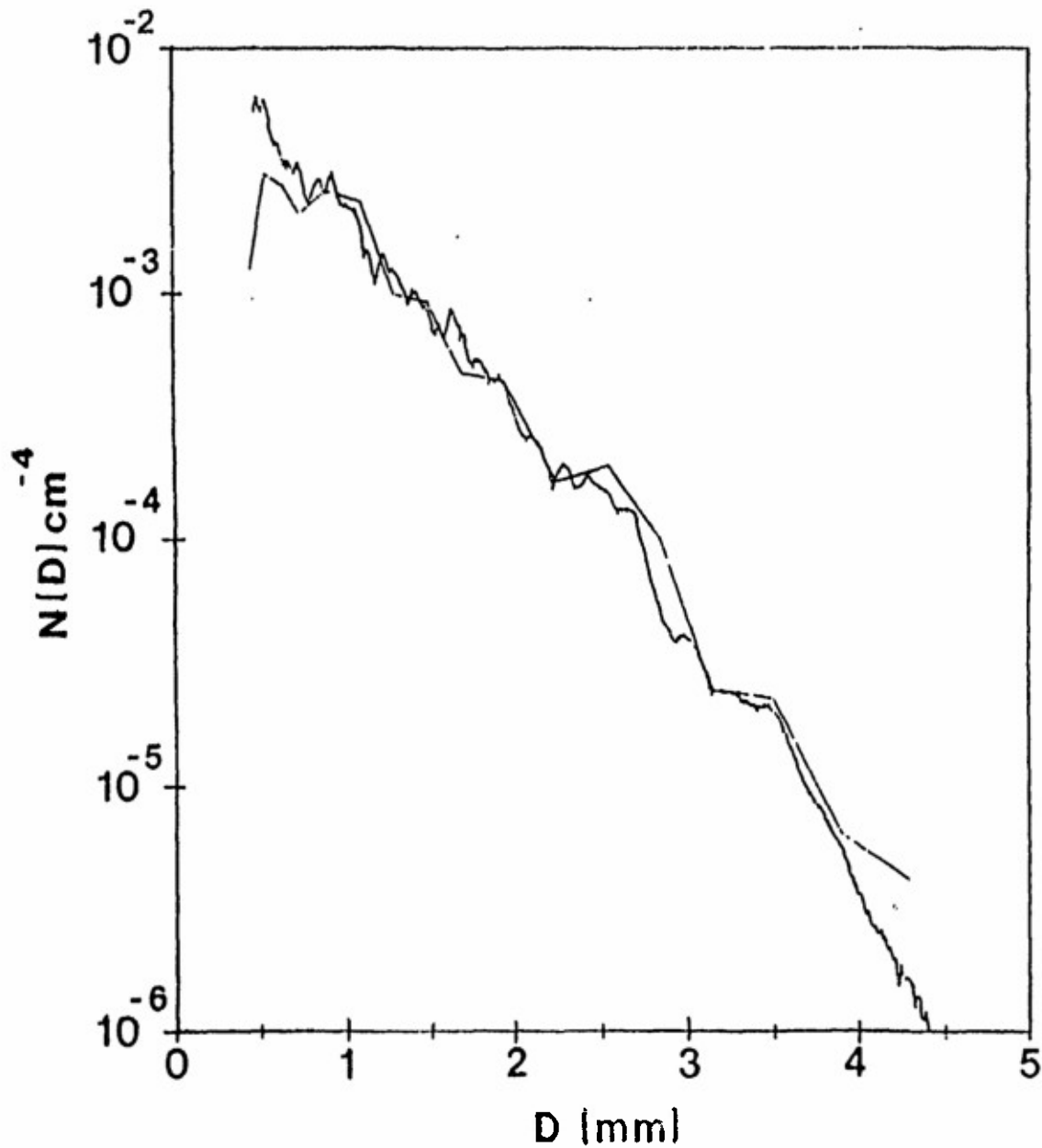


Fig. 5. Example of a dropsize distribution observed using the Doppler radar method discussed in the text and compared with disdrometer data (smoother function) acquired at the same time.

an article presenting and discussing the radar concept and design as well as an assessment of the radar's capabilities for probing hurricane circulation from space was published [13].

7. CONCLUSION AND RECOMMENDATION FOR FUTURE WORK

This project has demonstrated that the ground-based 94 GHz Doppler radar we developed and used for precipitation and cloud remote sensing is a viable tool for meteorological research and may also be successfully used for remote sensing from an airborne or satelliteborne platform.

Our prototype was developed without any background reference to any other similar system so that we experienced growing pains with some of the components. A significant amount of time was spent to maintain the equipment in an operational condition, especially the pulse modulator part of the radar which failed often, sometimes at critical times. We believe that this sort of experience helped the manufacturers of some of the components, such as Varian Associates and Pulse Technology Inc., to develop more reliable, commercially available, products. We also believe that the problems experienced in the early stages of the radar development have now been solved. Therefore, a 94 GHz Doppler radar of the kind we developed can be operated with the reliability of a well-designed X-band radar.

The coherent-on-receive method for the extraction of the Doppler frequency shift, which saves the much greater cost of a four cavities EIA (Extended Interaction Amplifier), appeared very reliable and yielded surprisingly low noise Doppler spectra considering the very high (94 GHz) operating frequency. A large part of this success is due to the excellent characteristics of the EIO (Extended Interaction Oscillator) tube.

Considering a new equipment, sensitivity can be increased by use of a larger antenna, i.e. a 180 cm dish in a Cassegrain configuration. Such antenna can be manufactured at a reasonable cost at the 94 GHz frequency and would increase the receiver sensitivity by 6 dB compared to that available with the 90cm dish used in our radar. In addition, the EIO peak power can be increased to 2kW and possibly slightly more. Also the receiver noise figure can be improved by possibly 2 dB. All of these improvements would yield a radar sensitivity increase of approximately 10 dB compared to that of the radar we developed originally. This would represent a substantial improvement of small cloud detectability. Our experience indicates that

although fair weather cumuli of maritime origin are always detected and observed, fair weather cumuli of continental origin are sometimes not 'seen' by the radar. This may be due to the fact that the median diameter of the population of cloud droplets in the maritime cloud is 9-12 μm compared to 7-9 μm in continental cloud. The 10 dB increase in sensitivity would allow that all fair weather clouds be observed.

Observations of fair weather cumuli by the radar can be significantly improved, not only by the increase of sensitivity quoted above, but also by a (approximately) $\pm 10^\circ$ beam angle scanning from vertical in a direction perpendicular to cloud motion. This beam scanning procedure would minimize contribution to Doppler from the cloud horizontal velocity. In addition, since the scanning is limited to a small angle from vertical, practically air vertical velocity alone is observed by the radar. The beam scanning combined with the cloud motion would then yield observation of the fields of reflectivity and vertical velocity in three dimensional space. This is a drastic improvement over the fixed beam method producing only a vertical cross section of the fields.

Using the equation of mass continuity, the dw/dz term inferred field from the vertical velocity field can be interpreted in terms of horizontal divergence of the motion fields which, in turn can be used to specify the cloud entrainment. This procedure, assisted by the three dimensionally measured radar reflectivity could serve as an input for the development of cloud circulation and dynamics models.

One of the advantages of the radar is its ability (confirmed by experience) to observe small nearby meteorological targets without ground clutter problems, thus allowing extremely short range operation. This is due to the λ^{-4} Rayleigh backscattering enhancement (60 dB with respect to S-band) which yields a high meteorological target-ground clutter contrast and allows low power detection of even weak weather targets. Incidentally the very short range operation yields observation of extremely low reflectivity targets (primarily above water) with some of them not explained by the presence of hydrometeors.

An application which was not considered in our research is to observe a heavy pollution environment containing a few μm size particulates. Using the Doppler capability, the air motion fields can be determined leading to an estimate of factors governing pollution occurrence. We believe that, especially with the improved sensitivity, such 94 GHz Doppler radar obser-

vations can be done from a minimum range of 50 meters to a few kilometers, if the particulate size reaches several μm 's. These considerations can also be applied to the observation of fog.

We also believe that the results reported here can serve as incentives for airborne (and possibly satelliteborne) use of the 94 GHz radar.

A last word. Other millimeter wave frequencies in atmospheric absorption windows ranging from 35 GHz to 240 GHz could be considered. However, the 94 GHz frequency seems to offer a very good compromise between frequencies which are too low to take a real advantage of the Rayleigh scattering enhancement and frequencies which are too high so that signal attenuation problems, low transmitter power, and hardware development costs become overwhelming. A 94 GHz radar for which commercially available hardware exists, represents a good compromise and that frequency may be considered as an adequate choice for a millimeter wave meteorological radar.

REFERENCES ¹

List of papers written under our ARO support, containing references to publications outside of our project:

- [1] Lhermitte, R., 1981. Satelliteborne dual millimetric wavelength radar, in Atlas, D. and Otto Thiele (eds), Precipitation measurements from space, Workshop report, VASA Goddard Space Flight center, D- 277-282.
- [2] Lhermitte, R, 1981. Millimeter wave Doppler radar, Proc. 20th . Radar Meteor. Conf. Amer. Meteor. Soc. 744-748.
- [* 3] Lhermitte, R. and C. Frush, 1984. Millimeter wave radar for Meteorological observations. Proc. 22 th Radar Meteor. Conf., Amer. Meteor. Soc. 228-231.
- [4] Lhermitte, R., 1986. Absorption and scattering by cloud and precipitation at 95 GHz, Presented at the Airborne Doppler Meeting National Center for Atmospheric Research, Boulder , Colorado.
- [* 5] Lhermitte R. 1986. A 3 mm wavelength Doppler radar for meteorological observations Preprint volume, International Union of Ra-

¹* indicates that ARO support is explicitly acknowledged in the article

dioscience, Commission F, Wave Propagation and Remote Sensing, 6.7.1-6.7.4.

- [* 6] Lhermitte, R., 1986. Observation of clouds and precipitation using a 94 GHz Doppler radar, Presented at the Workshop on ground based remote sensing of the troposphere, Hamburg, Germany.
- [* 7] Lhermitte, R., 1986. Cloud and precipitation observation with 94 GHz radar. Proc. Cloud Phys. Conf. Snowmass Village, Col., Amer. Meteor. Soc., 169-172.
- [* 8] Lhermitte, R., 1987. 94 GHz Doppler radar for cloud observations, J. Atmos. Tech. Vol. 4, No 1, 36-48.
- [* 9] Lhermitte, R., 1987. Small cumuli observed with a 3 mm wavelength Doppler radar, Geophys. Res. Lett., Vol. 7, No 7 707-710.
- [* 10] Lhermitte R., 1988. Observation of rain at vertical incidence with a 94 GHz Doppler radar: an insight on Mie scattering, Geophys. Res. Lett., Vol. 15, No 10 1125-1128.
- [* 11] Lhermitte, R., 1988. Cloud and precipitation remote sensing at 94 GHz, IEEE Transac. Geosc. Remote sensing, Vol. 26, NO 3, 207,216.
- [* 12] Lhermitte, R., 1989. Mie scattering observations by a 94 GHz Doppler radar at vertical incidence, Proc. 24 th Conf. Radar Meteor., Amer. Meteor. Soc., 1-4.
- [* 13] Lhermitte, R., 1989. Satelliteborne millimeter wave Doppler radar, URSI Commission F., Open Symposium Proc.
- [* 14] Lhermitte, R., 1989. Millimeter wave radars in Meteorology, Amer. Geophys. union Trans., (invited paper), 70:(15):285.
- [* 15] Lhermitte, R., 1990. Attenuation and scattering of millimeter wavelength radiation by clouds and precipitation, 1990, J. Atmos. Tech., Vol 7, No 3.

Attenuation and Scattering of Millimeter Wavelength Radiation by Clouds and Precipitation

ROGER LHERMITTE

Rosenstiel School of Marine and Atmospheric Sciences, University of Miami, Miami, Florida

(Manuscript received 27 April 1989, in final form 27 October 1989)

ABSTRACT

This article is concerned with investigations of scattering and absorption of 35, 94, 140, and 240 GHz radiation by clouds and precipitation. The computations of radar reflectivity, Doppler spectra, and absorption coefficients are performed using Mie functions and exponential drop-size distributions. The results can be used for an assessment of the applicability of short-wavelength Doppler radars for observation and study of clouds and precipitation either from the ground or from a space platform.

1. Background

The backscattering cross section of small scatterers (size much smaller than the incident radiation wavelength, λ) is proportional to $1/\lambda^4$ so that, compared to that observed at a 3 GHz frequency ($\lambda = 10$ cm), the radar reflectivity of a cloud of small droplets (e.g., diameter less than 100 μm) is greater by 42 dB at 35 GHz, 60 dB at 94 GHz, and 74 dB at 240 GHz. Therefore, radars operating at a frequency within the millimeter wave radio spectrum (wavelength interval 1 to 8.5 mm) appear as more sensitive cloud observing instruments than centimeter wave radars.

The choice of a wavelength suitable for radar operation in the earth atmosphere is restricted to spectral regions in which absorption of the radar signal by atmospheric gases, namely oxygen and water vapor, is minimal. The presence of absorption lines at 23 GHz (H_2O), 60 GHz (O_2 absorption band), 118 GHz (O_2), and 183 GHz (H_2O) restricts the wavelength choice to windows centered on 35, 94, 140 GHz, and between 200 and 300 GHz. The residual atmospheric attenuation in the windows is primarily due to the skirts of water vapor absorption lines and increases systematically with shorter wavelengths [for a complete view of atmospheric gas absorption in the millimeter wave spectrum see Liebe (1985) and Lhermitte (1987)].

The first millimeter wave radar designed for meteorological use was a 35 GHz system (see Paulsen et al. 1970). The radar was originally assigned by the US Air Force to cloud deck monitoring, essentially as a replacement for the optical ceilometer. More recently,

35 GHz radars have been equipped with Doppler capabilities and used again for the observation of clouds and precipitation (Hobbs et al. 1985; Pasqualucci et al. 1983; Omar and Sauvageot 1987). It was also demonstrated that an even shorter wavelength ($\lambda = 3.2$ mm or 94 GHz) radar (Lhermitte 1987), operating with 1 kW transmitted peak power and 3-foot size antenna was a viable meteorological tool providing effective observations of liquid water content and internal circulation in small clouds. Observing rainfall at vertical incidence with the 94 GHz Doppler radar also revealed that some of the raindrop size-related Mie backscattering oscillations can be clearly seen and thus can be used for raindrop's diameter identification (Lhermitte 1988b).

Present research and development of millimeter wave tubes (such as the "gyrotron" for example) is expected to contribute to the availability of more powerful transmitters, possibly reaching 50 kW peak power and 50 watts average power. A 94 GHz radar equipped with such a transmitter and a 2 m antenna would have a sensitivity 16 dB higher than that of the 94 GHz radar mentioned above (Lhermitte 1987, 1988a). Such sensitivity allows detection of clouds having a radar reflectivity as small as -60 dBZ (e.g., 1 mg m^{-3} of liquid water divided into 8 μm droplets) at 2 km range, and probably would allow short range observation of heavy pollution layers in which particulates may reach a few micrometer size. Radars operating at 240 GHz (Narayanan et al. 1988) may in the future represent a viable solution for the observation of small clouds, especially ice clouds. Therefore the characteristics of scattering and attenuation of 240 GHz radiation by hydrometeors is also considered in this article.

Millimeter-wave radars have two distinct advantages over centimeter-wave radars:

Corresponding author address: Dr. Roger M. Lhermitte, Division of Meteorological and Physical Oceanography, University of Miami, 4600 Rickenbacker Causeway, Miami, FL 33149-1098.

- Very narrow beams are produced with small antenna size.
- Rayleigh scattering gain reduces the need for high power transmitters.

A 3.2 mm wavelength radar, equipped with a 2 m antenna and a relatively low power (1 kW peak) transmitter, has the same 0.1° antenna beamwidth and sensitivity on weak distributed targets (such as a small cloud), as would have a 10 cm wavelength radar with a 60 m antenna and a 1 MW peak power transmitter. The difference in dimension, weight, and power supply requirements between these two radars is enormous. However, even if the millimeter wave radiation frequency lies in a spectrum window, it is significantly more attenuated than centimeter wave radiation when propagating through clouds and precipitation.

Observations of small (e.g., boundary layer) cumuli can be successfully conducted with millimeter wave radars without much concern about signal attenuation by cloud droplets (Lhermitte 1988a). However, deep stratus and cumulus clouds possibly reaching the precipitation stage bring significant attenuation problems and heavy precipitation may attenuate millimeter wave radiation so much that the effectiveness of the radar as a weather probing tool may be significantly reduced. For instance, the successful operation of the satellite-borne Doppler radar mentioned in the conclusion—even if its main capability is the probing of motion fields in precipitation systems—may be severely limited if the radar radiation does not reach sufficient low altitude levels in the storm. Therefore, the evaluation of a millimeter wave radar's performance as a weather remote sensing tool must rely on assessment of the physical conditions governing scattering and absorption of millimeter waves by clouds and precipitation.

The scattering and absorption of both millimeter wave and microwave radiation by cloud droplets (or any particulate or hydrometeor smaller than approximately $100 \mu\text{m}$) can be treated using the Rayleigh approximation (scatterers much smaller than the radar wavelength). Evaluating performance is easy since, in these conditions, the familiar backscattering σ , scattering Q_s , and absorption Q_a cross sections are given by

$$\sigma = \pi^5 D^6 / (\lambda^4 |K|^2) \quad (1)$$

$$Q_s = 2\pi^5 D^6 / (3\lambda^4 |K|^2) \quad (2)$$

$$Q_a = (\pi^2 D^3 \text{Im}(-K)) / \lambda, \quad (3)$$

where $|K|^2$ and $\text{Im}(-K)$ are derived from the complex index of refraction $m = n' + in''$ (n' is the real part and n'' is the imaginary part). Here $|K|^2$ decreases slightly with shorter wavelengths and $\text{Im}(-K)$ varies with temperature and wavelength (see Table 1).

If the particles are small compared to the radiation wavelength (Rayleigh limit), radar signal attenuation by scattering is always small compared to the effect of

absorption. Absorption of radiation by ice particles is also negligible even at millimeter waves, but scattering attenuation by ice particles, while being negligible for Rayleigh scatterers, becomes significant if larger particles are considered.

Although cloud particles (less than $100 \mu\text{m}$ diameter) can be always considered as Rayleigh scatterers regardless of radar wavelength, this does not hold for precipitation particles and, at millimeter wavelengths, relationships between precipitation intensity and radar reflectivity or signal attenuation must be investigated using Mie functions. Even at 35 GHz, Rayleigh backscattering is not rigorously valid for a particle diameter greater than 1 or 2 mm. At 94 GHz and above, scattering by all raindrops falls in the Mie region.

This article investigates the characteristics of absorption and scattering of millimeter wave radiation by hydrometeors in an effort to provide the basic information needed for an assessment of the performance, as a cloud or precipitation observing instrument, of a ground- or satellite-based millimeter wave radar. There are scattering and absorption theoretical solutions for nonspherical particles but, since the geometry of these nonspherical hydrometeors (except for cloud droplets and some raindrops) is difficult to specify, only spherical raindrops or hailstones identified with ice spheres are considered here. Because of the dominant effect of surface tension for small water spheres the assumption of spherically shaped raindrops is adequate for diameters up to approximately 2 mm.

In this article, the absorption, scattering, and backscattering cross sections of spherical particles are computed theoretically using the classical Mie functions (Mie 1908). The first task was to implement Mie function programs for the computation of scattering and absorption cross sections of raindrops (temperature ranging from 0° to 20°C) and ice spheres as a function of particle's diameter, which was done at the 35, 94, 140, and 240 GHz frequencies mentioned above. These computations required specification of the complex index of refraction of water and ice for all frequencies and temperatures considered. These data were compiled from several sources found in the literature on the subject (Ray 1972). The $\text{Im}(-K)$ and $|K|^2$ parameters computed from the index of refraction values have also been added to this list; the results are presented in Table 1.

The Mie functions were calculated for the frequencies and temperatures listed above and then stored for use in programs assembled to compute several radar related precipitation parameters.

2. Drop-size distribution and precipitation related parameters

In addition to the Mie functions the programs designed to calculate radar related precipitation parameters require specification of a drop-size distribution.

TABLE 1. Index of refraction of water and ice at selected frequencies and temperatures.

Frequency (GHz)	Water/ice	Temperature (°C)	n'	n''	$ K ^2$	$\text{Im}(-K)$
35	water	0	4.18	2.58	0.892	0.1027
35	water	10	4.67	2.78	0.906	0.0835
35	water	20	5.2	2.87	0.912	0.0676
35	ice	0	1.8	0.0001	0.182	0.0001
94	water	0	2.846	1.48	0.711	0.1938
94	water	10	3.128	1.75	0.77	0.17
94	water	20	3.41	2.02	0.828	0.147
94	ice	0	1.78	0.0004	0.176	0.0001
140	water	0	2.50	1.05	0.569	0.2006
140	water	10	2.68	1.25	0.643	0.1952
140	water	20	2.86	1.53	0.724	0.190
140	ice	0	1.76	0.0004	0.169	0.0001
240	water	0	2.3	0.6	0.414	0.148
240	water	10	2.45	0.8	0.494	0.169
240	water	30	2.45	1.1	0.577	0.215
240	ice	0	1.75	0.0003	0.169	0.0001

In the past considerable effort was devoted to selection of an appropriate drop-size distribution and the rain parameters attached to it (Atlas 1964; Atlas and Wexler 1963; Joss 1968; Sekhon and Srivastava 1971; Willis 1984; Ulbrich 1983; 1988. However, the exponential distribution $N(D) = N_o \exp(-\Lambda D)$, derived from the original Marshall and Palmer (M-P) (1948) distribution is a very convenient model and will be used throughout this work.

The M-P distribution was originally conceived to be a unique function of the rain intensity, R , expressed by

$$R = (\pi/6)3.6 \cdot 10^4 \int_0^\infty [N(D)D^3V(D)]dD, \quad (4)$$

where R is in mm h^{-1} , $N(D)$ is in cm^{-4} , D is in cm , and the raindrop vertical velocity, $V(D)$ is in cm s^{-1} . In the original M-P distribution, N_o is fixed and Λ is a function of R only. However, an analytical solution for Λ as a function of R and N_o can be found if an integral such as (4) has the following form:

$$\int_0^\infty [\exp(-\Lambda D)D^n dD] = \Gamma(n + 1)/\Lambda^{n+1}. \quad (5)$$

with the right member of the equation showing the solution.

Equation (4) can thus be solved in close form using the $V(D)$ relationship proposed by Spilhaus (1948): $V(D) = 1420D^{0.5}$, yielding the analytical solution: $\Lambda = 82.2N_o^{2/9}R^{-2/9}$. The Spilhaus relationship exhibits significant departures from the measurements of terminal velocity of raindrops by Gunn and Kinzer (G-K) (1949). The following $V(D)$ equation (Lhermitte 1988b), is more appropriate since it matches the G-K experimental measurements within 5 cm s^{-1} in the $50 \mu\text{m}$ to 6 mm raindrop diameter range;

$$V(D) = V_o[1 - \exp(-6.8D^2 - 4.88D)], \quad (6)$$

where $V(D)$ is in cm s^{-1} , D is in cm , $V_o = 923(\rho_o/\rho_z)^{0.5}$ with ρ_o and ρ_z being the air density at the ground and at the altitude z at which $V(D)$ is expressed, respectively. Using the $V(D)$ function (6) in Eq. (4) ($\rho_z = \rho_o$) and solving numerically leads to a $\log(\Lambda)$ versus $\log(R)$ relationship slightly nonlinear but in close agreement with a mean slope (0.03 to 400 mm h^{-1} domain) yielding the solution:

$$\Lambda = 69.7(R/N_o)^{-0.21}. \quad (7)$$

With $N_o = 0.08$, (7) reduces to the familiar expression $\Lambda = 41R^{-0.21}$ proposed by M-P. If the relationship between $\log(\Lambda)$ and the logarithm of a given parameter can be represented by a linear function, N_o is a constant term independent of D . For instance, if liquid water content, M in g m^{-3} , is considered, $\Lambda = 42.1(M/N_o)^{-1/4}$ (also proposed by Willis 1984). Using this expression and Eq. (7) we have:

$$M = 0.133(N_o)^{0.16}R^{0.84}. \quad (8)$$

With $N_o = 0.08$ this reduces to $M = 0.0887R^{0.84}$, which is in close agreement with the expression proposed by Sekhon and Srivastava (1971). In the same way the relationship between the familiar radar reflectivity factor $Z = \int [N(D)D^6 dD]$ (in $\text{mm}^6 \text{m}^{-3}$) and R is $Z = 89.71(N_o)^{-0.469}R^{1.47}$ which, with $N_o = 0.08$ reduces to $Z = 293R^{1.47}$.

A relationship such as (8) for instance, or the $Z-R$ relationship above, allows the use of exponential distributions in which N_o may have a different value from that in the M-P expression, such as the "thunderstorm distribution" ($N_o = 0.014 \text{ cm}^{-4}$) and the "drizzle distribution" [$N_o = 0.3 \text{ cm}^{-4}$ proposed by Joss et al. (1968)]. If the N_o term is constant, the slope of the $\log Z$ versus $\log R$ relationship is independent of Z or R . A large number of empirical $\log Z$ - $\log R$ relationships have been proposed in the last 40 years. Within the context of Rayleigh scattering (also no polarization

effects) and a linear exponential drop-size distribution, a $\log Z$ versus $\log R$ linear regression slope different from the 1.47 value mentioned above may be explained by a possible statistical dependence between N_0 and R in a dataset including different types of rain.

Actual raindrop size distributions may not have a linear exponential slope in the full raindrop size domain but rather exhibit a systematic increase of that slope with raindrop size, so that the function becomes asymptotic to a D value which represents the largest possible drop diameter found in that particular type of rainfall. This effect is more noticeable for high rain intensity and thus may reduce the slope of the $\log Z$ versus $\log R$ relationship on the high end of that function. Nevertheless, as a consequence of Mie scattering, the $\log \eta$ (η is the radar reflectivity) versus $\log R$ (or $\log M$) function is not linear at millimeter wavelengths.

Other drop-size distributions have been proposed: the gamma (Ulbrich 1983; Willis 1984) and the log-normal (Feingold and Levin 1986) functions, which essentially remove the M-P linear exponential slope restriction. However, at millimeter wavelengths radar reflectivity is not overly dominated by contributions from large size raindrops as it is for Rayleigh scattering. Furthermore, except for very light rain intensity for which, anyhow, the linear slope of the size distribution seems to extend to very small drop size, the contribution to radar reflectivity from drops having a diameter smaller than 0.5 mm is not significant. Indeed, as seen below, the bulk of the contribution to radar reflectivity and attenuation (both scattering and absorption) comes from raindrops with a diameter between 0.5 and 3 mm, so that a linear slope exponential distribution is an acceptable choice, requiring only specification of N_0 or an assessment of the influence of N_0 on the results. Furthermore, the simple form of the exponential distribution is easy to manipulate and leads to easily interpretable results. In the course of this research we concluded that a linear exponential distribution, in which N_0 is allowed to vary, is a convenient model yielding representative results.

The rainfall parameters selected for computation are: radar reflectivity, mean Doppler velocity and Doppler spectrum width observed with a vertically pointing radar beam, and attenuation coefficients.

These parameters are presented as a function of rain intensity. However, liquid water content, M , and precipitation parameters such as radar reflectivity, η , and radar signal attenuation coefficients are related to volume concentration of hydrometeors. The concept of rain intensity (which is really only valid at the ground) involves a vertical flux of the liquid water at a given mean vertical speed, \bar{w} . Here \bar{w} is a "raindrop mass weighted" mean velocity expressed by $\bar{w} = R/M$, and can be calculated assuming a given drop-size distribution and no air vertical velocity. Using an exponential drop-size distribution $N_0 \exp(-\Lambda D)$, $\bar{w} = 5250(\Lambda)^{-0.76}$ is a function of Λ only. The \bar{w} varies

from 216 cm s^{-1} for $\Lambda = 66 \text{ cm}^{-1}$ (0.1 mm h^{-1} M-P rain) to 794 cm s^{-1} for $\Lambda = 12 \text{ cm}^{-1}$ (200 mm h^{-1} M-P rain). In the case of significant up-downrafts (downward motion is usually taken as negative), w_a , $R = M(\bar{w} \pm w_a)$. In this perspective, the choice of rain intensity to represent what is really a volume concentration of liquid or solid water may appear questionable when applied to hydrometeors above the ground. However, the use of rain intensity as a valid parameter was discussed in more detail by Kessler (1987) and Lee (1988) and their conclusions are used as a justification for the selection of this quantity as a bonafide variable for the expression of the radar related parameters in this work.

All parameters (including rain intensity) are numerically computed using an exponential drop-size distribution and when needed, the raindrop size versus terminal velocity relationship (6) and the Mie functions.

3. Backscattering cross sections

The Mie backscattering cross section, σ_{Mie} , of water spheres calculated at the 35, 94, 140, and 240 GHz frequencies is shown in Figs. 1 and 2 for water at a 0°C temperature. Rayleigh scattering does not apply to the full range of raindrops and even the clearly defined first Mie function minimum is within that range for all the selected frequencies. That minimum occurs at approximately $D = 4.5 \text{ mm}$ at 35 GHz, 1.67 mm at 94 GHz, 1.10 mm at 140 GHz, and 0.68 mm at 240 GHz. The 140 and 240 GHz functions clearly show that, for large diameters, the Mie oscillations are reduced and that σ_{Mie} tends to be equal to the raindrop's geometric cross section, σ_{Mie} increases slightly with

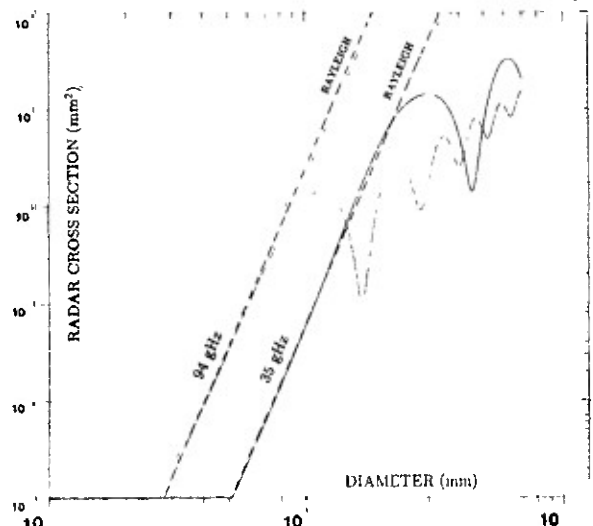


FIG. 1. Radar cross section of spherical raindrops as a function of their diameter at 35 and 94 GHz. The dashed lines indicate the Rayleigh scattering approximation.

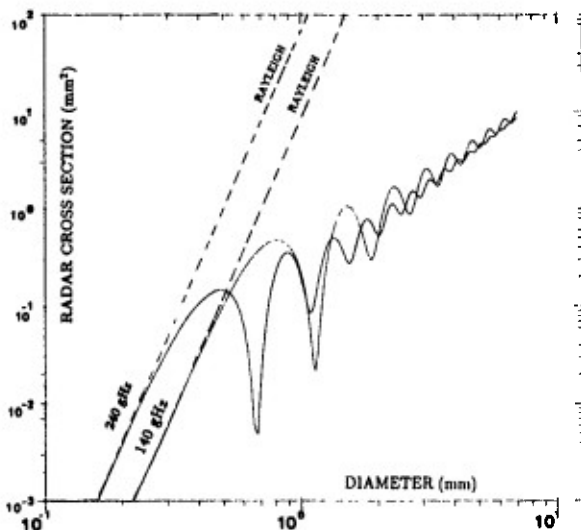


FIG. 2. As in Fig. 1 but for 140 and 240 GHz.

temperature, approximately 0.1 dB at 35 GHz, 0.7 dB at 94 GHz, 1.0 dB at 140 GHz, and 1.3 dB at 240 GHz, over the 0°C to 20°C temperature range.

Figure 3, which shows the $\sigma_{\text{Mie}}/\sigma_{\text{Rayleigh}}$ backscattering cross section ratio, indicates the maximum diameter value for which Rayleigh approximation is acceptable (Rayleigh function is also indicated by the dashed lines in Figs. 1 and 2); i.e., approximately, 2.5 mm at 35 GHz, 0.9 mm at 94 GHz, 0.5 mm at 140 GHz, and 0.3 mm at 240 GHz. Above these diameter values the Mie function oscillates but, on the average, departure from Rayleigh scattering increases with raindrop size. For a 5 mm diameter drop, for instance,

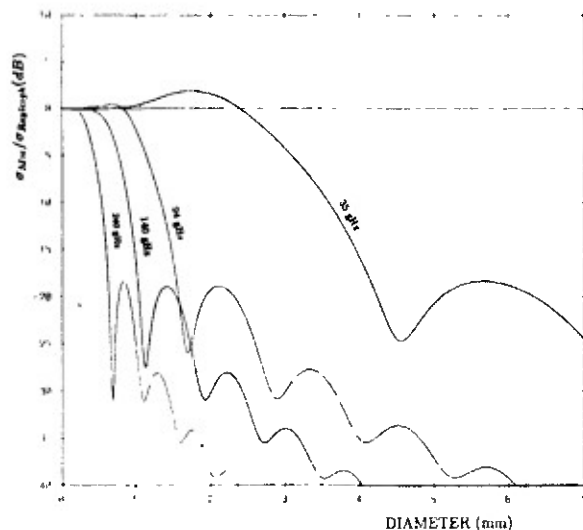


FIG. 3. Ratio (in decibels) of Mie to Rayleigh backscattering cross sections at the indicated radar frequency as a function of raindrop diameter.

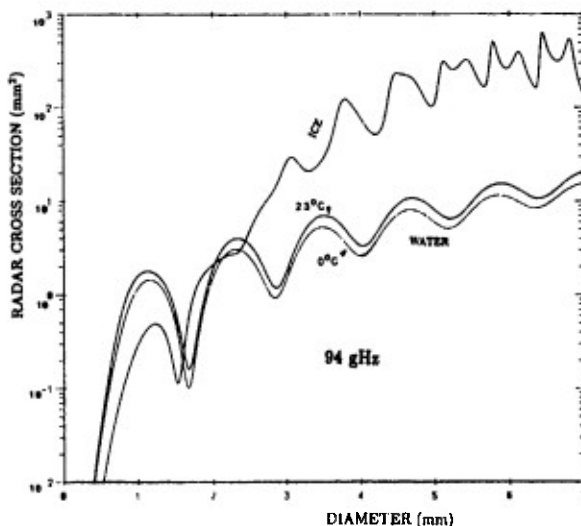


FIG. 4. Backscattering cross section of water (0° and 23°C temperature) and ice spheres as a function of diameter. Frequency is 94 GHz.

the actual Mie scattering is approximately 20 dB below Rayleigh at 35 GHz, 35 dB at 94 GHz, 45 dB at 140 GHz, and more than 55 dB at 240 GHz.

Figure 4 shows the 94 GHz radar cross section of both water spheres at two temperatures 0 and 23°C, σ_{water} , and ice spheres, σ_{ice} . Although, in the Rayleigh region, water raindrops are better scatterers than ice spheres of the same size, the effect is reversed for larger diameters with ice particles now being much more effective scatterers than water particles. Also note the relatively small variation of the backscattering cross section of raindrops as a function of their temperature (approximately 1 dB for a 0° to 23°C temperature change).

Figure 5 shows the ratio, $\sigma_{\text{water}}/\sigma_{\text{ice}}$, between water and ice spheres backscattering cross sections at the 35, 94, 140, and 240 GHz frequencies. In the Rayleigh region, $\sigma_{\text{water}}/\sigma_{\text{ice}}$ is equal to the ratio of the $|K|^2$ term for water and ice; i.e., -6.95 dB at 35 GHz, -6.4 dB at 94 GHz, -5.8 dB at 140 GHz, and -4.7 dB at 240 GHz. This holds within 1 dB up to $D \approx 4$ mm at 35 GHz, $D \approx 1.5$ mm at 94 GHz, $D \approx 1$ mm at 140 GHz, and $D \approx 0.6$ mm at 240 GHz. Above these values the effect is reversed and ice becomes a more effective scattering agent. Figure 5 shows that, above this "critical" diameter, ice spheres are consistently stronger scatterers than water spheres with $\sigma_{\text{ice}}/\sigma_{\text{water}}$ stabilizing at an average of 15 dB for a particle diameter greater than approximately 4 mm and for frequencies above 90 GHz. While the general wisdom in radar meteorology is to assume that the same amount of rainwater would produce less scattering if that water is converted to ice, this is not systematically true at millimeter waves (frequency above 90 GHz); even relatively small ice particles (graupel) such as commonly found in con-

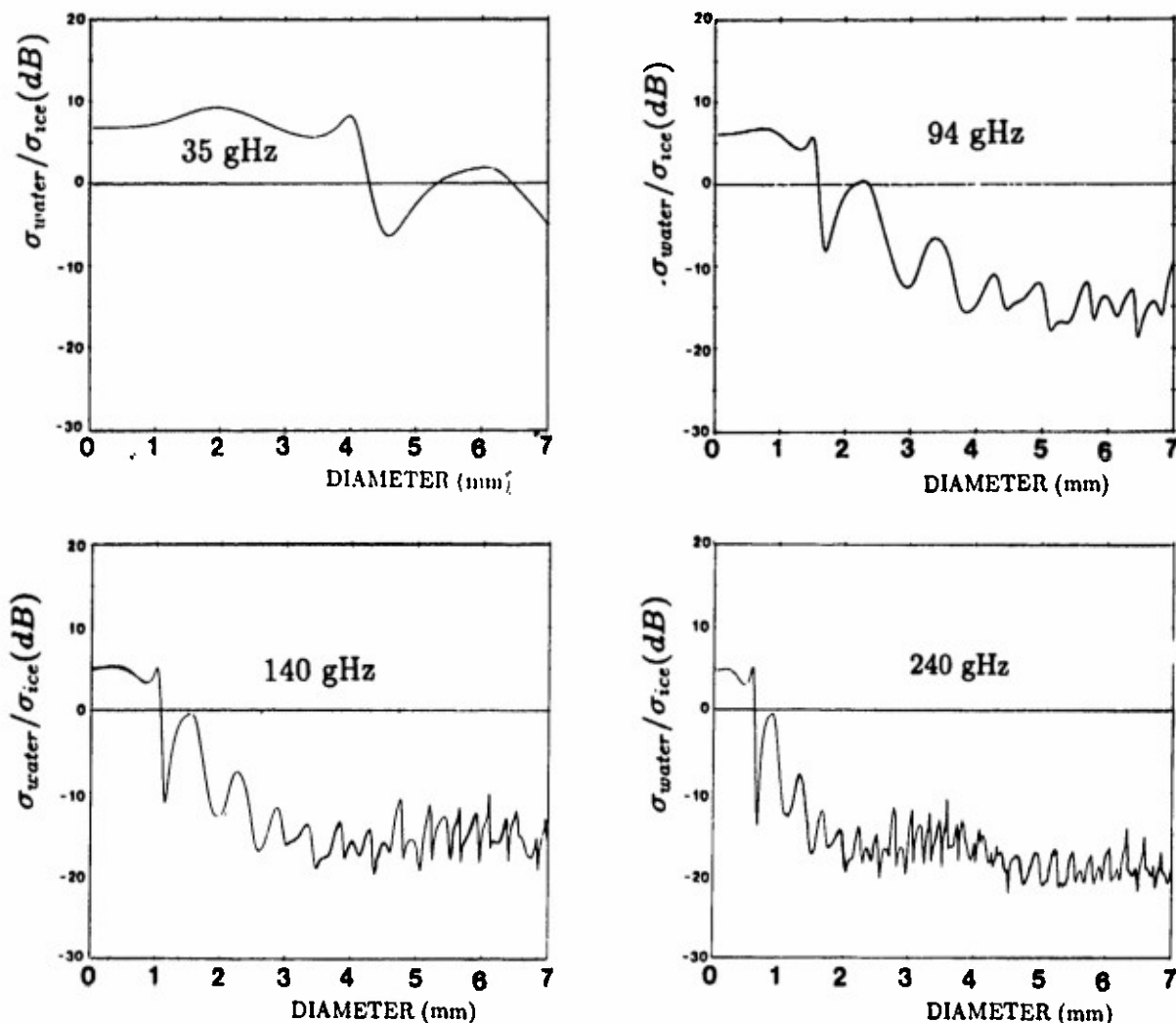


FIG. 5. Ratio (in decibels) between backscattering cross section of water and ice spheres as a function of diameter at the indicated radar frequencies.

vective storms may exhibit a radar reflectivity greatly exceeding that of intense rainfall.

4. Radar reflectivity of rain at millimeter wavelengths

The contribution, $d\eta$, to the radar reflectivity, η , arising from drops with a diameter between D and $D + dD$ is given by

$$d\eta = N(D)\sigma(D)dD \quad (9)$$

where $\sigma(D)$ is the backscattering cross section as a function of D . Assuming a M-P drop-size distribution for $N(D)$, $d\eta/dD$ was calculated with the results presented in Fig. 6 for the 35, 94, 140, and 240 GHz frequencies, for a rain intensity of 40 mm h^{-1} ($N_0 = 0.08 \text{ cm}^{-4}$, $\Lambda = 19 \text{ cm}^{-1}$). These results reflect the behavior of the Mie function and clearly show the predominant contribution to radar reflectivity of a relatively narrow

range of raindrop diameters. The maximum contribution occurs at approximately $D = 2.5 \text{ mm}$ at 35 GHz. At 94 GHz, the contribution to reflectivity exhibits a narrow peak around $D = 1 \text{ mm}$ and another weaker maximum at $D \approx 2.1 \text{ mm}$. At 140 and 240 GHz, several closely spaced maxima occur within the drop-size range for which significant drop concentration exists, but the average contribution extends from approximately 0.3 to 3 mm diameter. This is particularly noticeable at 240 GHz.

The radar reflectivity computed as

$$\eta = \int_0^{\infty} N(D)\sigma(D)dD \quad (10)$$

using a M-P drop-size distribution and $\sigma(D)$ values derived from Mie functions, is presented as a function of rain intensity for the 35, 140, and 240 GHz frequencies in Fig. 7. Also indicated in Fig. 7 is the cm-

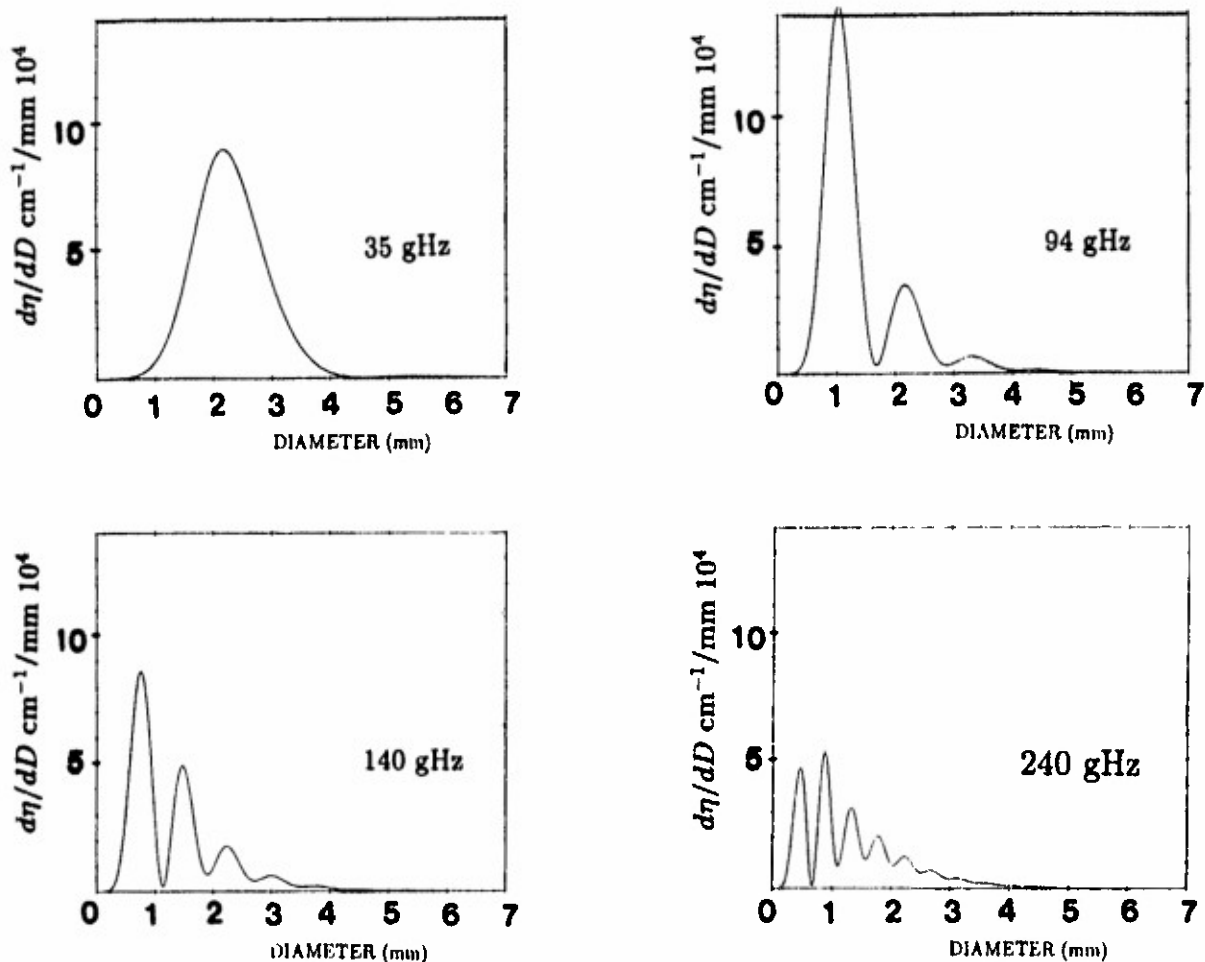


FIG. 6. Contribution $d\eta/dD$ to radar reflectivity, as a function of raindrop diameter in a M-P rainfall with $\Lambda = 19$ ($R = 40 \text{ mm h}^{-1}$).

pirical relationship between η and R at 35 GHz proposed by Wallace (1987) as a least squares fit of experimental data. Wallace's 35 GHz data agree well with the theoretical computations, which supports the selection of a M-P distribution here.

The influence of N_o on the η versus R relationship is shown in Fig. 8, which presents the η versus R function at 94 GHz for three N_o values: 0.014 (Joss "thunderstorm distribution"), 0.08 (original M-P distribution), and 0.3 (Joss "drizzle distribution"). Below $R = 0.01 \text{ mm h}^{-1}$, Rayleigh scattering dominates so that η is proportional to $(N_o)^{-0.469} R^{1.47}$. Around $R = 0.1 \text{ mm h}^{-1}$, η becomes fairly independent of N_o and, above 1 mm h^{-1} , the effect of N_o is reversed since an increase of that parameter is now associated with an increase of η . A similar behavior is observed at 35 GHz, but the independence from N_o is reached for a 20–30 mm h^{-1} rain intensity instead of 0.1 mm h^{-1} at 94 GHz. The least squares fit to 94 GHz experimental data presented by Wallace (1987) is also shown and is seen to fall between the $N_o = 0.08$ and the $N_o = 0.3$ curves. This suggests that, for the set of data used by Wallace, the mean N_o is probably between these two values.

For a 0.1 mm h^{-1} rain intensity, the radar reflectivity at 35 GHz (still approximately 40 dB above that at 3 GHz) is approximately 14, 15, and 16 dB lower than that at 94, 140, and 240 GHz, respectively. The radar reflectivity at 94 GHz, 140 GHz, and 240 GHz is nearly the same for a 0.3 mm h^{-1} rainfall but still 10 dB more than that at 35 GHz. For a 10 mm h^{-1} rainfall, the radar reflectivity at all the selected frequencies appears to be almost identical (within 2 dB). Here η can be converted into the familiar equivalent radar reflectivity factor, Z_e , which is defined by the Rayleigh scattering value that would produce the same reflectivity:

$$Z_e = 10^{12} \eta \lambda^4 / (|K|^2 \pi^5) \quad (11)$$

where Z_e is the $\text{mm}^6 \text{ m}^{-3}$ and η in cm^{-1} . For a 100 mm h^{-1} rainfall, Z_e values are approximately 40 dBZ_e at 35 GHz, 30 dBZ_e at 94 GHz, 20 dBZ_e at 140 GHz, and 10 dBZ_e at 240 GHz, compared to more than 50 dBZ at centimeter waves.

Indeed, departure from Rayleigh scattering at millimeter waves results in compression of the radar reflectivity dynamic range. For a rain intensity variation

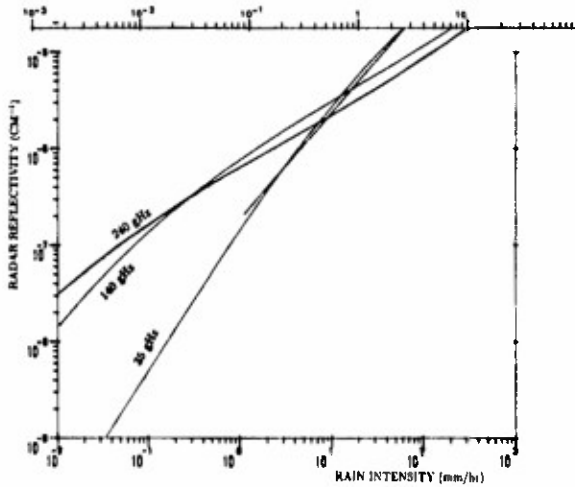


FIG. 7. Radar reflectivity of a M-P rainfall as a function of rain intensity at the indicated radar frequencies. The liquid water derived from the drop-size distribution is also indicated in the upper scale. The dashed line shows the empirical function proposed by Wallace (1988) as a fit to 35 GHz experimental data.

of 0.1 to 100 mm h⁻¹ (associated with a 45 dB variation of η at centimeter waves), η varies by 37 dB at 35 GHz, 22 dB at 94 GHz, 19 dB at 140 GHz, and 16 dB at 240 GHz. These results should not be interpreted as a failure of the short millimeter waves to probe a wide range of rainfall intensity but rather as requiring better accuracy in the reflectivity measurement. The mean $d(\log R)/d(\log \eta)$ slope, which changes by a factor of two from 35 GHz to 94 GHz, indicates that a 1 dB uncertainty in radar reflectivity measurements produces a mean uncertainty in the estimate of rain intensity of 15 percent at 35 GHz and 30 percent at 94 GHz. The $\log R$ versus $\log \eta$ function is not linear so that, for the same dB uncertainty, the variance of the rain intensity estimate is greater (smaller) than the mean value for high (light) rain intensity. Incidentally, the smaller range of η values may remove the need for a logarithmic compression receiver, which may be considered as an advantage. Nevertheless, the primary concern with the reliability of η quantitative measurements at millimeter waves is signal attenuation.

5. Radar reflectivity of ice at millimeter wavelengths

The structure of ice crystals and snowflakes is complex and certainly far from being spherical so that their radar cross section cannot be evaluated theoretically using the simple Mie solution. The main purpose of this paper is to calculate radar reflectivity on the basis of Mie scattering functions and specified drop-size distributions and not to consider empirical fits of observational data except if compared with theoretical computations. Dry, solid ice hailstones that have a near-spherical shape can be treated as ice spheres, at least as a first approximation of their scattering character-

istics. Assuming a known hailstone size distribution, radar reflectivity can thus be calculated theoretically. To introduce the basic difference between hail and rain backscattering at millimeter wavelengths, Fig. 9 shows the density distribution of radar reflectivity as a function of particle diameter, $d\eta/dD$, for both ice spheres (solid ice, applicable to dry hailstones) and raindrops, assuming an exponential size distribution for both ice and water with $N_0 = 0.08 \text{ cm}^{-4}$ and $\Lambda = 15 \text{ cm}^{-1}$. At 35 GHz, most of the contribution to radar reflectivity comes from 1 to 4 mm diameter raindrops with water drops having consistently more reflectivity than ice spheres. At 94 GHz, water raindrops having a diameter smaller than 1.5 mm are still better scatterers compared to ice particles of the same size but, for larger diameters, the contribution to η by ice significantly exceeds that from water. This effect is more pronounced at 140 and 240 GHz with ice now showing an overwhelming contribution.

In the data shown in Fig. 9, the $\Lambda = 15 \text{ cm}^{-1}$ exponential slope, although smaller than the $\Lambda = 19 \text{ cm}^{-1}$ selected in Fig. 6, still virtually prevents particles larger than $D = 7\text{--}8 \text{ mm}$ to contribute significantly to radar reflectivity. Hailstones can grow to a much larger size than raindrops. For instance, Douglas (1964) reported that observations of a typical hailstone size distribution can be represented by the following expression:

$$N(D)/M = 32.2 \exp(-3.09D) \quad (12)$$

where $N(D)$ is the hailstone concentration in number per cubic meter and M is the hailstone's water content in grams per cubic meter. In order to understand the advantage of using a size distribution normalized to

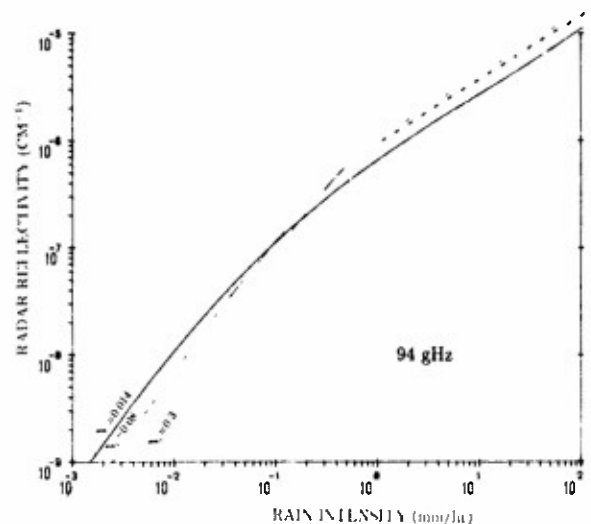


FIG. 8. Radar reflectivity, η , as a function of rain intensity, R , for exponential drop-size distributions with different N_0 . Frequency is 94 GHz. The dashed line shows the η versus R empirical relationship proposed by Wallace on the basis of 94 GHz experimental data.

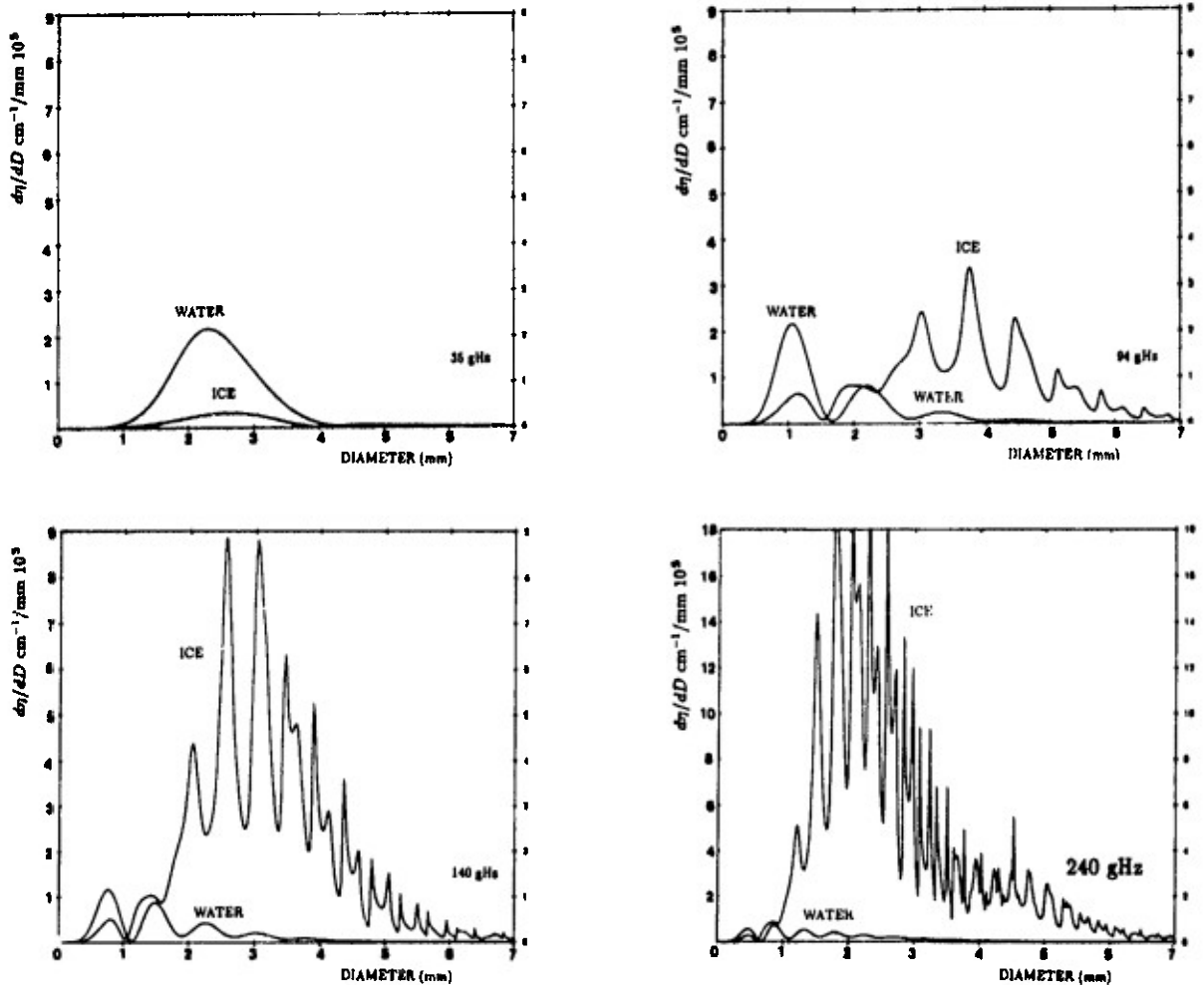


FIG. 9. Contribution to radar reflectivity (labeled "ice") as a function of hailstone diameter with a $\Lambda = 15$ M-P drop-size distribution. The curves labeled "water" show the same calculations assuming raindrops of the same size.

water content, let us assume $N(D) = N_0 \exp(-\Lambda D)$ and express M as a function of N_0 and Λ in the manner discussed above and inserting the ice density, δ . We have:

$$N(D)/M = (\exp(-\Lambda D)\Lambda^4)/(\delta\pi). \quad (13)$$

Therefore, the primary advantage of the Douglas' distribution is that it is independent of N_0 . Incidentally, comparing Eqs. (12) and (13) indicates that Douglas selected a $\delta = 0.9$ value that is acceptable for dry ice. The normalization to hail water content is a very useful concept that can be extended to calculating the ratio, η/M , represented by

$$\eta/M = (\Lambda^4/\delta\pi) \int_0^\infty [\exp(-\Lambda D)\sigma(D)dD] \quad (14)$$

which is only function of Λ . The η/M values for ice calculated using (14) are presented in Fig. 10 as a function of Λ for the 35, 94, 140, and 240 GHz frequencies. The Λ domain extends from 2 to 1000. The large Λ

values are not realistic for hail (or even for rain), but they indicate the tendency of the functions to reach a Λ^{-3} slope arising from $\eta/M = 0.07|K|^2\Lambda^{-3}\lambda^{-4}$, an expression that is applicable to Rayleigh scattering. In Fig. 10, η/M is also shown for a 10-cm wavelength assuming that all hailstones are Rayleigh scatterers, which is really applicable only to diameters smaller than approximately 3 cm. All the η/M versus Λ functions at millimeter waves exhibit a maximum for $\Lambda \approx 15 \text{ cm}^{-1}$ but this is not the case for the $\lambda = 10 \text{ cm}$ function that increases monotonically for decreasing Λ values so that, at $\lambda = 10 \text{ cm}$, the largest hailstone sizes produce the highest radar reflectivity per water content. Figure 10 indicates that, at millimeter wavelengths, ice spheres having a relatively small size (e.g., size distributions with $\Lambda = 15 \text{ cm}^{-1}$) yield a greater radar reflectivity per liquid water content than that produced by the very large hailstones with the size distribution ($\Lambda = 3.09 \text{ cm}^{-1}$) quoted by Douglas (1964). At 94 GHz and $\Lambda = 15 \text{ cm}^{-1}$, $\eta = 1.5 \cdot 10^{-5} \text{ cm}^{-1}$ (approximately 40 and 10 dB more than that observed

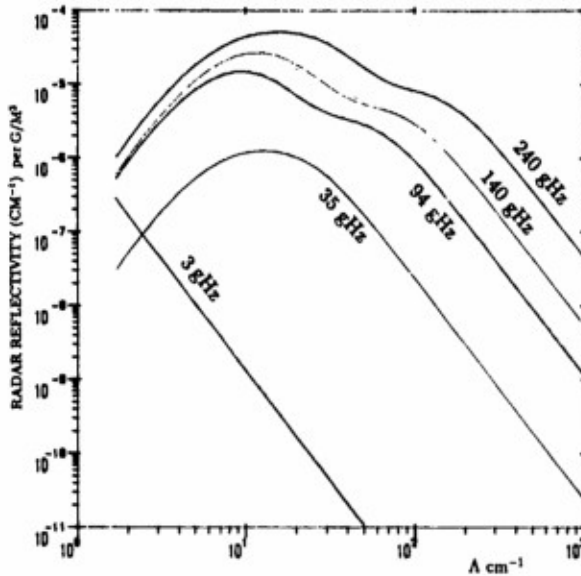


FIG. 10. Radar reflectivity at the indicated radar frequencies of a medium composed of hailstones with an exponential size distribution $N = N_0 \exp(-AD)$, as a function λ . The radar reflectivity based on Rayleigh scattering at 3 GHz is also shown.

at 3 and 35 GHz, respectively), a value still 10 dB greater than that observed for rain with the same λ and N_0 ($\sim 200 \text{ mm h}^{-1}$ rainfall intensity). In this context, medium size hail and graupel remain the strongest backscattering medium at millimeter waves. Assuming a very high value of 10 g m^{-3} for M , a maximum hail radar reflectivity of approximately $2 \times 10^{-4} \text{ cm}^{-1}$ may be observed at 94 GHz for a size distribution approaching that of the graupel typically found a few kilometers above the freezing level in a convective storm. However, for very large size hail such as quoted by Douglas (1964), the maximum radar reflectivity will be reduced to approximately $3 \times 10^{-5} \text{ cm}^{-1}$.

6. Doppler spectrum at vertical incidence

The data shown in Fig. 6 indicate that the σ_{Mie} versus D oscillations should be observable using a millimeter wave Doppler radar probing rainfall in a vertically pointing radar mode. The Doppler spectrum obtained in these conditions is the density distribution of the radar reflectivity as a function of raindrop velocity. If there is no air velocity contribution the raindrop's vertical velocity producing the Doppler shift is a unique and known function of its diameter, so that the radar reflectivity density distribution can be easily changed from diameter to velocity intervals and expressed as a function of velocity (Lhermitte 1988b).

The Doppler spectrum at vertical incidence is the density of radar reflectivity as a function of the particle vertical velocity V , $S(V) = d\eta/dV$ and can be expressed by $S(V) = [N(D)\sigma(D)]dD/dV$. Using the Mie func-

tions, the raindrop's vertical velocity versus diameter function in Eq. (6) for $V(D)$, and a M-P drop-size distribution for $N(D)$ a theoretical representation of the Doppler spectrum observed at vertical incidence in a rainfall can be achieved. The results for $\lambda = 19 \text{ cm}^{-1}$ (40 mm h^{-1} rain intensity according to a M-P drop-size distribution) are presented in Fig. 11 for 35 and 94 GHz, and in Fig. 12 for 140 and 240 GHz. The Doppler spectrum at 35 GHz fails to show even the first Mie scattering minimum. The spectrum at 94 GHz clearly shows the first minimum at 5.9 m s^{-1} and possibly two others at 7.9 and 8.8 m s^{-1} . At 140 and 240 GHz, two or three minima can be identified even in a noisy spectrum.

It must be remembered that, even if there is no mean velocity bias arising from the presence of vertical air velocity, the vertical velocity of a raindrop may include a random component due to air turbulence and oscillation of raindrop shape. This should smear an observed spectrum, thus essentially reducing the relative amplitude of closely spaced spectral minima and maxima (Lhermitte 1988b). Shape oscillations are more severe for raindrops having a diameter greater than approximately two millimeters. Hence, the spectrum smearing caused by shape oscillations will primarily affect the high velocity part of the spectrum.

Experience acquired from stratiform rain observations with a 94 GHz Doppler radar at vertical incidence indicates that the first Mie minimum can always be identified if the rainfall intensity is greater than approximately 5 mm h^{-1} . Figure 13 shows a Doppler spectrum observed in a 8 mm h^{-1} rainfall at 1.2 km altitude. A spectral dip at 6.2 m s^{-1} , in good agreement with the terminal velocity of a 1.57 mm raindrop at the altitude considered (1.2 km), is clearly seen. These results suggest that Mie oscillations in a Doppler spectrum can be used to effectively test the relationship between raindrop vertical velocity and size, and as a method for the measurement of both air vertical velocity and drop-size distribution (Lhermitte 1988h).

In the case of ice particles the first minimum of the Mie backscattering function is not as deep but should still be easily identified in a vertical incidence Doppler spectrum. It appears at $D = 4 \text{ mm}$ at 35 GHz and $D = 1.5 \text{ mm}$ at 94 GHz. Therefore a 35 GHz Doppler radar used in a vertically pointing mode may be useful in the measurement of vertical velocity of small hail or graupel in a convective storm. Using the method for the identification of large size hail may be done more effectively at 9 GHz, for which the first Mie minimum appears at approximately 1.5 cm.

7. Mean Doppler and spectral variance at vertical incidence

The mean Doppler vertical velocity, \bar{V}_d , which is a parameter useful for the expression of mean velocity components from Doppler data, is given by

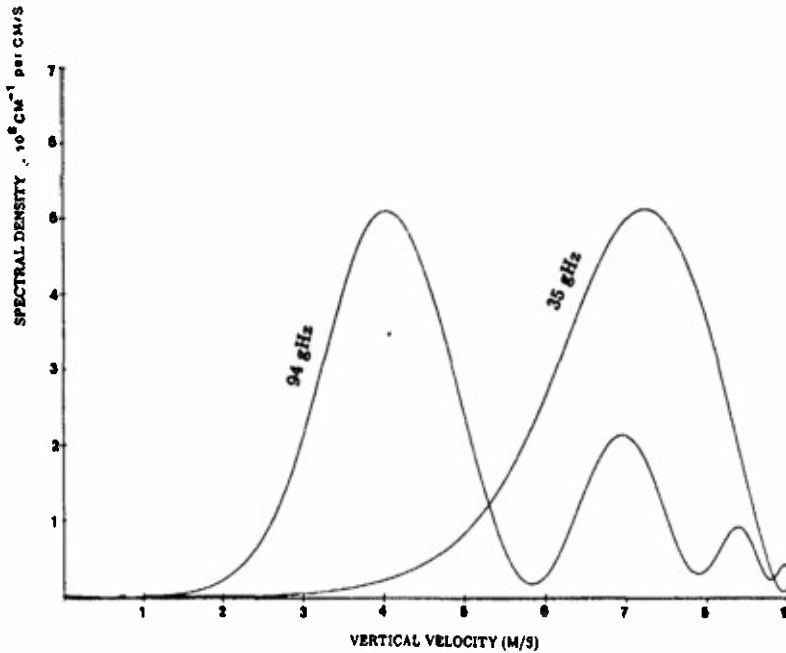


FIG. 11. Theoretical Doppler spectrum at vertical incidence based on Mie scattering functions, a Gunn-Kinzer raindrop terminal velocity model, and a M-P drop-size distribution with $\Lambda = 19$. Frequencies are 35 and 94 GHz.

$$\bar{V}_d = \frac{\int_0^\infty [N(D)\sigma(D)V(D)dD]}{\int_0^\infty [N(D)\sigma(D)dD]}, \quad (15)$$

where $N(D)$ is the drop-size distribution and $V(D)$ the relationship between raindrop diameter and fall speed. It is clear from (15) that \bar{V}_d is independent of N_o so that it is only a function of Λ . Here \bar{V}_d was calculated as a function of Λ using Eq. (5) with an ex-

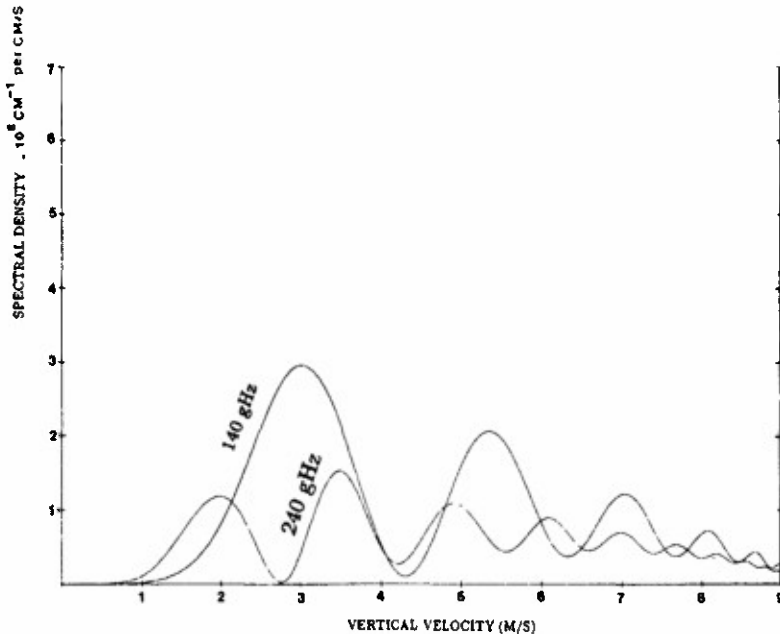


FIG. 12. As in Fig. 10, but for 140 and 240 GHz.

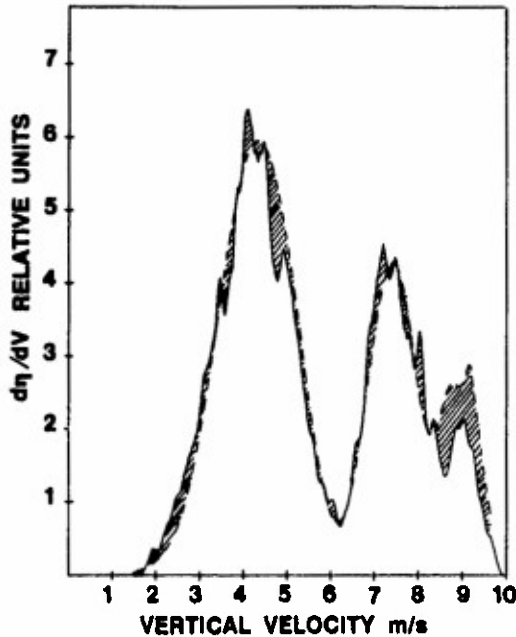


FIG. 13. Doppler spectrum actually observed with a 94 GHz Doppler radar at vertical incidence in a 8 mm h^{-1} rainfall. The theoretical spectrum calculated using the Mie function and a M-P drop-size distribution is also shown by the dashed line.

ponential drop size distribution, Eq. (6) for $V(D)$, and Mie functions for $\sigma(D)$. For each value of Λ , the rain intensity normalized to N_0 , R/N_0 , and the radar reflectivity normalized to N_0 , η/N_0 , were also computed. The computations were repeated at 35, 94, 140, and 240 GHz. The results are presented in Fig. 14 as $\log(\bar{V}_d)$ versus $\log(Z_e/N_0)$, with Z_e given by Eq. (9). The use of Z_e provides a normalization of η so that the results are independent of the selected frequency in the Rayleigh region.

For low radar reflectivity, $\bar{V}_d = 2.31Z^{1/7}$, which indicates that Rayleigh approximation is applicable (Λ is proportional $Z^{1/7}$) and also that for D between 10μ and 1 mm , the terminal velocity of a small size raindrop is roughly proportional to its diameter, D , as shown by the Gunn and Kinzer (1949) data. Still assuming Rayleigh scattering, but for greater D for which V is not proportional to D , the mean $\log(\bar{V}_d)$ versus $\log Z_e/N_0$ is no longer a linear function but $\bar{V}_d \approx 2Z^{1/8.8}$ is a reasonable fit. This expression is significantly different from the $\bar{V}_d = 2.88Z^{1/14}$ obtained by Rogers (1964) using the Spilhaus relationship mentioned before for $V(D)$. The Spilhaus function exhibits large deviations from the G-K data for both very small and very large raindrops and that can explain the discrepancy. On the contrary, the $V(D)$ function (6) is in much better agreement with the G-K data, with significant differences only localized in the Stokes' regime region (below $D = 10 \mu\text{m}$) for which the terminal velocity is proportional to D^2 . The $\log(\bar{V}_d)$ versus $\log(R/N_0)$ function is shown in Fig. 15 together with

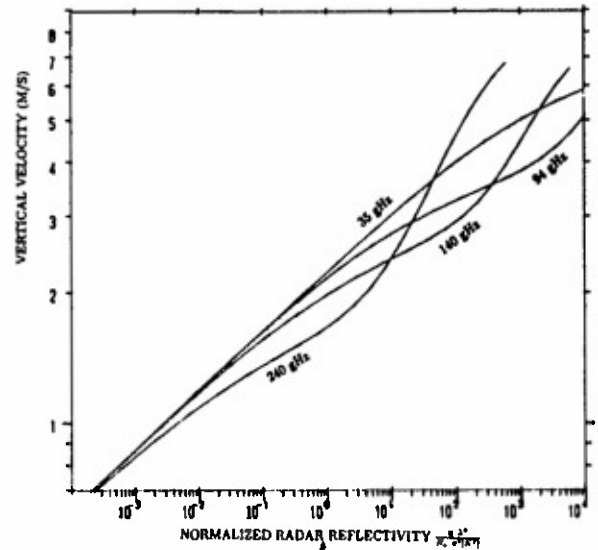


FIG. 14. Mean Doppler velocity at vertical incidence, (\bar{V}_d) , as a function of radar reflectivity normalized to wavelength and the $|K|^2$ term: Z_e/N_0 , at the indicated frequencies. Drop-size distribution is the M-P function and the drop terminal velocity is derived from the relationship (6) in the text.

the Rayleigh scattering solution applicable to centimeter wavelengths.

The calculations above show that, for high rain intensity, \bar{V}_d is significantly smaller at millimeter waves than at centimeter waves, as a consequence of the Mie backscattering cross section being significantly smaller than Rayleigh for large raindrops. For a rainfall intensity above 10 mm h^{-1} , the mean Doppler value at 35 GHz is approximately 1 m s^{-1} smaller than that calculated at centimeter waves for which Rayleigh scat-

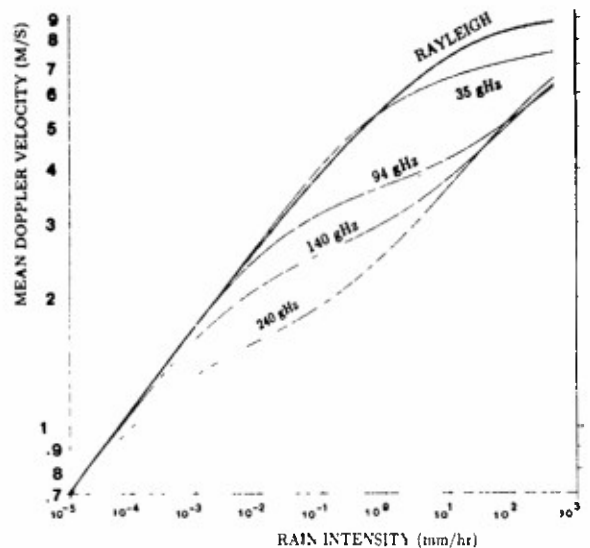


FIG. 15. Same as Fig. 14 but expressed as a function of rain intensity with $N_0 = 0.08$. The curve labeled Rayleigh is the solution for Rayleigh scattering applicable to centimeter wave radars

tering applies. At 94, 140, 240 GHz and for high rain intensity, $\overline{V_d}$ is approximately 3 m s⁻¹ smaller than the Rayleigh scattering value (5 m s⁻¹ instead of 8 m s⁻¹ for a 100 mm h⁻¹ rainfall).

We also computed the spectral variance given by $\overline{V_d^2} - (\overline{V_d})^2$. $\overline{V_d^2}$ is obtained by replacing $V(D)$ by $V^2(D)$ in Eq. (15). The spectral variance values, which are again independent of N_o , are plotted against rain intensity assuming a M-P drop-size distribution with $N_o = 0.08$ (see Fig. 16). At 35 GHz, the spectral variance is nearly the same as that obtained using Rayleigh scattering. At higher frequencies, the spectral variance is less than the Rayleigh value for rain intensity lower than 1 mm h⁻¹, but increases markedly for a higher rain intensity. This can be explained by the bimodal or trimodal nature of the spectra seen in Figs. 11 and 12.

8. Millimeter wave attenuation by atmospheric gases and hydrometeors

Atmospheric absorption in the windows is due primarily to the skirts of water vapor lines. For a specific humidity of 0.25 g m⁻³, the absorption coefficient is 0.04, 0.042, 0.05, and 0.09 dB km⁻¹, at 35, 94, 140, and 240 GHz, respectively. For a specific humidity of 25 g m⁻³, absorption values for the same frequencies are approximately 0.35, 2.1, 5.0, and 13 dB km⁻¹. Humidity is concentrated at low altitude in the earth atmosphere so that atmospheric gases absorption is important only for ground based equipment acquiring data with low elevation angles.

The main consideration in the evaluation of the performance of a millimeter wave meteorological radar is the attenuation of millimeter wave radiation by clouds or precipitation.

TABLE 2. Absorption coefficients α_{GHz} at 35, 94, 140, 240 GHz in dB km⁻¹ per g m⁻³ of liquid water at the indicated temperatures.

Temperature	α_{GHz}			
	α_{35}	α_{94}	α_{140}	α_{240}
0°C	0.99	4.9	7.66	9.68
10°C	0.80	4.2	7.46	11.05
20°C	0.65	3.75	7.26	14.06

Even at millimeter wavelengths, Rayleigh scattering or absorption generally applies to cloud droplets. This implies that contribution from scattering to attenuation is negligible and that the attenuation coefficient, $\alpha_a = \int N(D)Q(D)dD$, in decibels per kilometer per gram per cubic meter (one-way), is given by

$$\alpha_a = 8.18 \text{Im}(-K)/\lambda. \tag{16}$$

The results of these computations for liquid water are shown in Table 2.

If the hydrometeors are not very small compared to the radar wavelength, expression (16) is not valid and α must be calculated using Q_a from Mie functions. Also the scattering cross section, Q_s , becomes significant and signal attenuation calculations must be based on the extinction cross section $Q_t = Q_a + Q_s$. Figures 17 and 18 show the absorption and scattering cross sections Q_a and Q_s , respectively, as a function of D at the selected frequencies. In the Rayleigh region ($D \leq 0.1$ mm) $Q_a = [\pi^2 D^3 \text{Im}(-K)]/\lambda$ and thus is proportional to raindrop mass. For larger $D/\lambda \geq 2.5$, Q_a exceeds the Rayleigh absorption value and exhibits a maximum deviation from Rayleigh for $D/\lambda \approx 2.8$ (see

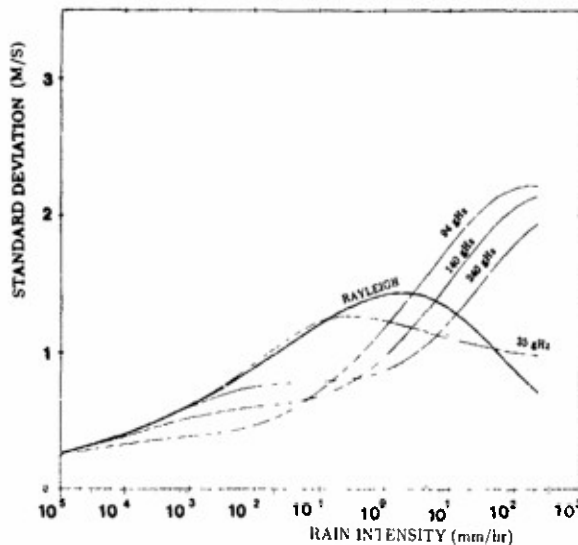


FIG. 16. As in Fig. 15 but for the square root of spectral variance

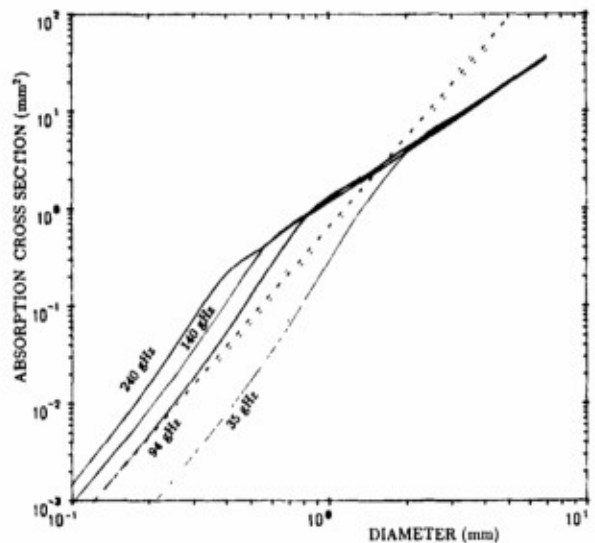


FIG. 17. Absorption cross section computed from the Mie equations at the indicated frequencies as a function of diameter for liquid water raindrops (temperature 10°C). The dashed line shows the 94 GHz solution in the hypothetical case of Rayleigh scattering.

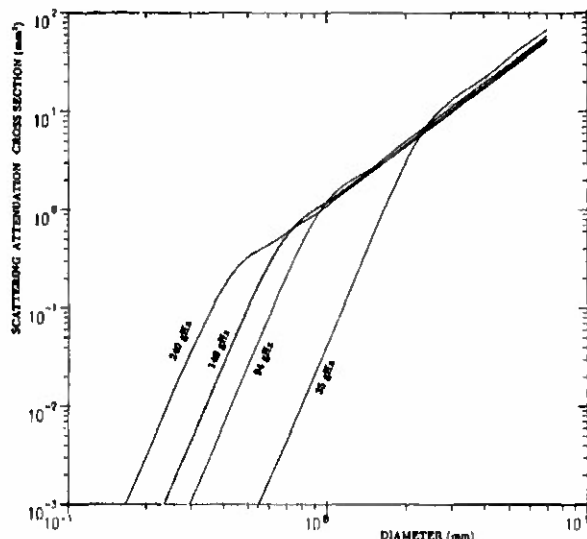


FIG. 18. As in Fig. 17 but for the scattering cross sections.

dashed line indicating Rayleigh absorption at 94 GHz). Above $D/\lambda \approx 5$, Q_a becomes markedly smaller than its Rayleigh value. Indeed, above $D = 1$ mm at 94, 140, 240 GHz, and above $D = 2$ mm at 35 GHz, Q_a is nearly independent of the radiation frequency.

The raindrop size contribution to attenuation is illustrated in the data presented in Fig. 19, which show the attenuation coefficient per gram per cubic meter of liquid water content as a function of the raindrop diameter, calculated at 35, 94, 140, and 240 GHz (0°C water temperature). For small drop diameter (less than $100 \mu\text{m}$ for example), the attenuation coefficient is equal to the Rayleigh absorption values shown in Table 2. However, for a greater raindrop diameter, the attenuation coefficient increases, reaches a maximum for $D/\lambda \approx 3$, greatly exceeding Rayleigh absorption, and then decreases slowly to a value smaller (except for 35 GHz) than that calculation for Rayleigh absorption. The attenuation peak occurs at approximately: $D = 2.5$ mm (35 GHz), $D = 0.9$ mm (94 GHz), $D = 0.6$ mm (140 GHz), and $D = 0.4$ mm (240 GHz).

The attenuation coefficient, α given by

$$\alpha = \int_0^\infty [Q_t(D)N(D)dD] \quad (17)$$

was computed using a M-P distribution and Q_t evaluated from the Mie functions. The results, which are expressed as a function of rain intensity calculated using the same drop-size distribution and the raindrop's terminal velocity relationship (6), are presented in Fig. 20 for a 20°C water temperature. In the Rayleigh region α is proportional to $R^{0.84}$, which agrees with Eq. (8). At 35 GHz, the expression $\alpha \approx 0.2R$ (R in millimeters per hour and α in decibels per kilometer) applies to a wide rain intensity domain and is in good agreement with observations. However, at 94 GHz and above, the

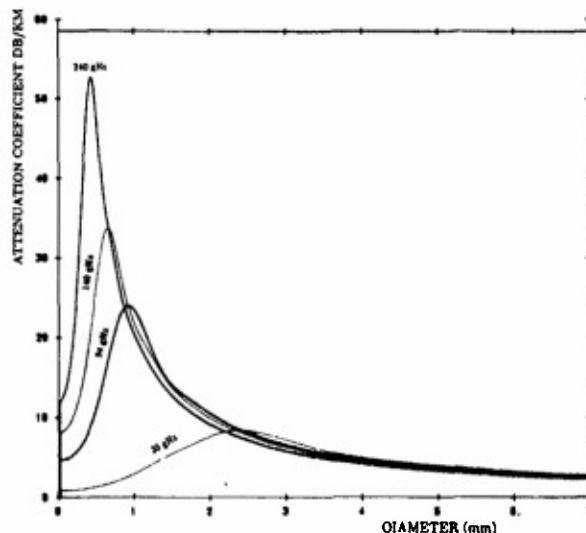


FIG. 19. Attenuation coefficient in dB km^{-1} for 1 g m^{-3} of liquid water composed of the same diameter as a function of that diameter, at the indicated frequencies. The starting value (small diameter) is the Rayleigh absorption value.

$\log \alpha$ versus $\log R$ relationship becomes markedly non-linear for high rain intensity, which suggests that the $\alpha = aR^b$ form proposed by Olsen et al. (1978) is not an acceptable model at these very short wavelengths. Figure 20 also shows that, for very high rain intensity, the attenuation coefficient tends to be independent of frequency. For a 10 mm h^{-1} rainfall, the theoretical value of α varies from 2 dB km^{-1} at 35 GHz to approximately 7 dB km^{-1} at 94 GHz and $8\text{--}9 \text{ dB km}^{-1}$

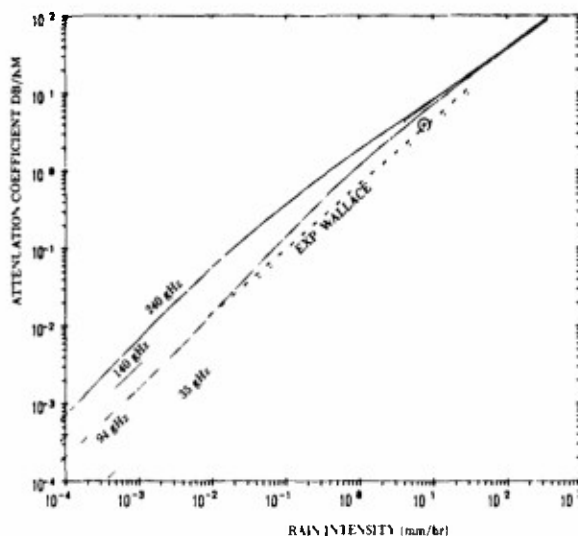


FIG. 20. Attenuation coefficient as a function of rain intensity at the 35, 94, 140, and 240 GHz frequencies. The dashed line indicates the relationship proposed by Wallace at 94 GHz on the basis of a least squares fit to experimental data. The circled cross shows the 94 GHz measurement by Lhermitte (see text)

at 140 and 240 GHz. These theoretical values of signal attenuation at millimeter waves are derived from single particle Mie cross sections. Forward scattering and possible multiple scattering are not included in the Q cross section.

To explore the validity of the above treatment, the theoretical results have been compared to actual measurements of attenuation. Two reliable measurements of signal attenuation at 94 GHz were considered. One was a set of attenuation measurements reported by Wallace (1988) on the basis of which a linear least squares fit between $\log \alpha$ and $\log R$ was proposed. The other data was a carefully done measurement of attenuation in a stratiform rain in which the drop-size distribution and the rain intensity were also measured (Lhermitte 1988b). Both data are presented in Fig. 20 (see caption). The theoretical calculations which, incidentally, do not seem to be significantly influenced by temperature, agree well with the functions proposed by Wallace for very low rain intensity but overestimate the Wallace function for $R \geq 0.1 \text{ mm h}^{-1}$ (7 dB km^{-1} calculated instead of 4 dB km^{-1} measured at 10 mm h^{-1}). Wallace's data are also in close agreement with Lhermitte's data obtained in a 8 mm h^{-1} steady rain for which both rain intensity and drop-size distribution were measured (6 dB km^{-1} theoretical instead of 3.5 dB km^{-1} measured). These results point out the need for more experimental data on signal attenuation by precipitation at 94 GHz and above.

If α can be expressed as a function of η , this offers a method for signal attenuation correction. The α versus η relationship was investigated, assuming an exponential drop-size distribution and computing both α and η as a function of Λ and for different values of N_0 . The α versus η functions obtained using this method are shown in Fig. 21 for a 94 GHz frequency. In the Rayleigh region, α is proportional to $(N_0)^{3/7} \times \eta^{4/7}$, which indicates a significant dependency on N_0 . However, Fig. 21 shows that the N_0 control on η is significantly reduced for higher η values, and that for $\eta \approx 10^{-6} \text{ cm}^{-1}$ ($\alpha \approx 1 \text{ dB km}^{-1}$) the relationship between α and η is virtually independent of N_0 . The same behavior is found at 35 GHz (not shown) but the independence from N_0 appears for much larger η and α value.

9. Conclusion

Because of the typical low power and antenna size of a millimeter wave radar, the choice of a millimeter wavelength is very attractive for space platform applications. A 0.2° beamwidth and a -20 dBZ sensitivity for a spaceborne radar at an altitude of 300 km would require a 6 m antenna and 100 watts average power at 15 GHz, compared to 1 m and 10 watts at 95 GHz.

Signal attenuation by clouds and precipitation is a serious problem associated with airborne or spaceborne millimeter wave operation (Meneghini et al. 1986).

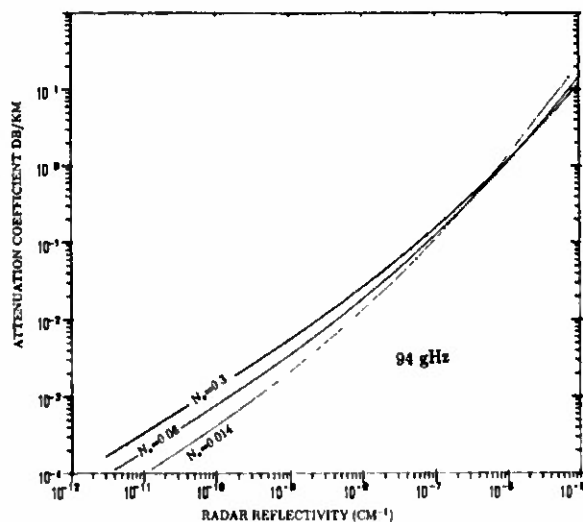


FIG. 21. Attenuation coefficient as a function of radar reflectivity using exponential drop-size distributions with different N_0 . Frequency is 94 GHz.

Measuring precipitation intensity directly (based on radar reflectivity-rain intensity relationship) may be unachievable at very short wavelengths, but attenuation is already a problem at 15 GHz for instance, for which the attenuation coefficient is approximately $0.12 \text{ dB per mm h}^{-1}$ of rain intensity, thus preventing reliable measurements of intense rainfall.

The answer to the question of feasibility of ground rainfall measurements from space may be to derive rainfall intensity empirically from other storm parameters such as the altitude of—and radar reflectivity gradients at—cloud tops and also precipitation penetration depth, using precipitation structure models. This approach is somewhat analogous to the empirical methods used in the treatment of satellite IR data to infer earth's surface precipitation. However, the radar approach relies on much more elaborate information on backscattering signal intensity gradients in the upper storm region, rather than only the upwelling radiation signal at the storm top.

Recently, a 94 GHz spaceborne radar was proposed (Lhermitte 1989). Because of its low power requirement and small antenna size, the instrument does not rely on complex technology. It is nevertheless capable of providing information on motion fields inside precipitation systems that can be penetrated by the millimeter wave radiation.

Providing some of the background material required for evaluation of ground-based and spaceborne millimeter wave radar performance was the primary incentive for this work. The results yield a basic understanding of the problem and are directly applicable to clouds and relatively weak precipitation. Considering ice particles with complex structure and even large raindrops that are basically oblate when falling will require much more experimental measurements of radar reflectivity

and signal attenuation using ground-based and airborne radars.

Acknowledgments. This work was performed under the Army Research Office DAAL03-86-K-0145 contract monitored by Dr. Walter Flood, whose constant encouragements are deeply appreciated. The Mie functions program source was provided by Dr. D. Brown. Many thanks to Drs. R. Serafin, F. Mark, and P. Willis who reviewed the first version of the manuscript and made helpful comments.

REFERENCES

- Douglas, R. H., 1964: Hail size distributions. *Preprints, 11th Wea. Rad. Conf.*, Amer. Meteor. Soc., 147-149.
- Feingold, G., and Z. Levin, 1986: The lognormal fit to raindrop spectra from frontal convective clouds in Israel. *J. Climate Appl. Meteor.*, **25**, 1346-1363.
- Gunn, R., and G. D. Kinzer, 1949: The terminal velocity of fall for water droplets in stagnant air. *J. Meteor.*, **6**, 243-248.
- Hobbs, P. V., N. T. Funk, R. R. Weiss, J. D. Locatelli and K. R. Biswas, 1985: Evaluation of a 35 GHz radar for cloud research. *J. Atmos. Oceanic Technol.*, **2**, 35-48.
- Joss, J., J. C. Thams and A. Waldvogel, 1968: The variations of raindrop size distribution at Locarno. *Proc. Int. Conf. Cloud Phys.*, 369-373.
- Kessler, E., 1987: Kinematic effect of vertical drafts on precipitation near earth's surface. *Mon. Wea. Rev.*, **115**, 2862-2864.
- Lee, A. C., 1988: The influence of vertical air velocity on the remote microwave measurement of rain. *J. Atmos. Oceanic Technol.*, **5**, 727-735.
- Lhermitte, R., 1987: A 94 GHz Doppler radar for cloud observations. *J. Atmos. Oceanic Technol.*, **4**, 36-48.
- , 1988a: Cloud and precipitation remote sensing at 94 GHz. *IEEE Trans. on Geoscience and Remote Sensing*, **26**, 207-216.
- , 1988b: Observation of rain at vertical incidence with a 94 GHz Doppler radar: an insight on Mie scattering. *Geophys. Res. Lett.*, **15**, 1125-1128.
- , 1989: Satellite-borne millimeter wave Doppler radar. *Proc. Union Radio Scientifique Internationale, Open Symposium, La-Londe-Les-Maures, France.*
- Liebe, H. J., 1985: An updated model for millimeter wave propagation in moist air. *Radio Sci.*, **20**, 1069-1089.
- Marshall, J. S., and W. McK. Palmer, 1948: The distribution of raindrops with size. *J. Meteor.*, **5**, 165-166.
- Meneghini, R., K. Nakamura, C. W. Ulbrich, D. Atlas, T. D. Clem and S. R. Kostic, 1986: Comparisons of methods using data from an air-borne dual-wavelength radar. *Proc. 23rd Conference Radar Meteorology*, Amer. Meteor. Soc.,
- Mie, G., 1908: Beiträge zur Optik trüber Medien, speziell kolloidaler Metall-Lösungen. *Ann. Phys.*, **25**, 377-445.
- Narayanan, R. M., C. C. Borel and R. E. McIntosh, 1988: Radar backscatter characteristics of trees at 215 GHz. *IEEE Transactions on Geoscience and Remote Sensing*, **26**, 217-228.
- Olsen, R. L., D. V. Rogers and D. B. Hodge, 1978: The aR^b relation in the calculation of rain attenuation. *IEEE Transactions on Antennas and Propagation*, **AP-26**, 318-329.
- Omar, J., and H. Sauvageot, 1987: Radar reflectivity of cumulus clouds. *J. Atmos. Oceanic Technol.*, **4**, 264-272.
- Pasqualucci, F., B. W. Bartram, R. A. Kropfli and W. R. Moninger, 1983: A millimeter wavelength dual-polarization Doppler radar. *J. Climate Appl. Meteor.*, **22**, 758-765.
- Paulsen, W. H., P. J. Petrocchi and G. McLean, 1970: Operational utilization of the TPQ-11 cloud-detection radar. Air Force Cambridge Resear. Lab. Paper No. 166, 37.
- Ray, P. S., 1972: Broadband complex refractive index of ice and water. *J. Appl. Opt.*, **11**, 1836-1843.
- Rogers, R. R., 1964: An extension of the Z-R relation for Doppler radar. *Proc. 11th Weather Radar Conference*, 158-161.
- Sekhon, R. S., and R. C. Srivastava, 1971: Doppler radar observations of drop-size distributions in a thunderstorm. *J. Atmos. Sci.*, **28**, 983-994.
- Spilhaus, A. F., 1948: Raindrop size, shape, and falling speed. *J. Meteor.*, **5**, 108-110.
- Ulbrich, C. W., 1983: Natural variations in the analytical form of the raindrop size distribution. *J. Climate Appl. Meteor.*, **22**, 1764-1775.
- Wallace, B., 1988: Millimeter-wave propagation measurements at the ballistic research laboratory. *IEEE Transactions on Geoscience and Remote Sensing*, **26**, 253-258.
- Willis, P., 1984: Functional fits to some observed drop size distributions and parameterization of rain. *J. Atmos. Sci.*, **41**, 1648-1661.

OBSERVATION OF RAIN AT VERTICAL INCIDENCE WITH A 94 GHz DOPPLER RADAR:
AN INSIGHT ON MIE SCATTERING

Roger M. Lhermitte

Rosenstiel School of Marine and Atmospheric Sciences, University of Miami, Fla

Abstract. A new method aimed at differentiating air vertical motion and raindrop terminal velocity in a velocity spectrum observed at vertical incidence identification based on Mie backscattering oscillations occurring within the raindrop size range at the 3.2 mm wavelength. The method is applicable to measurement of downdraft or microburst in rainshafts and drops size distribution in all types of rain.

INTRODUCTION

Recent observations of stratiform precipitation at vertical incidence with a Doppler radar operating at a 94 GHz frequency ($\lambda=3.2$ mm) have revealed a unique capability of the system based on the fact that, at this very short wavelength, the backscattering cross section of a raindrop as a function of its diameter oscillates markedly (Mie scattering). Since they occur within the raindrop size range, the Mie backscattering oscillations create a pattern of maxima and minima in a Doppler spectrum observed at vertical incidence, and thus can serve as a means to identify raindrop size. The occurrence of air vertical velocity, w , merely shifts the Mie oscillation pattern and does not alter its structure. The w shift can be determined by comparing the observed spectrum with a predicted spectrum evaluated assuming $w = 0$. This note presents the new method and some of the results.

The 94 GHz Doppler radar has the following main characteristics: peak power 1 kw; pulse width 200 ns; antenna size 3-foot; beamwidth 0.3°; minimum detectable signal with 3 s integration time -115 dBm. The radar is equipped with a processor providing vertical profiles of mean Doppler velocity and radar reflectivity [Lhermitte, 1987]. In addition, the radar signal containing backscattering phase and amplitude information (coherent video), can be sampled at a selected range gate and continuously recorded. The recorded signal is processed by a micro computer programmed with FFT algorithms to generate power density spectra (Doppler spectra).

DOPPLER SPECTRUM AT VERTICAL INCIDENCE IN RAIN

If a Doppler radar observes falling raindrops at vertical incidence, the Doppler frequency shift arises from the raindrops' vertical velocity, V . V is expressed by $V = V_i + w$, where V_i is the raindrop terminal velocity in still air and w is the air motion. The fall velocity of raindrops has been accurately measured [Gunn and Kinzer, 1948; hereafter referred to as *G-K*]. Although complicated functions have been proposed as a fit to the *G-K* experimental data [i.e. Beard, 1976], we have found that they can be represented to a sufficient degree of accuracy

by: $V_i = V_0[1 - \exp(-(aD^2 + bD)]$, where V_i is in cm/s, D in cm. With $V_0 = 925$ cm/s, $a = 6.8$, and $b = 4.88$, the standard deviation of the above expression from the *G-K* data is less than 3 cm/s in the 0.5 to 6 mm raindrop size range and may be considered as an acceptable fit, possibly reducing the experimental data noise. The *G-K* measurements were made at sea level and these V_i values must be corrected for observations made aloft by $(\rho_0/\rho)^{0.4}$ [Foote and duToit, 1969] where ρ_0 is the air density at sea level and ρ is the air density at the height at which the observations are made. The Doppler spectrum observed at vertical incidence, $S(V) = n(D).dD/dV.\sigma(V)$ can be defined as a density distribution, $d\eta/dV$ of the radar reflectivity, η , with the vertical velocity, V , of the scatterers. The first term contributing to $S(V)$ is the drops size distribution, $n(D) = dN/dD$, a density distribution of the number of raindrops per unit volume as a function of equal diameter D intervals. $n(D).dD/dV$ is the drops size distribution expressed as a function of equal velocity intervals. $n(D)$ can be represented by a simple exponential function $n(D) = N_0 \exp(-\Lambda D)$ proposed by Marshall and Palmer, [1948] (*M-P*), where N_0 is equal to 0.08 cm^{-4} and Λ is a parameter depending on rain intensity. Actual drops size distributions do not agree fully with *M-P* as there are significant departures at the low and high ends of the size spectrum. However, an exponential form is a reasonable fit to any actual size spectrum within $D=1$ mm to $3 \cdot 4$ mm (depending on rain intensity). $\sigma(v)$, is the radar cross section of raindrops as a function of their vertical velocity using: i. σ versus D from Mie scattering tables, and ii. the terminal velocity V_i versus D relationship.

We can thus derive $k.n(D)$ (k is an unknown constant) from the Doppler spectrum $S(V)$ alone. The evaluation of k requires measurement of the radar reflectivity which can be seen as the integral of $S(V)$ over all possible vertical velocities. This method, which was proposed in the early days of meteorological Doppler radar methodology, is severely hindered by the possible presence of air vertical velocity, w , which shifts the $V(D)$ relationship and corrupts particle diameter measurements based on the V_i versus D function. For large raindrops, even a small uncertainty in w produces a very large error in D measurements (at $D=4.5$ mm the error on D is ± 0.4 mm for a $\pm 0.2 \text{ ms}^{-1}$ uncertainty on V_i). Two methods, originally conceived for the purpose of measuring downdraft-updraft from Doppler spectra, were proposed to separate particle terminal velocity and air velocity. The first method is based on estimating the velocity spectrum boundaries [Battan, 1970]; the second relies on a known relationship between the mean Doppler (first moment of the Doppler spectrum) and the radar reflectivity based on an *M-P* assumption for $n(D)$ [Rogers, 1964]. However, none of these methods can yield an acceptable estimate of w if the actual drops size distribution is unknown.

MIE SCATTERING AS MEANS TO MEASURE w

Using a radar operating at a very short wavelength offers a completely new approach to the problem of separating V_i

Copyright 1988 by the American Geophysical Union.

Paper number 8L8088.
0094-8276/88/008L-8088\$03.00

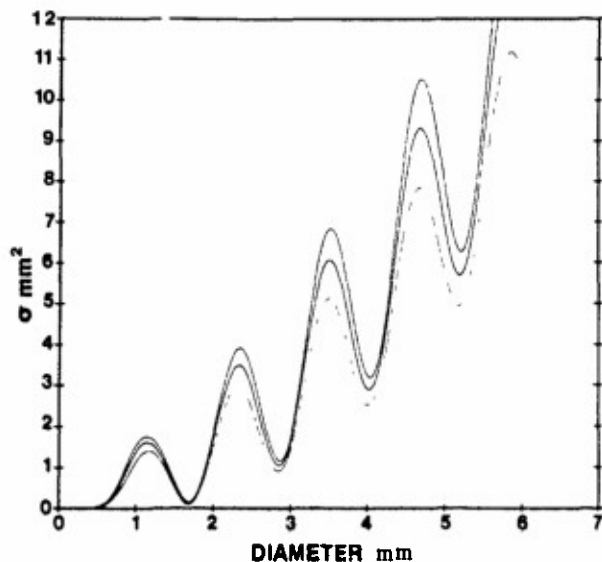


Fig. 1. Backscattering cross section of spherical liquid water drops as a function of their diameter at a 3.2 mm wavelength and for 0, 10, 20° temperatures.

and w , based on the presence of maxima and minima of the backscattering cross section, σ , occurring at well defined raindrop diameters. As seen in Fig. 1, at a 3.2 mm wavelength (droplet temperature 15°C), σ exhibits maxima at $D = 1.0, 2.26, 3.44, 4.62$ mm, and minima at $D = 1.67, 2.86, 4.04,$ and 5.22 mm. These oscillations should modulate the Doppler spectrum observed at vertical incidence and thus can serve as a means for particle size identification. The occurrence of air velocity, w , will merely shift these oscillations in the Doppler frequency scale and should not destroy their integrity. Therefore, comparing an observed Doppler spectrum with a predicted spectrum evaluated from the Mie function should lead to a measurement of w , and then, correcting for w , a measurement of $n(D)$.

Recent rain observations with our millimeter wave radar indeed confirmed that some of these Mie oscillations appear clearly in a Doppler spectrum observed at vertical incidence in moderate to heavy rain conditions. Fig. 2. shows an example of the observed spectra, processed from data recorded on November 30 1987, at Sudbury, Massachusetts. The observations were made at an altitude of 1.3 km in steady rain conditions dominated by a radar "melting hand" (see Fig. 4 captions). Four individual spectra were added to yield the smooth spectrum shown in Fig. 2. Each spectrum was calculated using 4096 complex samples which were recorded at 1 s time interval. The dominant feature of the spectrum is the well defined dip at 6.2 m/s (first Mie minimum for a diameter of 1.67 mm), surrounded by the two maxima at approximately 4 and 7 m/s. Also shown in Fig. 2 is a predicted spectrum based on the Mie function evaluated at the 3.2 mm radar wavelength assuming an exponential drop size distribution with a 15 cm^{-1} slope and a $D=0$ intercept adjusted for best match with the observed spectrum in the 2 to 8 m/s range (1 to 3 mm in raindrop size). The agreement between the two spectra in the 2 to 8 m/s velocity range is remarkable. The volume sampled by the radar (approximately 10^4 m^3) is quite sufficient to yield a representative sample of the drops size distribution.

The contribution from air velocity, w , can be objectively determined by calculating the cross correlation, $\rho(\Delta V)$ between predicted and observed spectra as a function of a velocity lag

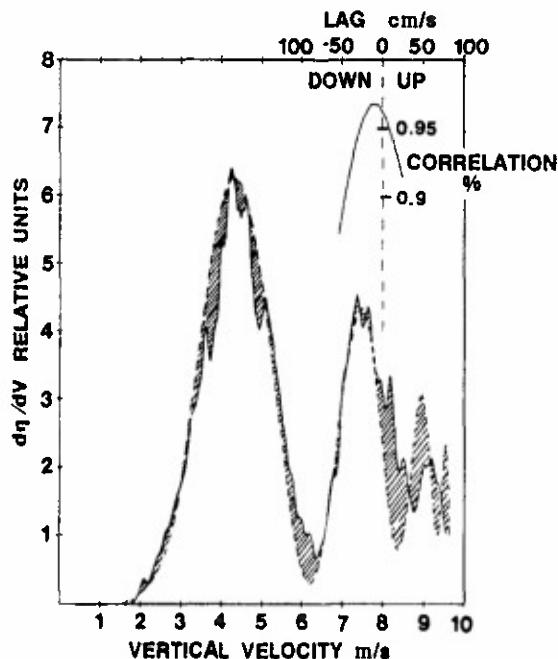


Fig. 2. Radial velocity (Doppler) spectrum observed in a 15 mm/hr rain at vertical incidence together with a predicted spectrum (dashed line) based on Mie backscattering cross section and an exponential drops size distribution with Λ adjusted for best fit. The shaded area shows the difference between the observed and predicted spectrum. The most noticeable feature is the spectral dip at 6.2 m/s. The function at the top of the figure is the cross correlation between the two spectra as a function of a velocity lag. The correlation peak (0.965) is obtained for a very small velocity lag (less than 5 cm/s).

ΔV . The result of such calculations is shown in the upper part of Fig. 2. The cross correlation is maximum (0.965) for a velocity lag slightly less than 5 cm/s (downward). Applying the cross correlation method to a few hundred individual spectra sampled during a 10 minute time interval, indicated that the peak to peak ΔV variation from spectrum to spectrum was approximately ± 30 cm/s with most of the observations showing less than a ± 10 cm/s value. These results are consistent with the observed variations of mean Doppler illustrated by Fig. 4. At the altitude of the observation, the mean Doppler velocity varies by ± 20 cm/s although the radar reflectivity varies by less than 0.1 dB. Such a steadiness of the observed radar reflectivity values indicates that the primary cause for variation of the mean Doppler is variability in air motion. Since the observations presented here were made in stratiform rain conditions, ΔV (attributed to an updraft or a downdraft) is small. However, if these measurements are made in convective rain conditions (i.e. in situations where a rainshaft is associated with a strong downdraft or a microburst) much greater values of w are expected.

In Fig. 2 the spectral dip in the observed spectrum does not quite reach the minimum shown in the predicted spectrum. Spectral averaging required to yield a smooth spectrum could produce this effect, but in our case it is done with a 8 cm/s bandwidth, too small to produce significant spectrum smearing; also amplitude white noise is removed in spectrum processing. The possibility of a significant contribution from radar frequency noise was rejected because backscattering from fixed targets was always observed to be associated with very narrow spectra. Due to the radar narrow beam ($5 \cdot 10^{-3}$ radian)

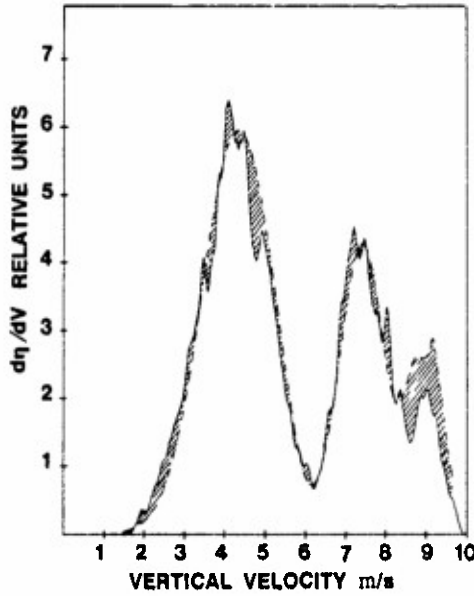


Fig. 3. Same as Fig. 2 but including a 5 cm/s velocity shift and convolving the predicted spectrum with a 20 cm/s standard deviation noise spectrum.

the combined horizontal wind-beamwidth effect on spectrum smearing was also rejected as well as a possible contribution due to multiple scattering. It was felt that the primary contribution to the excess spectral density observed in the spectral dip was the presence of a random component attached to either the velocity or the diameter variables, essentially smearing the V versus D relationship. Departures from sphericity typically observed for large raindrops during their fall could produce a random modulation of the Mie backscattering cross section. However, this effect is not likely to be important for a drop with a diameter less than 2 or 3 mm, so that random fluctuations of raindrop velocity due to air turbulence, or any variations of

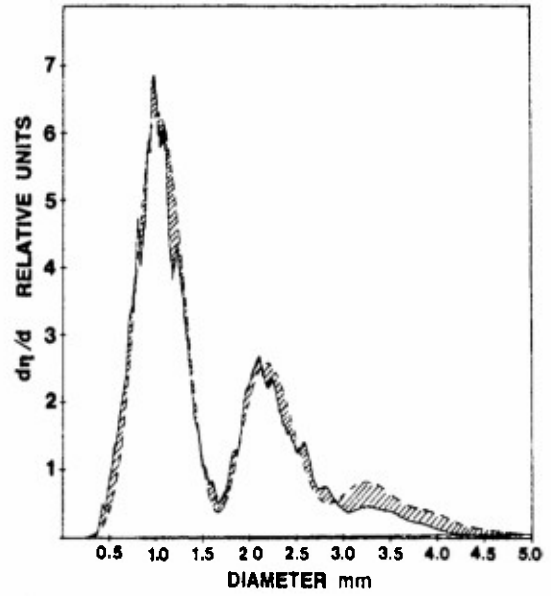


Fig. 5. Spectrum as a function of equal raindrop diameter, D , intervals. Both the observed spectrum and a predicted spectrum (dashed line) based on the Mie function and an exponential dropsize distribution are shown. The shaded area highlights the small difference between the two functions. The agreement is remarkable between $D = 0.5$ to $D = 3$ mm, but for diameters larger than approximately 3mm the observed spectrum falls off more rapidly.

w during the signal dwell time may be a more general cause for spectrum smearing. Such an effect can be reproduced by convolving the original spectrum with a spectrum simulating the random velocity fluctuation and its variance. This method was applied to the predicted spectrum shown in Fig. 2. The results are presented in Fig. 3 and indicate that a convolution with a spectrum having a 30 cm/s bandwidth provides a good

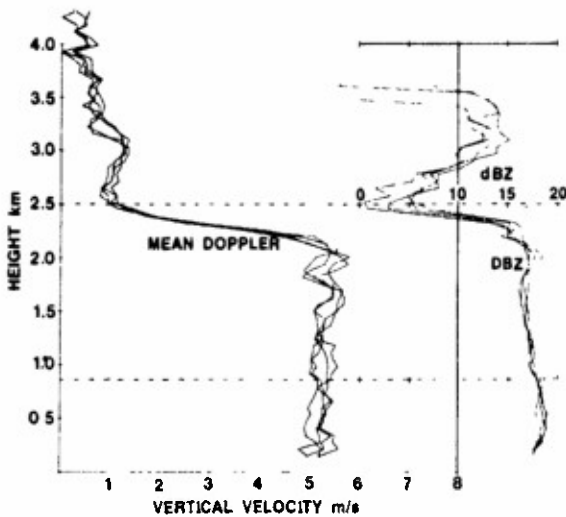


Fig. 4. Vertical profiles of mean Doppler velocity and radar reflectivity in dBZ acquired on 30 November 1987. The sudden velocity increase at an altitude of 2500 meters is due to particle melting. Four profiles, 4 s apart, are shown. The Doppler spectrum measurements were made slightly above the bottom dash line. Note the variability of mean velocity compared to the steadiness of radar reflectivity.

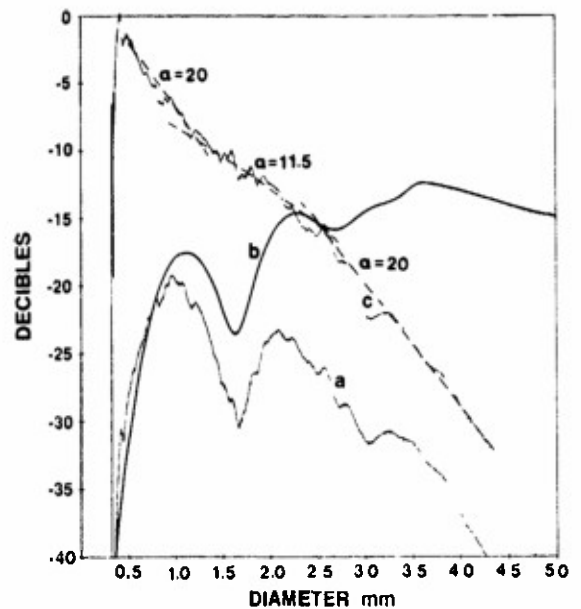


Fig. 6. a) Observed spectrum, b) $\sigma(D)$ function, and c) dropsize distribution $n(D)$ all shown in log scale (decibels). The approximate slope (in cm^{-1}) of $n(D)$ is indicated in several parts of the function.

match between experimental and theoretical results. Inspection of Fig. 3 also indicates that velocity spectrum smearing produces a merging of the closely spaced third and fourth Mie maxima ($D = 3.6$ and 4.6 mm) and yields a much closer similarity between observed and predicted spectra. This is due to the very small value of dV_r/dD for large raindrops. Application of the method to several spectra indicated that the standard deviation needed to match theoretical and experimental data varies from 10 cm/s to 40 cm/s and seems to increase with the number of individual spectra used in the evaluation of an average spectrum. Increasing air motion turbulence would ultimately result in filling the spectral dip at 1.67 mm completely thereby preventing air velocity measurement. This would happen if the random velocity fluctuation reaches a peak-to-peak value of ± 5 m/s (standard deviation greater than approximately 2 m/s).

After w is estimated using the above correlation method and the air turbulence correction introduced, we can calculate the spectrum, $S(D) = d\eta/dD$, now expressed as a function of equal diameter intervals. An example of such results is shown in Fig. 5 where the observed spectrum is again shown with a predicted spectrum based on the Mie backscattering function and a linear exponential drop size distribution with the slope adjusted for best fit. $S(D) = n(D)\sigma(D)$ so that $n(D)$ can be readily computed. An example of the results is shown in Fig. 6 where $S(D)$, $\sigma(D)$, and the calculated $n(D)$ function are shown using a logarithmic scale for better perception. Incidentally, we found that the smoothness of the calculated $n(D)$ function in the vicinity of the spectral dip is very sensitive to a correct choice of both ΔV and the spectral variance added to the predicted spectrum. Fig. 6 shows that there is a large deficiency of raindrops below $D = 0.5$ mm. Above $D = 0.5$ mm the $n(D)$ function exhibits a near exponential decay but the local exponential slope (in cm^{-1}) varies markedly from 20 ($D = 0.5$ to 1.5 mm), to 12 ($D = 1.5$ to 2.5 mm), to 21 ($D = 2$ to 4 mm), and increases more rapidly afterwards.

CONCLUSION

We intend to apply the method to measurements of air vertical velocity, and possibly air turbulence and drop size distribution in rainshafts produced by convective storms. The method would also be very useful in providing vertical profiles of drop size distribution and air vertical velocity in precipitation regions observed by an S-band radar in an effort to improve our knowledge of the radar reflectivity-rain intensity relationship. We also intend to extend our measurements to the spectrum of the cross polarized component, a method which would bring an insight of large particle shape distortions. So far we have

limited our observations to liquid raindrops and it is unknown at this point if the method is applicable to identification of graupel or hailstones and their sizes. However, we will attempt to obtain Doppler spectra in these conditions.

ACKNOWLEDGEMENTS

The millimeter wave Doppler radar was developed under the Army Research Office Contract DAAL03-86-K-0145. Many thanks to Dr. Walter Flood from ARO who provided us the continuing support without which these research achievements could not have been possible.

The data were acquired during a field project sponsored by the Air Force Cambridge Laboratories (Contract F19628-87-C106) monitored by Drs. K. Glover and J. Metcalf whose support for the field project is also deeply appreciated. Thanks to Drs. P.T. Willis and R.J. Pasch for many valuable discussions. Dr. Pasch also had a key role in the development of the data processing programs.

REFERENCES

- Battan, L.J., Some observations of vertical velocities and precipitation sizes in a thunderstorm. *J. of Appl. Meteor.*, **3**, 415-420, 1964.
- Beard, K.V., Terminal velocity and shape of cloud and precipitation drops aloft. *J. Atmos. Sci.*, **33**, 851-864, 1976.
- Foot, G.B. and P.S. duToit, Terminal velocity of raindrops aloft. *J. Appl. Meteor.*, **8**, 249-253, 1969.
- Gunn, R., and G.D. Kinzer, The terminal velocity of fall for water drops in stagnant air. *J. Meteor.*, **6**, 243-248, 1949.
- Lhermitte, R., A 94 GHz radar for cloud observations. *J. Atmos. Ocean. Tech.*, **4**, 36-48, 1987.
- Marshall, J.S. and W.MCK Palmer, The distribution of raindrops with size. *J. Meteor.*, **5**, 165-166, 1948.
- Mie, G., Beitrage zur optik truer medien, speziell kolloidaler metallosingen. *Ann. Phys.*, **25**, 377-445, 1908.
- Rogers, R.R., An Extension of the Z-R relation for Doppler radar. *Eleventh Weather Radar Confer. Amer. Meteor. Soc.*, Boston, Mass., 1964.

Roger M. Lhermitte, Roenstiel School of Marine and Atmospheric Sciences, University of Miami, Miami, Florida 33149.

(Received April 20, 1988;
accepted July 25, 1988.)

Cloud and Precipitation Remote Sensing at 94 GHz

ROGER M. LHERMITTE

Abstract—The paper is concerned with the use of short millimeter-wave Doppler radars for the observation of clouds and precipitation. Attenuation and scattering (including Mie backscattering by raindrops) of these short wavelengths radiation by hydrometers is discussed as well as the sensitivity of such radars for the observation of clouds.

Results of observations indicate that the internal circulation of fair weather cumulus is effectively observed.

I. BACKGROUND

METEOROLOGICAL radars operate typically at centimeter wavelengths primarily to avoid problems in the interpretation of echo signal intensity in terms of radar reflectivity, arising from the significant attenuation of shorter wavelength radiation propagating through precipitation regions. However, when it became evident that clouds were not observed by centimeter-wave radars, the search for an increased radar sensitivity was directed toward the use of shorter wavelengths for which an increase of cloud radar reflectivity due to Rayleigh scattering (see (3)) is expected, and the use of millimeter-wave radars was recommended.

Wavelength selection for a radar operated in the earth's atmosphere is restricted to spectral regions where absorption by atmospheric gases is low. The millimeter-wave absorption spectrum is shown in Fig. 1. Outside of the water vapor line at 23 GHz, the spectrum is dominated by three strong absorption regions: (a) the 60-GHz complex of rotational O_2 lines, (b) another O_2 line at 118 GHz, and (c) a strong water vapor line at 183 GHz. The spectral windows where local minima of atmospheric absorption occur are centered on 35, 100, 150, and 210–290 GHz. The residual absorption in all the windows is primarily due to the skirts of water vapor lines and increases systematically with the window frequency. At low humidity (less than 1 g/m^3 , for instance), the one-way absorption in all the windows is below 0.1 dB/km, but for strong humidity (i.e., 25 g/m^3) it increases to 0.7, 2.5, 6, and 15 dB/km, at 35, 100, 150, and 210 GHz, respectively.

Although there were attempts to observe clouds at a 1.2-cm wavelength in the early days of radar meteorology, the first systematic millimeter-wave radar observations of clouds were done in the 35-GHz window (i.e., [10]). The radar was designed as a cloud monitoring instrument and

was used for several years primarily as a qualitative indicator of cloud cover (ceilometer). There was no attempt to measure cloud radar reflectivity at these times and it is regrettable that the radars were not properly calibrated. Measuring cloud echo intensity would have produced an extensive documentation on cloud radar reflectivity at 35 GHz, especially for cirrus clouds, which were well detected by the radar.

More recently, 35-GHz radars were again considered for cloud observations and some of the available equipments converted into Doppler radars [12], [9], [1]. These radars are equipped with the same magnetron that was developed earlier, now used in conjunction with a Stalco-Coho technique for measurement of the echo phase containing the Doppler information.

The expectation that a shorter wavelength would increase cloud radar reflectivity further was an incentive for proposing the use of frequencies beyond 35 GHz. The recent development, at 94 GHz, of a receiver technology comparable to that available for centimeter-wave radar design and the availability of long-life high-power transmitter tubes (extended interaction oscillator, EIO) presented the opportunity to design and assemble a cloud observation radar working at a wavelength shorter than the previous 35-GHz band limit [6]. It was decided to equip the radar with a modern signal processing system so that accurate quantitative measurements of radar reflectivity, mean Doppler velocity, and velocity spectrum variance could be obtained. Primarily due to the use of the EIO and a well-designed low-noise local oscillator (phase lock oscillator), the radar demonstrated excellent Doppler performance [3]. Some of the results of cloud observations performed with the radar were published previously [3], [4]. This paper summarizes the radar characteristics and performance as a cloud observing instrument, discusses signal attenuation by water vapor and hydrometers at 94 GHz, and presents some of the results on cloud and precipitation observations.

II. RADAR WAVELENGTH AND CLOUD OBSERVATION CAPABILITY

Assuming that the radar beam is completely filled by the distributed target (cloud), the performance of a meteorological radar can be derived from the following radar equation:

$$\begin{aligned}
 10 \log \eta &= 10 \log P_r - 10 \log P_t \\
 &- 10 \log (h) - 10 \log (A_r) \\
 &+ 10 \log (2\pi R^2) + \beta \quad (1)
 \end{aligned}$$

Manuscript received October 5, 1987; revised January 26, 1988. This work was supported by the Army Research Office under Contract DAAG29-84-0145.

The author is with the Rosenstiel School of Marine and Atmospheric Science, University of Miami, Miami, FL 33149.

IEEE Log Number 8820744

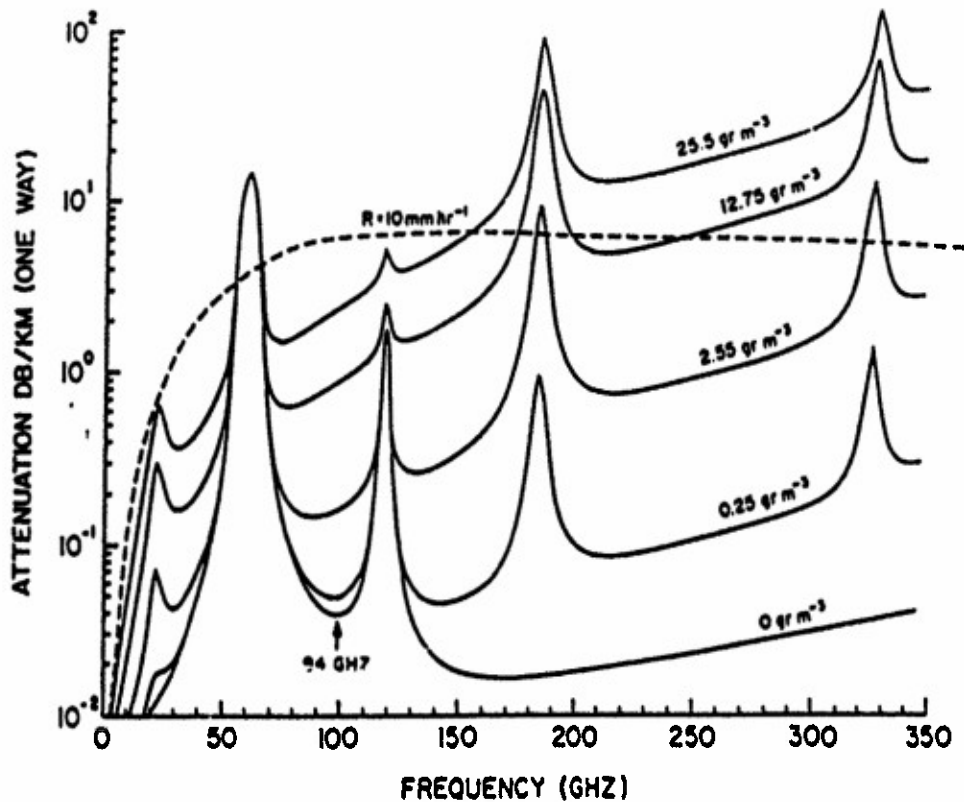


Fig. 1. Atmospheric gases absorption spectrum at the ground in various humidity conditions indicated by the specific humidity values. Absorption for a 10 mm h^{-1} rain is also indicated.

where η is the radar reflectivity in negative reciprocal centimeters. P_r and P_t , respectively, are the received power and the transmitter peak power in watts. h is the radial dimension of the pulse volume. A_e is the antenna effective area, and R is the range of the target. β is a corrective term that includes transmitter antenna efficiency ($\sim 2 \text{ dB}$) and two-way signal attenuation between radar and target.

If the cloud particles are so small that even the shortest radar wavelength is associated with Rayleigh scattering (cloud particle diameter smaller than approximately one-fourth of the radar wavelength), the radar reflectivity factor, $Z = \int N(D) D^6 dD$ (N in particles per cubic meter and D in millimeters); is given by $Z = (\eta \lambda^4) / (\pi^3 |K|^2)$ where $|K|^2$ is a scattering parameter discussed below. With the more familiar $\text{dBZ} = 10 \log Z$ units

$$\text{dBZ} = 10 \log \eta + 95.14 + 40 \log \lambda - 10 \log |K|^2 \quad (2)$$

or

$$\begin{aligned} \text{dBZ} = & 10 \log P_r + 40 \log \lambda - 10 \log P_t \\ & - 10 \log h - 10 \log A_e + 10 \log (2\pi R^2) \\ & + 10 \log |K|^2 + 95.14. \end{aligned} \quad (3)$$

The term containing λ shows the drastic influence of the radar wavelength on radar sensitivity, which is a strong incentive for the choice of a very short wavelength for cloud detection. When examining the contribution to ra-

dar sensitivity from the terms in (3), it should be remembered that echo intensity measurements are usually performed using a signal integrator so that the smallest signal the receiver can detect is a function of the number of samples used in performing the integration. More specifically, integration of a radar signal P_r , which is performed on receiver signal samples digitized at the radar repetition rate at adjacent range gates, has two effects. Firstly, it reduces the standard deviation of the fluctuating mean estimate to $\bar{P}_r / (N_s)^{1/2}$, where N_s is the equivalent number of independent samples (smaller than the actual number N of samples depending on sample to sample correlation). Secondly, it reduces the effective receiver noise level P_n to $P_n / (N)^{1/2}$, where N is now the actual number of samples integrated as they are statistically independent from pulse to pulse. Therefore, for a given signal dwell time, the radar sensitivity increases not only with the pulse width (or pulse volume radial dimension, the term containing h in the equation above), but also with the radar pulse repetition rate. Radar sensitivity for distributed targets (i.e., clouds) is thus a function of the transmitter average power, not peak power.

We are now equipped to examine the relative merit (compared to a typical S-band radar) for cloud observation of typical radars operating at wavelengths ranging from S-band (3 GHz) to the present technological limit of approximately 220 GHz. Table I is based on average characteristics of meteorological radars actually in use and shows the wavelength dependence of the transmitter av-

TABLE I

Wave length cm	Transmitter Average power dB(W)	Antenna size dB(m)	Rec. NF figure (dB)	λ^{-4} gain dB	Beam width degree	Far field km	Total dB
10.0	0(500)	0(10.0)	0(1)	0	0.7	2.00	0
5.6	-2(300)	-10(3.6)	-1(2)	+10	1.0	0.23	-3
3.2	-3(250)	-10(3.0)	-2(3)	+20	0.7	0.28	+5
0.85	-13(25)	-14(2.0)	-4(5)	+42	0.3	0.47	+11
0.32	-20(5)	-20(1.0)	-4(5)	+60	0.2	0.31	+16
0.14	-30(0.5)	-34(0.2)	-7(8)	+73	0.3	0.03	+2

verage power, antenna size, receiver noise level, $1/\lambda^4$ Rayleigh scattering gain, and the overall merit figure of the radar for cloud detection. The radar antenna beamwidth and the far field factor $R = D^2/\lambda$ are also indicated.

Table I, covering radar wavelengths from 10 to 0.14 cm, shows that, despite large variations of some of the individual terms, there is only a relatively small change of the overall radar sensitivity for cloud observation. Note that the above data relates to typical meteorological radar characteristics that do not necessarily represent state-of-the-art radar development.

Besides the far field condition, which, for antennae producing the same beamwidth, is more favorable at shorter wavelengths, the most important consideration for close range detection of weak atmospheric targets is not only the receiver noise level, but also ground echoes leaking through the antenna sidelobes. This is especially true for high-power long-wavelength radars. Assuming the same sidelobe structure for all antennae regardless of the wavelength, the effect of ground echo interference in the measurement of the weak backscattering produced by a small cloud at close range can be characterized by the contrast between returns from the ground and from clouds. Ground echoes are caused by a variety of large size targets such as buildings, trees, terrain, etc. The variation as a function of radar wavelength of ground clutter radar cross section per unit area σ^0 is not well known and depends on the targets, but it seems to increase only very slowly with a decrease of the wavelength. On the other hand, cloud echo intensity increases proportionally to $1/\lambda^4$, or a dramatic increase of 60 dB from 10- to 0.32-cm wavelength. Therefore, even with a possible 10-dB increase of σ^0 with the shorter wavelength, the ground clutter-cloud return contrast will improve by at least 50 dB from a 10- to 0.3-cm wavelength. It is our experience that, even surrounded with buildings, a 94-GHz radar, providing a theoretical 15-dB (no-clutter) cloud detection improvement over an S-band radar, does not show any measurable (less than 20 dB below receiver noise) ground clutter signal at short

ranges (200 m) for elevation angles above approximately 5° . Therefore, a millimeter-wave radar operated in a vertically pointing mode (or slightly off vertical if three-dimensional scanning is required) is an attractive solution for the observation of low-altitude low-reflectivity clouds such as fair weather cumuli.

The 94-GHz radar discussed here provides a Rayleigh scattering gain of 17 dB over a 35-GHz radar and has the following main characteristics: peak power 1.2 kW (10 kW), maximum average power 5 W (25 W), antenna size 90 cm (180 cm), receiver double side-band noise figure 6 dB (5 dB). The numbers quoted within parentheses are feasible improvements of the radar characteristics that are not implemented at the present time. The radar described in [1] operates at 35 GHz and has the following characteristics: average power 25 W, antenna size 180 cm. A receiver noise power of -85 dBm is quoted by Hobbs but with the indicated receiver bandwidth and an up-to-date mixer, the receiver noise should be down to -95 dBm (6-dB DSB noise figure).

Assuming that such a receiver noise improvement is realized in the Hobbs' radar, the 94-GHz radar exhibits a dB sensitivity gain on cloud detection with a 3-ft dish, and 11 dB with a 6-ft dish. With an average power increase to 25 W, the sensitivity gain is 17 dB. Small fair weather cumuli are at the threshold of detection (dBZ -50) and even a relatively small improvement of the radar sensitivity may make a significant difference in their detectability.

The 94-GHz radar has a much smaller size, is operated at low power (a few hundred watts of power supply) and does not require waveguide pressurization. The 94-GHz radar also uses a gridded extended interaction oscillator (EIO), which exhibits much less intrapulse FM or phase noise [6] than the magnetron used in the 35-GHz radar. This is confirmed by observations of fixed target signal phase coherence and also tests of mean Doppler stability and spectral variance on cloud echoes [3] that indicate that the radar phase noise contribution to the measurement of Doppler spectrum moments is negligible.

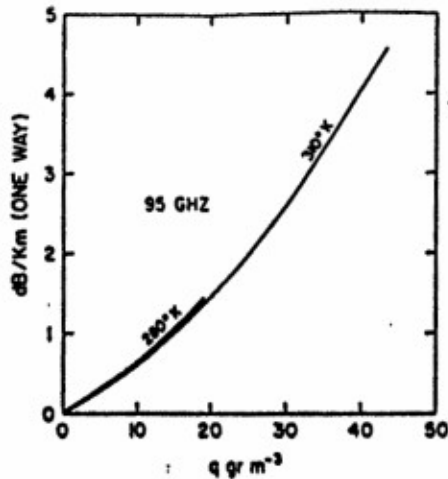


Fig. 2. Atmospheric attenuation at 94 GHz as a function of specific humidity in grams times cubic meters, at ground pressure and for two temperatures, 280 and 310°K.

III. ABSORPTION OF 94-GHZ RADIATION BY ATMOSPHERIC GASES AND HYDROMETEORS

The clear air residual atmospheric absorption in the 94-GHz window is due to the skirts of the O₂ and H₂O lines and depends on altitude (pressure broadening) and specific humidity. There is a small variation with temperature. The absorption varies from approximately 0.4 dB/km for a low 0.25 g/m³ humidity to approximately 2 dB/km for a high 25 g/m³ humidity (see Fig. 2).

Absorption is a line integral of the absorption coefficients evaluated from the radar to the target. Since, in clear air, water vapor is the dominant absorption agent, the maximum zenith absorption (i.e., to the top of the atmosphere) for a vertically pointing beam is a function of humidity conditions and can be derived from the vertically integrated water vapor that is often characterized as the precipitable water. The 94-GHz absorption coefficients based on data by Liebe [8] and Shimabukuro and Epstein [13] are shown in Fig. 3. The one-way zenith absorption varies from approximately 0.5 dB for a dry atmosphere (0.6-cm precipitable water) to more than 3 dB for a very humid one (5-cm precipitable water). It increases by 3 percent for a radar beam 15° off vertical, 15 percent for 30°, and doubles for 60°. Although the vertically pointing beam mode yields the least absorption, off vertical scanning up to 30° offering a beam scanning capability can be tolerated even in the case of a humid atmosphere.

Attenuation of 94-GHz radiation by clouds and precipitation is caused by: 1) absorption of the radiative energy being transferred into heating of the particles; 2) scattering of radiative energy by the hydrometeors. The absorption cross section Q_a and the scattering cross section Q_s of a sphere (cloud droplet) much smaller than the radiation wavelength, (Rayleigh absorption) is given by

$$Q_a = \pi^2 D^3 \text{Im}(-K)/\lambda \quad (3b)$$

$$Q_s = 2\pi^2 D^6 |K|^2 / 3\lambda^4 \quad (4)$$

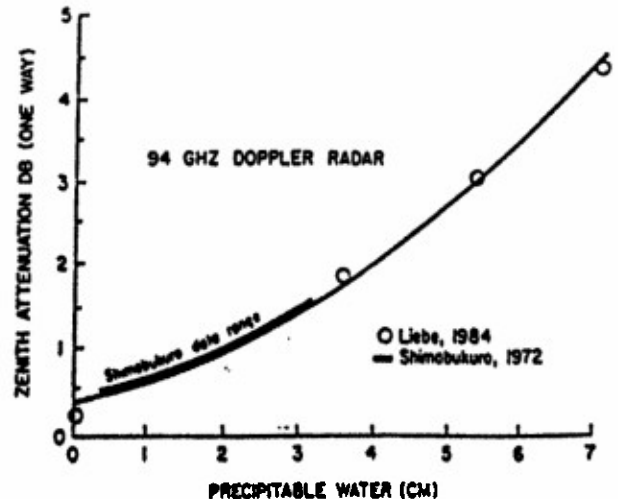


Fig. 3. One-way zenith absorption as a function of precipitable water. The solid line is the model proposed by Shimabukuro as a least squares fit of his data. The circles are the values proposed by Liebe on the basis of his experiments.

where $K = (m^2 - 1)/(m^2 + 2)$, and $m = n' + in''$ is the complex index of refraction of water (or ice). $\text{Im}(-K)$ is the imaginary part of K . The attenuation cross section is $Q_t = Q_a + Q_s$. For a cloud of particles, the absorption, scattering, and extinction coefficients (in decibels per kilometer), α_a , α_s , α_t , respectively, are expressed by

$$\alpha_a = 0.434 \sum Q_a \quad (5)$$

(similarly for α_s , α_t with the summation extending to all particles present in a cubic meter of air). In the case of Rayleigh absorption (droplets much smaller than the radar wavelength) α_a in decibels per kilometer is given by: $\alpha_a = 8.18M \text{Im}(-K)/\lambda$ where M is the cloud liquid water in grams per cubic meter.

At 94 GHz, the complex index of refraction of liquid water must be interpolated between actual measurements at $\lambda = 1$ mm and $\lambda = 5$ mm, using the Debye equations [11] and is seen to vary with temperature. Table II shows, at 94 GHz, the real and imaginary parts of m , the absorption index $\text{Im}(-K)$, the absorption coefficients, and the scattering index $|K|^2$.

The α_a values above are presented graphically in Fig. 4 where α_a is seen to vary almost linearly with temperature. The scattering cross section Q_s is negligible for Rayleigh absorbers.

In the case of larger size particles for which Rayleigh scattering is not applicable, the computation of α for a given cloud or precipitation must be based on a knowledge of particle size distribution. To overcome this requirement and still provide an insight of the importance of 94-GHz signal absorption by precipitation, the contribution to α due to 1 g/m³ of water divided into drops of the same diameter D is calculated as a function of that diameter.

The α_s and α_t coefficients computed in these conditions using Mie tables are shown in Fig. 5 as a function of D .

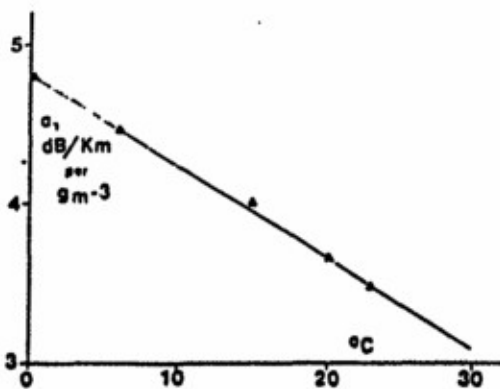


Fig. 4. Absorption coefficient at 94 GHz, α_a , as a function of water temperature, for liquid droplets in the Rayleigh region. α_a is normalized to a $1\text{-}g\text{-}m^{-3}$ cloud water content.

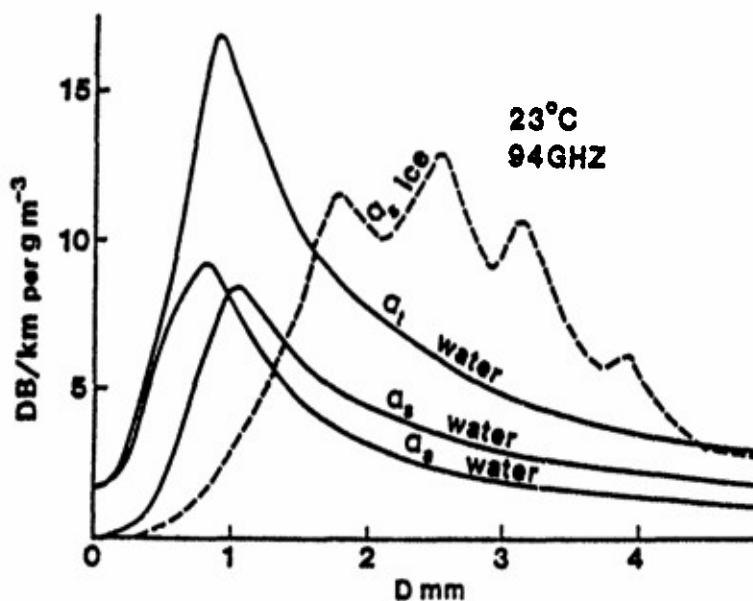


Fig. 5. Absorption α_a , scattering α_s , and attenuation α_t , coefficients at 94 GHz for a monodisperse distribution $1\text{-}g\text{-}m^{-3}$ water content cloud (23°C) as a function of particle size. α_s is also shown for a cloud composed of spherical ice particles.

TABLE II
INDEX OF REFRACTION OF LIQUID WATER ABSORPTION AND SCATTERING TERMS AT 94 GHz

Temperature	n'	n''	$\text{Im}(-\kappa)$	α_a dB/km/($g\ m^{-3}$)	$ \kappa ^2$
0°C	2.84	1.48	0.1938	4.80	0.711
15°C	3.21	1.79	0.1614	4.0	0.787
20°C	3.41	2.02	0.1470	3.64	0.828
23°C	3.05	2.05	0.1402	3.47	0.832

for a liquid water content of $1\text{ }g\text{/}m^3$. α_a , which exhibits a constant value of 3.47 dB/km (temperature 23°C) in the Rayleigh region, increases to a maximum of 9 dB/km for a particle diameter of approximately 1 mm, and decreases to a value smaller than that observed in the Ray-

leigh region for a particle size greater than 3 mm. The contribution to a α_s , which is negligible in the Rayleigh region, increases to a maximum of approximately 8 dB/km for $D = 1\text{ mm}$, and decreases to approximately 3.5 dB/km for $D = 3.5\text{ mm}$.

In the case of ice particles we have: $m = 1.878 + i4.76 \cdot 10^{-4}$ (0°C) so that $\text{Im}(-K) \sim 2 \cdot 10^{-4}$ and $\alpha_m \sim 6 \cdot 10^{-3}$ dB/km. Although it may be concluded that, even at 94 GHz, signal attenuation by an ice cloud is negligible, this is only true for Rayleigh scattering, and perhaps for Mie scattering if we consider only attenuation caused by absorption. At 94 GHz, 60–70 μm ice spheres produce a scattering contribution to attenuation equal to that due to absorption. For larger sizes, the scattering contribution becomes rapidly overwhelming, reaching more than 10 dB/km for particle sizes of $D = 1\text{--}2$ mm. Note that, except for solid hailstones, the assumption of spherical particles is not realistic and should be replaced by the complex structure of an ice crystal or snowflake for which the analytical Mie solution is inapplicable.

IV. CLOUD AND PRECIPITATION RADAR REFLECTIVITY AT 94 GHz

In the Rayleigh region, the backscattering cross section of a sphere is $\sigma = \pi^3 D^6 |K|^2 / \lambda^4$, so that cloud radar reflectivity η is

$$\eta = (\pi^3 |K|^2 / \lambda^4) \int N(D) dD. \quad (6)$$

η is in reciprocal centimeters and D and λ are in centimeters. $|K|^2$ is shown in Table II and is seen to increase only slightly with temperature.

Table III shows, at 94 GHz and 23° temperature, the radar reflectivity of 1 g/m^3 liquid water, divided in droplets of the same diameter D , as a function of the droplet diameter D .

For non-Rayleigh scatterers (drops having a diameter larger than 0.5 mm at 94 GHz), the computation of radar reflectivity must be performed using the Mie backscattering cross section that is shown in Fig. 6. The radar reflectivity is given by an integral over all particle sizes, thereby involving the drop size distribution. It was shown [3] that, assuming a Marshall-Palmer [1948] drop size distribution, the maximum radar reflectivity encountered in heavy rain will not exceed 30 dBZ. However, in order to provide an insight into the influence of particle size on radar reflectivity at 94 GHz, the contribution to radar reflectivity arising from 1 g/m^3 of water divided into droplets of a given diameter D is shown in Fig. 7 as a function of D for both water and ice. A maximum reflectivity is reached if the same liquid water is divided into 1-mm drops. Larger sizes are associated with less reflectivity; however, there are deep oscillations of the function in the precipitation particle size range. Comparing the scattering functions for ice and water indicates that, for Rayleigh scattering, there is an increase of reflectivity of approximately 6 dB if a particle changes from ice to water during melting. However, this effect is reversed for particles of larger size for which Mie scattering applies. Indeed, at 94 GHz, backscattering by ice spheres having a diameter greater than 2 mm is much stronger than that produced by water spheres of the same size.

The presence of deep Mie scattering oscillations within

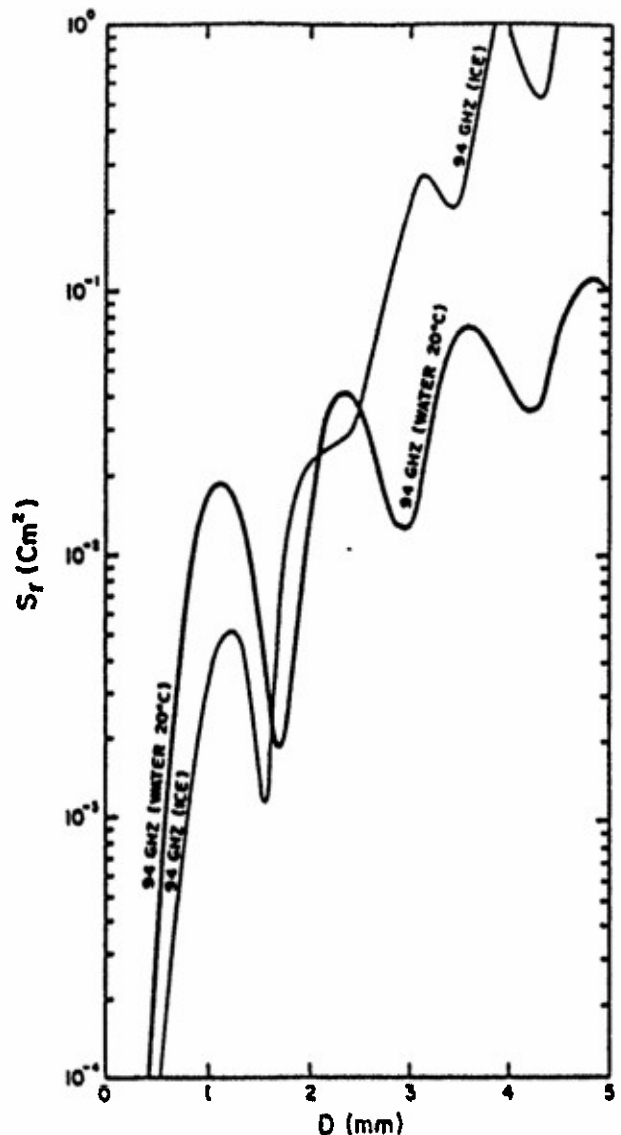


Fig. 6. Backscattering cross section of water and ice spheres at 94 GHz.

TABLE III

D	$\eta(\text{cm}^{-1})$	dBZ
1 μ	$4.6 \cdot 10^{-14}$	-57
10 μ	$4.6 \cdot 10^{-11}$	-27
100 μ	$4.6 \cdot 10^{-8}$	+03

the raindrop size range may provide an opportunity to remotely identify raindrop size. This is realized, for instance, if observation of the Doppler spectrum (density distribution of reflectivity $d\eta/dV$ as a function of radial speed V) is made in rain conditions at vertical incidence. To illustrate this method, Fig. 8 shows a theoretical evaluation of a Doppler spectrum observed at vertical incidence in a 1 mm/h rainfall assuming a Marshall-Palmer

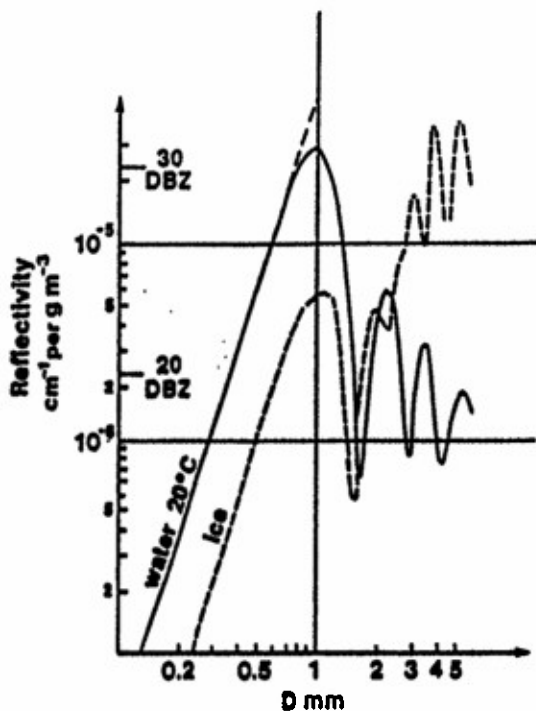


Fig. 7. Radar reflectivity contribution based on Mie scattering functions by particles of diameter D , per grams times cubic meters of water content, as a function of D . The same calculations for ice spheres are also indicated.

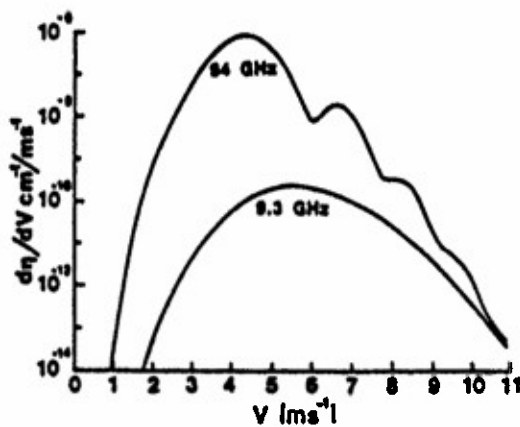


Fig. 8. Doppler spectrum at vertical incidence for a 1-mm/h rainfall assuming a Marshall-Palmer drop size distribution, calculated at 94- and 9.3-GHz radar frequency.

drop size distribution. The oscillations of the Mie scattering functions are clearly visible. The Doppler spectrum observed in the same rainfall but at 9 GHz is also shown for comparison. Fig. 9 shows the ratio r between the two (94 and 9 GHz) spectra. This ratio r is independent of the drop size distribution and only a function of drop size and, if air vertical velocity is neglected, a function of the raindrop vertical velocities or Doppler frequency shifts at vertical incidence. One sees that in the Rayleigh region, r is 40 dB, which reflects the λ^{-4} relationship, decreases to 15 dB for $D = 1$ mm, and then oscillates with well defined maxima at $D = 2.2, 3.5,$ and 4.75 mm; r is also shown for ice and indicates that the rolloff of the function

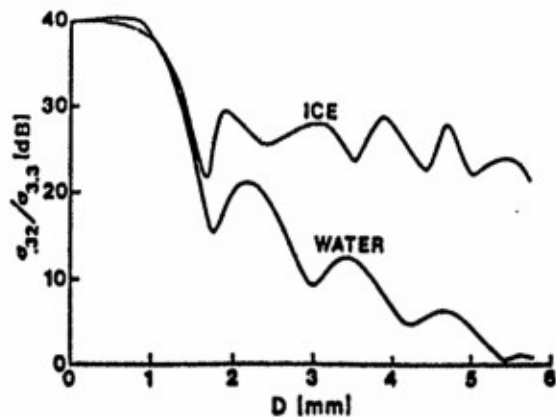


Fig. 9. Ratio between Doppler spectra at 94- and 9.3-GHz wavelength as a function of particle diameter. This ratio is effectively represented by the ratio between radar cross sections at the two wavelengths. The results are also shown for ice spheres.

with increasing particle diameter is limited to less than 15 dB instead of 40 dB in the water case. This may offer a means to differentiate between raindrops and hailstones.

V. SIGNAL PROCESSOR AND RADAR PERFORMANCE

The radar is equipped with an autocovariance processor (pulse pair processor) and a signal integrator that were both described earlier (2). The two terms of the autocovariance function and the signal complex square (0 lag correlation term) as well as the integration of a log receiver signal are evaluated in real time with a fast digital hardware processing unit and recorded on magnetic tape. The computation of mean Doppler and spectral width, which is performed by a microcomputer from the recorded data, was discussed previously (2). This method allows flexibility for the computation of spectral moments, particularly useful for the calibration of the spectrum width for which receiver noise has to be estimated (7). The processor produces pulse pair data continuously evaluated at 400-ns range intervals. Most of the data recorded so far were obtained with a 10-kHz PRF (± 8 m/s unambiguous Doppler velocity range), a 0.4- μ s pulse width providing a range resolution of 60 m, and 32 000 samples (3.2-s dwell time) used in the evaluation of the autocovariance and signal intensity terms. In these conditions, mean Doppler, spectral width, and mean signal intensity can be extracted from signals 22 dB below the receiver noise level (3).

The radar has been operated with a transmitter peak power of 1.2 kw (pulse width 0.4 μ s), and a 90-cm diameter antenna with a one-way efficiency factor estimated to be 2 dB. In these conditions, the minimum radar reflectivity that can be detected by the radar at a 1-km range is given by inserting these values in (1). We have

$$10 \log \eta = P_r \text{ (dBm)} - 18 + 20 \log R \quad (7)$$

or using the more familiar dBZ with $10 \log \eta = \text{dBZ} - 76.2$ at 94 GHz, we have

$$\text{dBZ} = P_r \text{ (dBm)} + 57.8 + 20 \log R. \quad (8)$$

The above values only apply to Rayleigh scattering. For larger particles, we must define an equivalent Z_e , i.e., the radar reflectivity factor of Rayleigh-scattering raindrops required to produce an echo intensity equal to that observed.

In the radar receiver, the signal at the output of a logarithmic amplifier is integrated using 32 000 samples so that its level is determined with approximately 0.01-dB precision. The method for extracting the signal power P_s is based on measuring the ratio, $\alpha = (P_s + P_n)/P_n$ (P_n is the noise power), and then computing $P_s/P_n = 10^{\alpha} - 1$. Assuming that the noise at the output of the receiver is entirely due to the 94-GHz receiver input noise and estimating this noise from receiver calibration using solar radiation received by the antenna [3] provides a technique for the measurement of signal power. Using 32 000 samples in the integration yields a theoretical noise reduction of 22 dB, which is confirmed by our tests. The receiver noise power is estimated to be -93 dBm (15-MHz receiver bandwidth, 6-dB DSB noise figure) so that the minimum detectable signal in these conditions is about -115 dBm. If we report these data in (8), the minimum dBZ value that the radar can detect at a 2-km range (typical boundary layer cloud top) is ~ -50 dBZ. Table III indicates that -50 dBZ is the radar reflectivity of a cloud with 10 mg of liquid water and a particle size of 10 μm , which is less than the typical conditions encountered in a fair weather cumulus.

VI. MODE OF OPERATION AND RESULTS OF CLOUD OBSERVATION

One of the project objectives was to observe the vertical air velocity w , which, in the case of very small droplets having negligible terminal velocity, is directly measured using a fixed vertically pointing radar beam. This mode of operation yields a vertical cross section of the observed clouds where time can be replaced by a space coordinate if it is assumed that the clouds are at a nearly steady state and translating at a fixed speed. This is acceptable for stratiform clouds or precipitation conditions. In the case of an isolated cloud such as a fair weather cumulus, the method can still yield very useful data but can be advantageously replaced by a two-dimensional cloud scanning methodology. The radar beam is now scanned slightly off vertical (i.e., an elevation angle of $90 \pm 15^\circ$ that does not appreciably change the signal attenuation conditions) and that, combined with the cloud motion, yields an effective three-dimensional probing of the cloud. The only problem is the contamination of vertical velocity by horizontal velocity, which occurs for nonvertical beam angles. However, if the technique is applied to the observation of a fair weather cumulus moving in a well-defined direction, the scanning can be done in a direction perpendicular to the cloud motion so that any contribution to radial velocity by the cloud horizontal velocity is minimized.

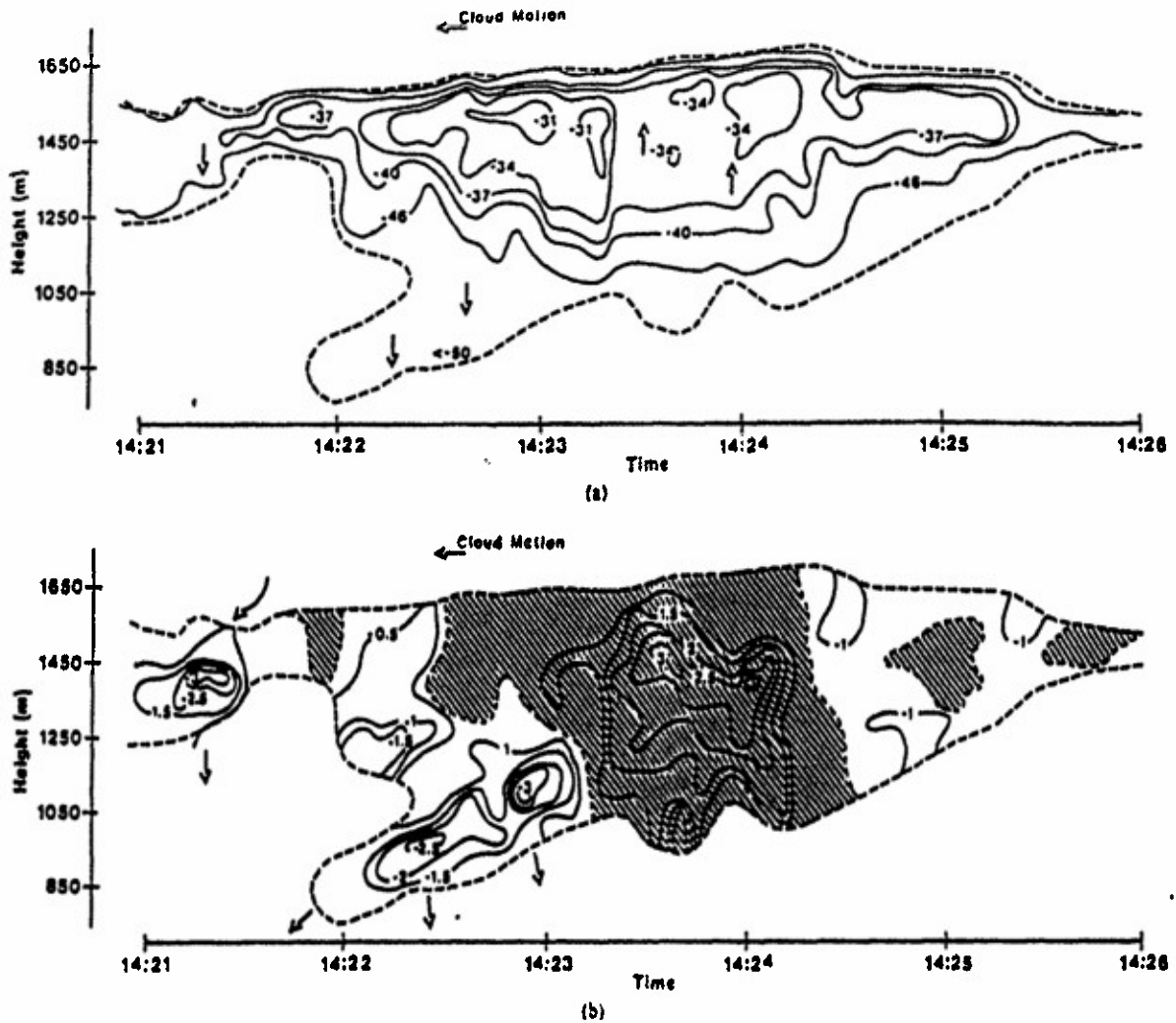
Such three-dimensional scanning is now planned but all the 94-GHz radar observations of clouds in the past were

performed using a fixed vertically pointing radar. This methodology is appropriate for the observation of cloud layers such as stratus, stratocumulus, cirrus, and also stratiform precipitation. Incidentally, the experience acquired using the radar indicates that data in stratified, slightly precipitating, nimbostratus clouds are obtained up to the cloud top at 8 km. High-altitude (12–14 km) cirrus are always detected even if barely visible with the naked eye.

In the case of isolated clouds such as fair weather cumulus, there is only a small probability for the cloud to pass overhead with the radar intersecting the cloud center so that a representative vertical cross section of both radar reflectivity and vertical velocity could be obtained. During a two-month cloud observation campaign in the 1986–1987 winter in Florida, we were fortunate to find that, at certain occasions, the radar happened to be underneath a line of cumulus that were systematically moving with the environmental wind and that some of these clouds were passing directly overhead with the radar beam going through the cloud center. These were conditions favorable for acquisition of vertical velocity and radar reflectivity data in a cloud region representative of the cloud circulation. To confirm this favorable aspect of the observations the visual image of the clouds passing directly overhead was recorded by a video camera.

An example of the results is shown in Fig. 10(a) and (b). The data presented are radar reflectivity and vertical velocity in a vertical cross section defined by the translation of the cloud through the radar beam. These data were presented before [4], but they have been reanalyzed to show more detail in both the reflectivity and the radial velocity fields. The radar reflectivity field is shown in Fig. 10(a). The maximum radar reflectivity is -31 dBZ and the minimum detectable reflectivity is -50 dBZ. There is a sharply defined cloud top due to a temperature inversion clearly indicated by the radiosonde data collected that day [4]. The cloud base is not as well defined and exhibits a noticeable variability. The vertical velocity is shown in Fig. 10(b) and reveals the presence of a strong updraft region (updraft maximum velocity 3 m/s) in the cloud center and two significant downdrafts below and toward the cloud's leading edge. Comparing the velocity and the radar reflectivity fields indicates that the bulk of the updraft is just below (and slightly lagging in time) a region of high radar reflectivity, although the downdrafts are always in a region of very low radar reflectivity. The presence of the updraft is associated with local rising of the cloud top (still strongly capped by the temperature inversion lid), and the downdrafts are associated with a local lowering of the cloud bottom that can considerably distort the cloud base.

Fig. 11 shows another type of data collected by the millimeter-wave radar. These observations were made through the melting region of a stratiform cloud previously named "bright band" because of a systematic maximum of echo intensity observed just below the 0° isotherm. The previous bright band observations with cen-



vertical velocity—attributed to the onset of particle melting when they fall through the melting zone—which was previously observed by centimeter-wave radars. There is also, on the top of the melting zone, the same 6–7 dB increase of radar reflectivity that was observed by centimeter-wave radars and is attributed to the change of index of refraction from ice to water. However, the 94-GHz observations show that, although the particles' acceleration in the melting zone is comparable to that observed with centimeter-wave radars, it is no longer associated with a decrease of the reflectivity observed when descending through the melting zone. The decrease of radar reflectivity below the maximum clearly observed with centimeter-wave radars was primarily attributed to the decrease of particle concentration—and thus radar reflectivity—due to the systematic acceleration of the particles through the melting zone end, to a lesser degree, to the shrinking of particle size due to melting. Since that reflectivity decrease is not observed by the 94-GHz radar although the particle acceleration through the melting zone is still observed, we must conclude that, when particles shrink during their melting—and thus accelerate—their radar cross section (and therefore the radar reflectivity) increases. The answer to this apparent anomaly may be found in Fig. 6, which shows that, due to the peculiarities of Mie scattering, the radar cross section of a 1.5-mm particle will increase by more than 10 dB if it shrinks to a 1-mm raindrop. The minimum of radar reflectivity above the melting band observed with the millimeter-wave radar, which is sometimes associated with an increase of the particles' vertical velocity, may also be attributed to the same Mie scattering behavior. The data presented in Fig. 11 were all acquired in very light precipitation conditions (1 rime to less than 1 mm/h) with a mean Doppler velocity below the melting region reaching approximately 4 m/s, which is the terminal velocity of a 1-mm raindrop.

VII. CONCLUSION

The 94-GHz Doppler described here is about the shortest wavelength radar that can be assembled for meteorological use. Radar components are available off-the-shelf. The radar is very small, can be easily transported, and has demonstrated excellent Doppler performance. Its capabilities for cloud detection and its portability make it a good cloud physics tool, useful for the study of boundary layer cumuli and clouds in the initial stages of their development.

Because of the deep Mie backscattering oscillations occurring in the raindrop particle size range, the 94-GHz radar is also an attractive choice for drop size distribution measurements based on a multiwavelength methodology, with the 94-GHz radar observations done jointly with an S-band or an X-band radar.

ACKNOWLEDGMENT

This work was monitored by Dr. W. Flood. Dr. Flood's encouragement and constructive review of this work are appreciated. The radar was also installed and operated at Sudbury, Massachusetts in conjunction with an Air Force Geophysical Laboratory Research Program.

REFERENCES

- [1] P. V. Hobbs, N. T. Funk, R. R. Weiss, J. D. Locatelli, and K. R. Biswas, "Evaluation of 35 GHz radar for cloud physics research," *J. Atmos. Ocean. Tech.*, vol. 3, no. 1, pp. 35–48, 1985.
- [2] R. M. Lhermitte, "Observation of clouds and precipitation using a 94 GHz Doppler radar," in *Proc. Ground Based Remote Sensing Techniques for the Troposphere* (Hamburg), sponsored by Stiftung Volkswagenwerk, Aug. 23–25, 1986; see also Supplement, pp. 259–264, Dec. 1986.
- [3] —, "A 94 GHz Doppler radar for cloud observations," *J. Atmos. Ocean. Tech.*, vol. 4, no. 1, pp. 36–48, 1987.
- [4] —, "Small cumuli observed with a 3 mm wavelength Doppler radar," *Geophys. Res. Lett.*, vol. 14, no. 7, pp. 707–710, 1987.
- [5] R. M. Lhermitte and D. Atlas, "Doppler fall speed and particle growth in stratiform precipitation," in *Proc. 10th Wea. Radar Conf., Am. Meteor. Soc.* (Boston), pp. 297–302, 1984.
- [6] R. Lhermitte and C. Frush, "Millimeter-wave radar for meteorological observations," in *Preprint Volume: 22nd Conf. Radar Meteorology, Am. Meteor. Soc.* (Zurich, Switzerland), pp. 228–231, Sept. 10–13, 1984.
- [7] R. M. Lhermitte and R. J. Surahn, "Pulse to pulse coherent Doppler radar signal processing techniques," *J. Atmos. Ocean. Tech.*, vol. 1, no. 4, pp. 293–308, 1984.
- [8] H. J. Liebe, "An updated model for millimeter-wave propagation in moist air," *Radio Sci.*, vol. 20, no. 5, pp. 1069–1089, 1985.
- [9] F. Pasqualucci, B. W. Bartram, R. A. Kropfli, and W. R. Mielinger, "A millimeter wavelength dual-polarization Doppler radar," *J. Climate Appl. Meteor.*, vol. 22, pp. 758–765, 1983.
- [10] P. J. Peirncehi and W. H. Paulsen, "Meteorological significance of vertical density profiles of clouds and precipitation obtained with the AN TPQ-11 radar," in *Proc. 12th Conf. Radar Meteor., Am. Meteor. Soc.*, pp. 467–472, 1966.
- [11] P. S. Ray, "Broadband complex refractive indices of ice and water," *J. Appl. Opt.*, vol. 11, no. 5, pp. 1836–1843, 1972.
- [12] H. Sauvageot, R. Aurou, and B. Campstron, "Long-lasting precipitation cells in stratification clouds," in *Cloud Dynamics*, E. M. Ages and T. Asai, Eds. Boston: D. Reidel, 1982, pp. 73–85.
- [13] F. Shimabukuro and E. Epstein, "Attenuation and emission of the atmosphere at 3.3 mm," *IEEE Trans. Antennas Propagat.*, vol. AP-1, no. 4, 1970.



eteorological Society

Roger M. Lhermitte received the Ph.D. degree from the University of Paris in 1954.

He is currently a professor of meteorology at the University of Miami. He pioneered the meteorological use of radars with emphasis on the application of Doppler techniques for the processing and display of motion fields in precipitation systems from the radar data. Recently he developed a 94-GHz Doppler radar and used it to study clouds and precipitation.

Dr. Lhermitte is a Fellow of the American Meteorological Society.

Reprinted from JOURNAL OF ATMOSPHERIC AND OCEANIC TECHNOLOGY, Vol. 4, No. 1, March 1987
American Meteorological Society

A 94-GHz Doppler Radar for Cloud Observations

ROGER LHERMITTE

A 94-GHz Doppler Radar for Cloud Observations

ROGER LHERMITTE

Rosenstiel School of Marine and Atmospheric Science, University of Miami, Miami, FL 33149

(Manuscript received 21 August 1985, in final form 24 June 1986)

ABSTRACT

A Doppler radar operating at 3.2 mm wavelength was designed and assembled primarily for observation of clouds and precipitation. Phase detection of the radar signals which is required for Doppler operation is implemented through the use of a coherent oscillator phase locked on the transmitter pulse and used as a reference in the phase detector. The radar and associated signal processing techniques such as signal integrator and signal autocovariance estimator are discussed along with the Doppler performance of the radar. Also presented are the results of observation of ice and water clouds and also precipitation, which show the excellent Doppler capabilities of the radar in terms of accuracy of the mean Doppler and Doppler spectrum width.

1. Introduction

Observation of motion and growth of small hydrometeors, such as cloud droplets, is a powerful method for the study of the physics and dynamics of clouds in early stages of their development. A Doppler radar can be used for this purpose as it can monitor particle growth by measuring radar reflectivity, as well as simultaneously observing updraft and entrainment arising from latent heat released by condensation and/or freezing processes.

Centimeter wavelength radars may have the sensitivity required to detect small cloud droplets if these radars are equipped with a high power transmitter and a large aperture antenna. However, this approach involves bulky and heavy equipment while short range performance of such radars is usually limited by ground clutter. Since the backscattering from small targets such as cloud particles increases proportionally to λ^{-4} , a relatively low power radar operating at a shorter wavelength may constitute a better alternative. Signal absorption due to atmospheric gases, clouds and precipitation may be prohibitive at certain wavelengths. Figure 1, derived from Liebe's (1985) data, shows atmospheric attenuation for centimeter and millimeter wavelengths. At low humidity, spectral windows suitable for radar operation are clearly identified. The frequency bands are: K_a -band (35 GHz, $\lambda = 0.85$ mm), W-band (94 GHz, $\lambda = 3.2$ mm), F-band (140 GHz, $\lambda = 2.14$ mm) and G-band (220 GHz, $\lambda = 1.36$ mm). Note that in high humidity conditions, these "windows" are almost filled.

The shortest wavelength used in previous meteorological radars was $\lambda = 0.85$ cm (K_a -band). W-band radar components are now available at an affordable cost and, since the λ^{-4} improvement at 94 GHz is 40 dB with respect to X-band and 17 dB with respect to

K_a -band, a W-band Doppler radar can be considered for cloud observations. The W-band radar has the advantage of low power, lightness, small overall size and mobility. Thus, it can be easily transported in a small vehicle or installed aboard an airplane or an orbiting satellite. When compared to that of a longer wavelength radar, the W-band radar performance at short range is less likely to be degraded by ground clutter, thereby allowing observation of targets in close proximity of the radar (less than 100 meters).

A 94-GHz meteorological Doppler radar has been proposed (Lhermitte, 1981; Lhermitte and Frush, 1985). The radar has now been constructed and operated for cloud and storm observations; this paper presents the radar design, an evaluation of the radar performance, and some preliminary results.

2. Pulse Doppler Radar Design

a. Pulse Doppler techniques

Pulse Doppler radars measure the pulse-to-pulse echo phase change due to target motion and convert it into a Doppler frequency shift. Echo phase measurements can be performed using either one of the following techniques:

1) The transmitter pulse is produced by high power coherent amplification of a pulse sample of a frequency stable signal (STALO). The STALO signal is also used as a phase reference for incoming echoes;

2) The transmitter is a pulsed high power oscillator producing an RF pulse with a random phase. Either a frequency stable reference is used to measure the phase of both the transmitter pulse and the echoes associated with it, or the transmitter pulse synchronizes a coherent oscillator (COHO) acting as a phase reference for the incoming echoes.

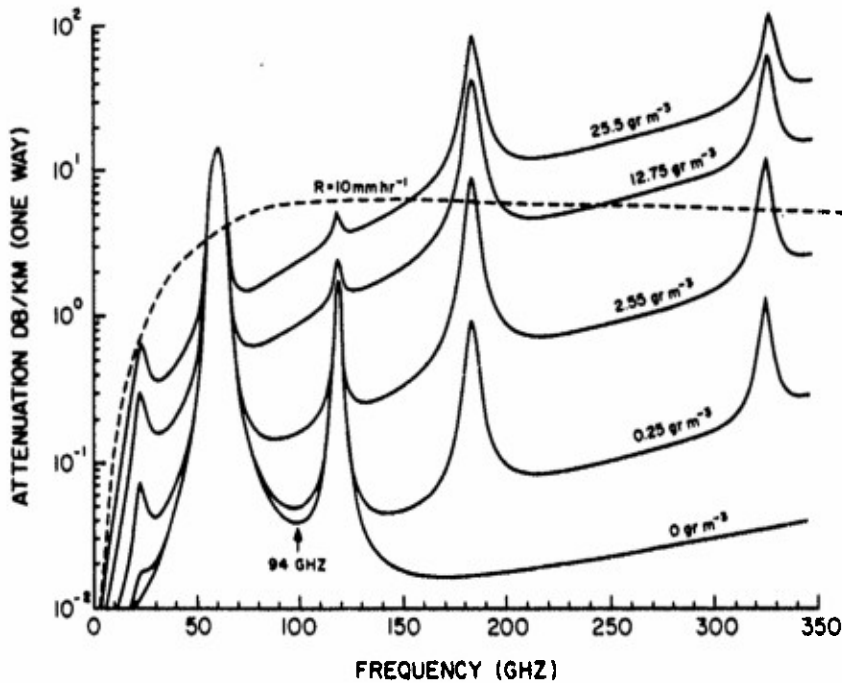


FIG. 1. Atmospheric gases absorption spectrum at the ground for various humidity conditions indicated by the specific humidity values. The absorption due to a 100 mm rainfall is also shown.

Phase coherent power amplification at 94 GHz can be implemented with a high power (1 kW peak, 5 watts average), low phase noise, pulse coherent amplifier referred to as an Extended Interaction Amplifier (EIA). The EIA appears to be an optimum device for a millimeter-wave Doppler radar because of its low phase noise; however, its cost is high. A much less expensive power oscillator tube, the Extended Interaction Oscillator (EIO) delivers the same power as the EIA and, used as a pulsed oscillator assisted by phase locking circuits, represents a more economical alternative. The EIO solution was selected for our Doppler radar design based on a phase-locking COHO technique.

A block diagram of the millimeter-wave Doppler radar is shown in Fig. 2; Fig. 3 shows a photograph of the equipment. The radar operates at a frequency of 93.95 GHz and is equipped with two (for transmission and reception) Cassegrain antennae (3-foot diameter dishes, 0.27° 3 dB beamwidth). The isolation between the two antennae exceeds 80 dB. The Cassegrain feed configuration allows the transmitter or receiver to be attached directly to the back of its respective antenna so that waveguide losses (3 dB m^{-1}) are minimized. The entire radar is set on a rigid frame that can be tilted and rotated in azimuth; thereby offering antenna scanning capabilities.

b. Transmitter

Doppler radars with magnetron transmitters have been implemented at K_u -band (Pasqualucci et al., 1983;

Hobbs et al., 1985). A magnetron delivering 10 kW at 94 GHz is available off-the-shelf, but its choice was rejected because of short life expectancy and unknown intrapulse phase noise. The EIO has a demonstrated longer life and is believed to have lower phase noise, so that even if it delivers less power (1 kW peak), it was considered a better solution. Also, the EIO can be gated by applying a low power pulse to an input grid which controls the high power output pulse. The dc high voltage main power source is constantly applied to the tube, and there is no need to switch on a large amount of power to produce the transmitter pulse, a basic requirement for pulsed magnetron operation. Therefore, frequency stability and full power are rapidly established at the start of the transmitted pulse and intrapulse frequency modulation is reduced.

Considerable effort was devoted to the modulator design. This and the EIO performance resulted in a transmitter pulse with a 3 ns rise time and a 5 ns fall time and intrapulse frequency modulation and phase noise small enough to ensure satisfactory Doppler operation. Figure 4 shows an example of the transmitter pulse at the output of the mixer used in the phase-lock operation. Note the very short rise and fall times. The pulse width can be set between 0.1 and 2 μs and the pulse repetition rate can be adjusted between 2.5 and 20 kHz. Although not considered in this early design, a transmitter pulse as narrow as 20 ns (3-meter range resolution) can be produced. Such an improvement of range resolution would require an increase of the IF frequency from its present value of approximately 60

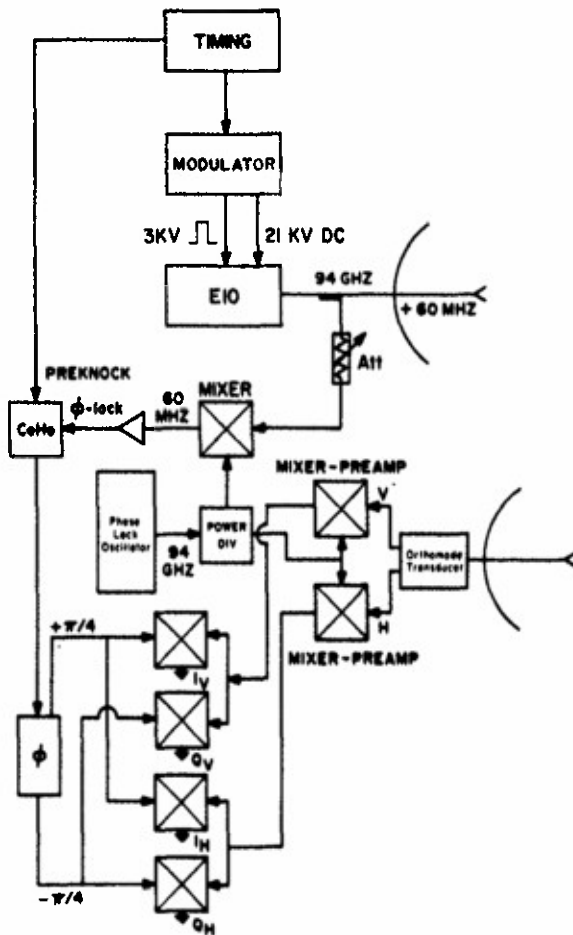


FIG. 2. Radar block diagram.

MHz to perhaps 160 MHz or more to accommodate the need for a larger bandwidth (50 MHz).

c. Receiver

Phase-coherent translation of rf echoes to the 55 MHz IF frequency is performed by a low-noise mixer-preamplifier and a 94-GHz frequency stable local oscillator (STALO). The STALO is a Gunn diode phase locked oscillator (PLO), referenced to a 100-MHz crystal oscillator. The PLO signal has the frequency stability and low phase noise of the crystal oscillator reference. The mixer-preamplifier noise figure is 6.5 dB double-sideband, and the equivalent receiver noise power is $P_n = -93$ dBm (30 MHz double sideband as a preamplifier-filter front-end is not available at 94 GHz).

A separate mixer-preamplifier provides a sample of the transmitter pulse downconverted to IF, needed for COHO synchronization. The 94 GHz rf signal input to the mixer is derived from a 20 dB coupler inserted between the EIO output and the transmitter antenna; an additional 80 dB attenuation in an attenuator-waveguide assembly sets the RF pulse at the input of

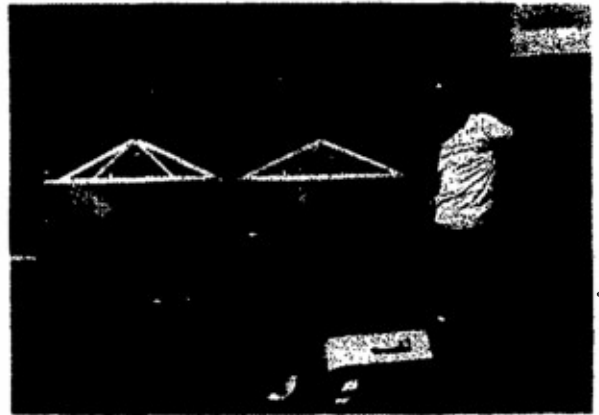


FIG. 3. Photograph of the Doppler radar.

the mixer to a -40 dBm power level. The IF phase reference pulse (3 GHz bandwidth) at the mixer output shown in Fig. 4 synchronizes the COHO oscillator when it starts to oscillate. The COHO continues to oscillate, retaining the phase of the reference pulse during the interpulse time, until it is disabled a few micro-seconds before the next transmitter pulse.

A conventional dual-mixer system acts as a phase detector producing the familiar coherent video composed of two in-phase, I, and quadrature, Q, signals. Figure 5 presents an example of the I or Q signal associated with the transmitter pulse as a test of radar phase coherence. Note that the COHO frequency is intentionally shifted (approximately 2 MHz) with respect to the IF frequency and that phase coherence is still obtained. The low phase noise performance of the radar was further tested by observing the coherent video for fixed targets shown in Fig. 6.

3. Signal processing, radar sensitivity and calibration

a. Signal processing

The I and Q coherent video signals and the signal at the output of a logarithmic amplifier are sampled and digitized at range gate positions by three 8-bit an-

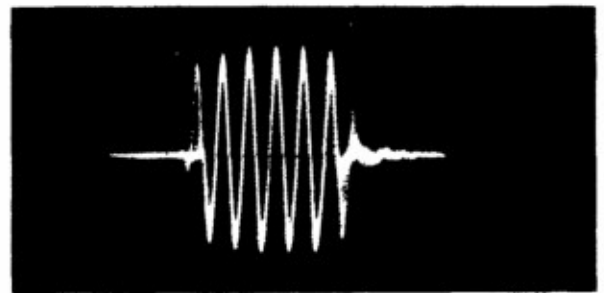


FIG. 4. IF signal (55 MHz) at the output of the mixer-preamplifier used for phase lock. Mixer inputs are 94 GHz EIO transmitter pulse and PLO CW signal. Pulse width is 0.1 μ s.

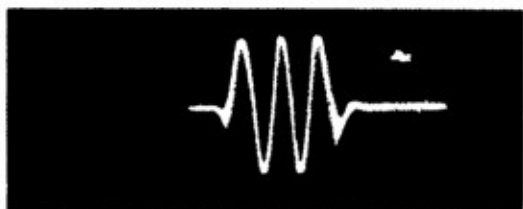


FIG. 5. I or Q coherent video signal at the output of the phase demodulator occurring during the transmitter pulse. PRF: 10 KHz, 2-second exposure time, pulse width 1.5 μ s, COHO/IF frequency offset 2.0 MHz.

alog-to-digital converters. The converters are of the flash type with a conversion time less than 100 ns. Video samples can be recorded at 100 ns time intervals if a fast buffer memory is used, and Doppler spectra calculated off-line. This method is complex and leads to a relatively slow data throughput rate, considerably smaller than that achieved using a signal processing autocovariance technique originally proposed by Woodman and Hagfors (1969) and named "pulse-pair" (PP) later. In the first phase of this project, directed primarily toward exploring the millimeter wave Doppler radar capabilities for meteorological research, we have selected the PP method to provide continuous processing of mean Doppler at all available range gates. Our PP processor requires a minimum of 300 ns to perform the complex multiplication and integration needed for calculation of the autocovariance in real-time, therefore setting the limit to the minimum available time interval between range gates. The processor can calculate signal autocovariance at all the range gates available in the pulse repetition period up to a maximum of 1024.

The PP method has often been discussed (i.e., Doviak and Zrnić, 1983), and the following is a brief summary of the theory and operation of the PP processor designed for this project. The complex autocorrelation function of the backscattered signal is:

$$\rho(\tau) = \rho_c(\tau)e^{-2\pi f_0 \tau} \quad (1)$$

where τ is the time lag and $\rho_c(\tau)$ is the autocorrelation function amplitude only dependent on signal bandwidth. The f_0 is rigorously equal to the mean frequency (first spectral moment) for symmetric spectra but only very slightly dependent of spectrum nonsymmetry (Sirmans, 1975).

We can express $\rho_c(\tau)$ by:

$$\rho_c(\tau) = e^{-2\pi^2 \sigma^2 \tau^2} \quad (2)$$

where σ^2 is the spectral variance. Equation (2) applies rigorously to a Gaussian shape spectrum; however, it is a very close approximation for most spectrum shapes (Lhermitte and Serafin, 1984).

In our processor, the real and imaginary terms representing the complex signal autocovariance for a time lag equal to the interpulse time and the $\langle I^2 + Q^2 \rangle$ term

representing the zero-lag reference are calculated in real time at each range gate and recorded on magnetic tape (16-bit words). An off-line computer performs the calculation of f_0 and σ^2 following Eqs. (1) and (2).

Some of the observations presented here were made in very low signal-to-noise conditions. White noise does not bias the estimate of f_0 (it only increases its variance). However, the noise contribution, P_n , to the $\langle I^2 + Q^2 \rangle$ term representing the zero lag autocovariance amplitude reference must be removed in the spectral width computations, as this term must relate to signal autocorrelation function amplitude only. The long signal integration time used in our observations allows precise determination of P_n in echo free regions, which can thus be subtracted from $\langle I^2 + Q^2 \rangle$ for spectral width computation. We have used this procedure for the spectrum-width data presented here. However, this method only removes white noise contribution from the receiver. All white noise contributions including the presence of noise in backscatter or radar phase noise can be canceled by calculating ρ_1 and ρ_2 for two pulse-repetition periods τ_1 and τ_2 . The signal spectral variance is then expressed by (Lhermitte and Serafin, 1984)

$$\sigma_s^2 = \ln(\rho_1/\rho_2)/[2\pi^2(\tau_1^2 - \tau_2^2)] \quad (3)$$

This improved noise correction method will be implemented later when the radar is equipped with dual pulse repetition rate capabilities.

b. Atmospheric and hydrometeor absorption

The absorption spectrum for atmospheric gases is shown in Fig. 1. The 3-mm wavelength is inside a window that contains the skirts of the 60 GHz and 118 GHz O_2 lines, and also the skirt of the intense 184 GHz H_2O line which makes absorption in this window strongly dependent on atmospheric water vapor. Figure

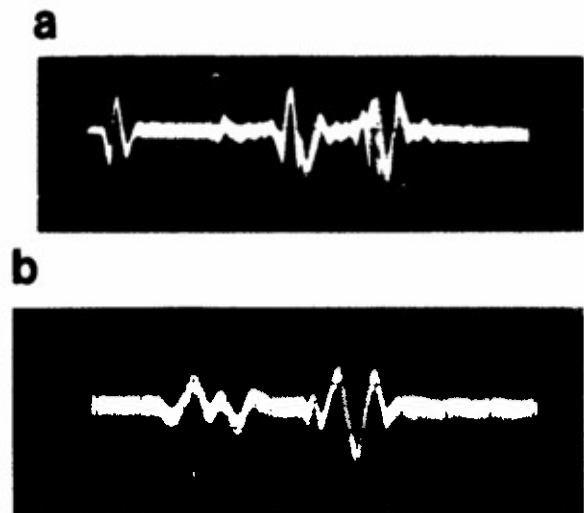


FIG. 6. Coherent video signal (I or Q) on fixed targets. a, targets at 750 meters and 1 km; b, targets at ~ 2 km on an expanded scale.

7 shows the absorption coefficient at 94 GHz derived from Liebe's (1985) data, as a function of specific humidity. One sees that with 25 g m^{-3} humidity, the absorption coefficient is about 2 dB km^{-1} (one-way). For a vertically pointing radar beam, zenith absorption is much less significant because of the systematic decrease of both water vapor amount and pressure broadening with altitude. Shimabukuro and Epstein (1970) have collected a large number of observations of clear air attenuation at 94 GHz using solar radiation as a source; an empirical least squares fit of their measurements of zenith absorption versus precipitable water is shown in Fig. 8. The same data computed by Liebe (1985) from laboratory experiments are also presented for comparison.

For small spheres of diameter D , the absorption cross section $Q_a = (\pi^2 D^3 / \lambda) \text{Im}(-K)$ (Rayleigh approximation), where $K = (m^2 - 1)/(m^2 + 2)$ and m is the complex index of refraction. At 94 GHz, $m = 3.5 + 2.05i$ for water (25°C) and $m = 1.78 + 4.76 \times 10^{-4}i$ for ice (Ray, 1972), so $\text{Im}(-K) = 0.1402$ for water and 2.5×10^{-2} for ice. The Q_a is proportional to particle mass so the absorption coefficient is proportional to cloud or fog water content. The calculated one-way absorption per g m^{-3} of liquid water varies almost linearly with temperature from 3.47 dB km^{-1} at 23°C to 4.8 dB km^{-1} at 0°C .

Precipitation particles whose diameter exceeds approximately 0.2 mm are not Rayleigh absorbers at 94 GHz, and Q_a must be calculated using the Mie equations. Furthermore, the scattering cross section Q_s exceeds Q_a for water particles with a diameter greater than 1 mm . At 94 GHz, the attenuation coefficient (including scattering) β (in dB km^{-1}), calculated for rainfall and assuming a Marshall-Palmer (Marshall

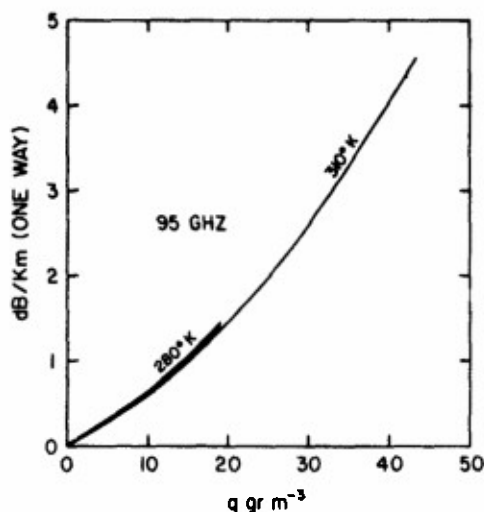


FIG. 7. Atmospheric attenuation at 94 GHz as a function of specific humidity in g m^{-3} , at ground pressure and for two temperatures, 280 and 310 K .

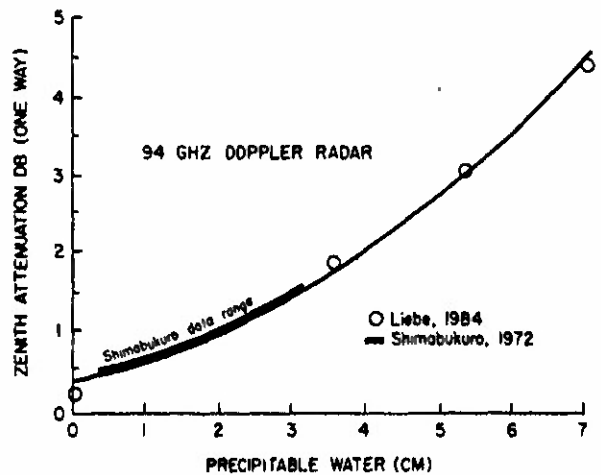


FIG. 8. One-way zenith absorption as a function of precipitable water. The solid line is the model proposed by Shimabukuro as a least squares fit of his data. The heavier line indicates the range of the Shimabukuro data. The circles are the values proposed by Liebe on the basis of his experiments. Note the very good agreement between two completely independent sets of data.

and Palmer, 1948) drop size distribution $N(D) = N_0 \exp(-\Lambda D)$, $N_0 = 8 \cdot 10^4$ and $\Lambda = R^{0.21}$, R rainfall in mm h^{-1} , is approximately $\beta = 0.9R^{3/4}$; this equation agrees reasonably well with experimental measurements.

c. Rayleigh-Mie backscattering

Water or ice spheres with a diameter smaller than approximately $\lambda/4$ are Rayleigh scatterers and their radar cross section, S_r , is

$$S_r = \pi^5 |K|^2 D^6 / \lambda^4. \quad (4)$$

At 94 GHz, $|K|^2 = 0.813$ for water (temperature 20°C) and 0.173 for ice. Since $|K|^2$ does not vary significantly for longer wavelengths, S_r for Rayleigh scatterers at W-band is 17 dB . This is 40 dB higher than that at K_u and X-band, respectively. The S_r values calculated at 94 GHz using the Mie equations are shown in Fig. 9 as a function of particle diameter, D , for water (0° and 20°C) and ice. Rayleigh scattering, which is acceptable for $D > 8 \text{ mm}$ particles, is also indicated in Fig. 9. Above $D \sim 1.8 \text{ mm}$, the Mie backscattering values oscillate and are consistently 15 to 25 dB below Rayleigh backscattering. The Mie computations for K_u -band and X-band are also shown in Fig. 9 for comparison.

For Rayleigh scatterers, S_r is 6.7 dB less for ice than it is for water. However, at 94 GHz, precipitation particles with $D > 1 \text{ mm}$ are more efficient scatterers if they are made of ice rather than water (see Fig. 9). This fact was recognized long ago for centimeter waves detecting large hailstones (Atlas et al., 1960). However, at 3-mm wavelength the increased backscatter for ice

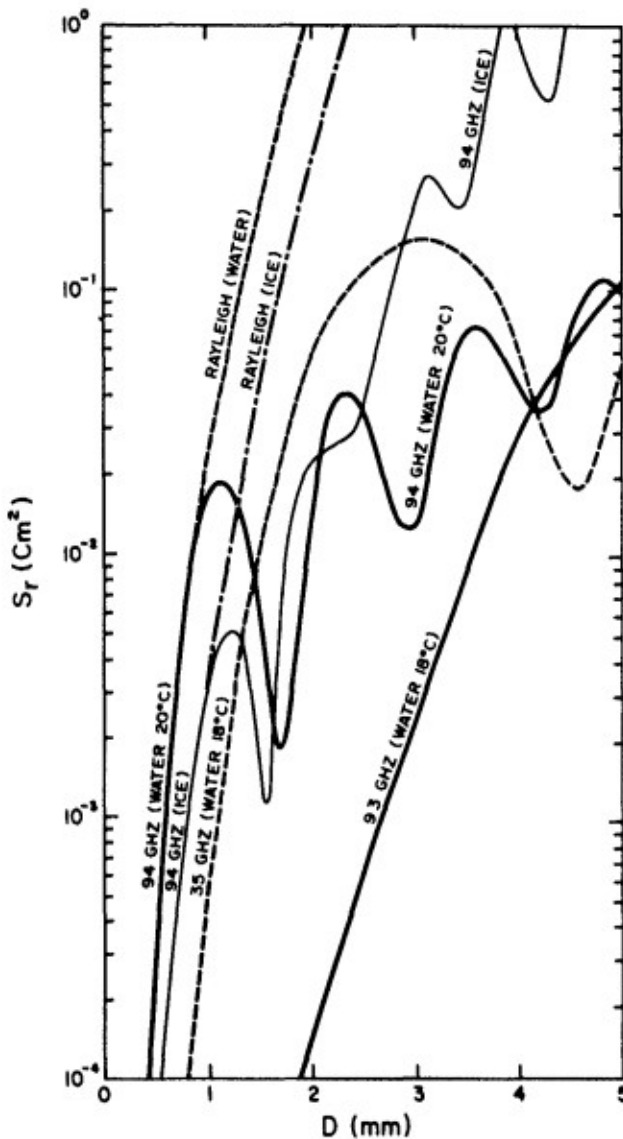


FIG. 9. Backscattering cross section of water and ice spheres versus their diameter at 94 GHz. The results for 35 GHz and 9.3 GHz are also indicated for reference.

occurs for millimeter size particles commonly found in clouds. As a comparison, the increased backscatter for ice at K_u -band occurs for particle sizes $D > 7$ to 8 mm, definitely greater than the size of ice particles in clouds except for large graupel and hailstones.

Radar reflectivity is expressed by $\eta = \int N(D) \times S_r(D) dD$, where $N(D)$ is the drop size distribution. The reflectivity factor is $Z = \int N(D) D^6 dD$ and implies Rayleigh backscattering. At 94 GHz and assuming Rayleigh scattering the relationship between Z in $\text{mm}^6 \text{m}^{-3}$ and η in cm^{-1} is

$$Z = 4.21 \times 10^7 \eta. \quad (5)$$

Precipitation particles at 94 GHz are Mie scatterers and an equivalent radar reflectivity factor, Z_e , derived

from Eq. (5) using the actual η calculated using Mie backscattering cross sections, must be expressed.

The Z_e computations at 94 GHz, based on a Marshall-Palmer dropsize distribution, are presented as a function of rainfall rate, R , in Fig. 10 in mm h^{-1} . For Rayleigh scatterers Z is also shown and one sees that Z_e is always smaller than Z , with Z/Z_e increasing to 25 dB for $R = 100 \text{ mm h}^{-1}$. Since the ratio S_r/M , where M is the particle mass, decreases with increasing D , a narrow dropsize distribution concentrated around the virtual maximum raindrop size (5–6 mm), produces even slightly less Z_e values for the same precipitation intensity. The 3-mm wavelength radar reflectivity of rainfall cannot be greater than approximately $1.5 \times 10^{-5} \text{ cm}^{-1}$, or an equivalent Z_e of 30 dBZ, as compared with 55 dBZ values or more for centimeter wavelength radars. Large ice particles (i.e. hailstones) can increase Z_e to more than 30 dBZ, still less than the radar reflectivity observed using centimeter-wave radars. The fact that, at 94 GHz, large raindrops do not dominate backscatter renders the relationship between radar reflectivity and rainfall rate much more sensitive to small particle deficiency (compared with a M-P distribution) often observed in drop size distribution measurements. This may invalidate the use of a M-P drop size distribution for the interpretation of radar reflectivity data at a 3-mm wavelength.

The expression for mean Doppler velocity, \bar{V} , at vertical incidence is

$$\bar{V} = \frac{\int N(D) S_r(D) V(D) dD}{\int N(D) S_r(D) dD} \quad (6)$$

where $V(D)$ is the particle vertical velocity. Assuming that precipitation particles fall at their terminal velocity and using a M-P dropsize distribution and the Mie scattering function allows calculation of the V - R re-

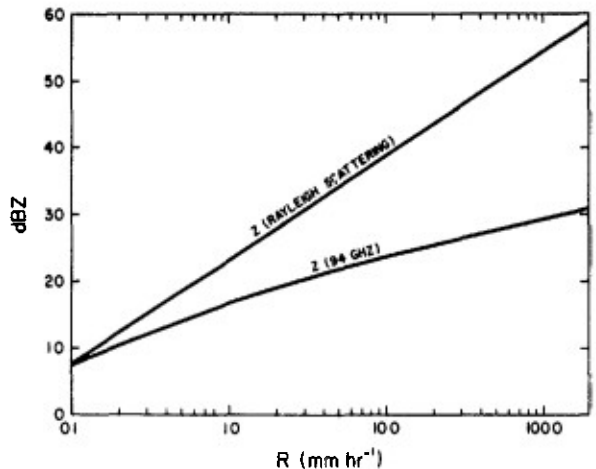


FIG. 10. Radar reflectivity factor, Z , as a function of rainfall rate for a long-wavelength radar (Rayleigh scattering) and a 94-GHz radar. Marshall-Palmer dropsize and the Gunn-Kinzer vertical velocity/diameter relationship are used.

relationship at 94 GHz shown in Fig. 11 for rainfall at sea level, together with the \bar{V} - R relationship proposed by Joss and Waldvogel (1977) for microwave radar. At 94 GHz \bar{V} for very heavy rainfall (100 mm h⁻¹) is 5 m s⁻¹ instead of 9–10 m s⁻¹ for the J-W relationship, owing to the relatively stronger contribution to backscattering (compared to microwave) by smaller particles.

d. Radar equation and radar parameters

With the acceptable assumption that meteorological targets fill the radar beam completely, radar reflectivity can be expressed by the following simplified radar equation, presented in a logarithm form for convenience.

$$10 \log \eta = 10 \log P_r - 10 \log P_t + 10 \log 4\pi R^2 - 10 \log h - 10 \log A_e \quad (7)$$

where η is the radar reflectivity of the meteorological scatterers, P_r the echo power, P_t the transmitter peak power, $h = tc/2$ the scattering volume radial dimension, A_e the effective area of the receiving antenna, and R the target distance.

The transmitter antenna efficiency including the loss of signal in the antenna sidelobes must be included in A_e , as well as the loss of sensitivity arising from the only partial merging at close range of essentially parallel antenna beams. The antenna radiation pattern is not accurately known, but it is unlikely that the antenna efficiency and beam merging correction exceeds 3.5 dB.

With this correction included, and using $P_t = 1$ kW peak, a 3-foot antenna diameter, and $h = 60$ m (400 ns pulse), the radar reflectivity is

$$10 \log \eta = P_r(\text{dBm}) - 23.5 + 20 \log R \quad (8)$$

where η is in cm⁻¹, P_r is the received signal intensity in dBm, and R the target distance in km.

Or, in dBZ:

$$\text{dBZ} = P_r(\text{dBm}) + 53 + 20 \log R. \quad (9)$$

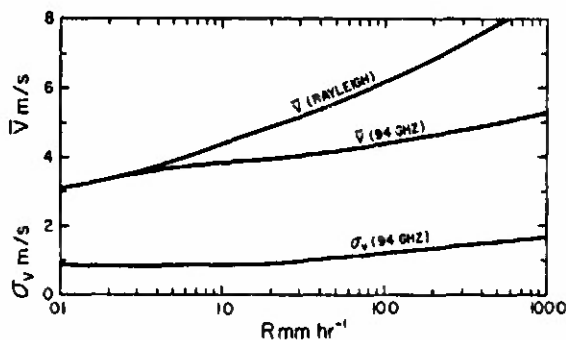


FIG. 11. Mean Doppler velocity at vertical incidence as a function of rainfall intensity for centimeter wave radar (Rayleigh scattering accepted), and for 94-GHz radar data. M-P dropsize distribution and Gunn-Kinzer vertical velocity/size relationship are used. The spectrum width, σ_v , for the 94 GHz data is also presented.

At a 3 km range, a cloud reflectivity of approximately -30 dBZ will produce a signal equal to noise (-93 dBm); this is the radar reflectivity at 94 GHz of a 1 g m⁻³ liquid water cloud composed of 10 μ particles.

e. Signal-to-noise improvement and radar receiver calibration

This section discusses the effective signal-to-noise gain due to signal integration, and signal intensity calibration methods. The results presented here were obtained using a 3.2-sec signal dwell time and a 10 kHz PRF, providing 32 000 samples for the computation of signal autocovariance and signal intensity for each range gate. This unusually large sample size results in very small variance of the estimates and enables measurement of signal intensities which are much less than the receiver noise.

Mean intensity which yields radar reflectivity is the mean square of the backscatter amplitude. However, mean signal intensity is usually derived from integrating the signal at the output of a radar receiver and, if the radar receiver input/output transfer function is not exactly quadratic, the receiver calibration performed using a nonfluctuating signal must be corrected. For a logarithmic amplifier, this correction is +2.5 dB for large signals and 0.5 to 1 dB for weak signals for which the logarithmic amplifier transfer function becomes almost linear (Lhermitte and Kessler, 1966). In our radar processor, an arbitrary correction of +0.5 dB, below -80 dBm and +2.5 dB above -80 dBm, is applied to the logarithmic signal integrator output. The I and Q signals below saturation are produced by an essentially linear receiver-phase detector transfer function and the $\langle I^2 + Q^2 \rangle$ integration data need not be corrected.

A calibrated signal source at 94 GHz was not available for calibration of the radar receiver and we had to consider an alternate radar receiver/integrator calibration technique. Let P_n be the 94-GHz noise power and P_s the received signal at the input of the millimeter wave receiver. Assuming independent (Gaussian) processes the signal plus noise power is $P_{s+n} = P_s + P_n$. The change from P_n to P_{s+n} associated with the occurrence of a signal, can be expressed by the ratio $\alpha = P_{s+n}/P_n$. The signal-to-noise ratio is thus $P_s/P_n = \alpha - 1$, or:

$$(\text{dBm})_{\text{signal}} = (\text{dBm})_{\text{noise}} + 10 \log(\alpha - 1). \quad (10)$$

The relationship between α and P_s/P_n is shown graphically in Fig. 12. If the integrator output, P_s , associated with an echo exceeds the noise rms fluctuation, the signal is detected. With our dataset (32 000 samples at each range gate, see below) the detection threshold was found to be -20 to -25 dB below the noise. This result agrees well with the $1/(N_e)^{1/2}$ theoretical signal-to-noise improvement expected from N_e statistically independent samples.

Only the signal-to-noise ratio, P_s/P_n , is measured by the integrator and the noise power P_n must be assessed

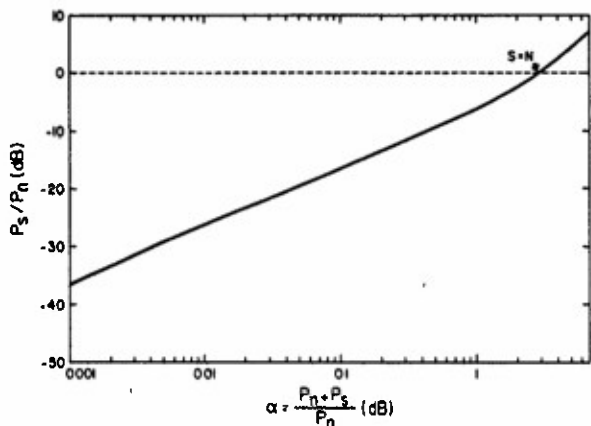


FIG. 12. Signal-to-noise ratio S/N as a function of the $(S + N)/N$ ratio observed by the radar.

for the received signal intensity to be measured. Knowing the receiver noise figure and bandwidth, P_n can be calculated. A laboratory measurement of the mixer-preamplifier noise figure can be performed, but it requires extensive equipment and a more convenient way is to measure the receiver performance using solar radiation as a reference source. The quiet sun radiation temperature is 8000°K at 94-GHz. The sun can be considered as a blackbody emitting a signal power (radiation flux) 14.2 dB above a 300°K reference. The radar antenna 3 dB beamwidth is approximately 0.27° , and the solar disc diameter is (0.53°). If the radar beam axis is centered on the solar disc and assuming a gaussian shape radar beam and a uniform sun brightness, yields less than 2% (0.1 dB) signal loss with respect to a radiation source filling the beam completely.

Using an integrator with approximately 0.5-sec integration time (a few degrees Kelvin precision with 30 MHz receiver bandwidth), it was found that when the antenna was pointed toward the solar disc, the solar radiation power level finally reaching the mixer was (fortuitously) equal to the mixer noise within ± 0.2 dB. Neglecting the lower temperature atmospheric radiation, we calculated the solar signal power at the input of the radar receiver by considering only solar signal attenuation in the sun-radar receiver path. We estimated: 1.5 dB atmospheric attenuation from temperature and humidity soundings, $2 \text{ dB} \pm 1 \text{ dB}$ loss for antenna efficiency including sidelobe effects, 1 dB loss in waveguides, and 3 dB for natural radiation received by a polarized receiver, or a total of 7.5 dB. This yields a 6.6 ± 1.5 dB noise figure which agrees with the 6.5 dB quoted by the manufacturer of the mixer. In addition to its simplicity, this method allows easy periodic checks of the mixer performance.

A 6.5 dB noise figure and a 30 MHz double sideband bandwidth is equivalent to a -93 dBm receiver noise power, P_n . Knowing P_n , P_s can be derived from the P_s/P_n measurements and an absolute calibration of the radar receiver from antenna input to integrator output

can be established. The accuracy in measurement of receiver noise power and the knowledge of the receiver transfer function are the main factors governing the accuracy in measuring mean signal intensity. For P_s greater than P_n , we believe that the uncertainty in our P_s measurement does not exceed ± 2 dB and can degrade to ± 3 dB for $S/N = -20$ dB.

f. Precision of mean velocity and spectral width estimates

The ability of the radar to provide reliable measurement of mean Doppler and spectrum width for a signal

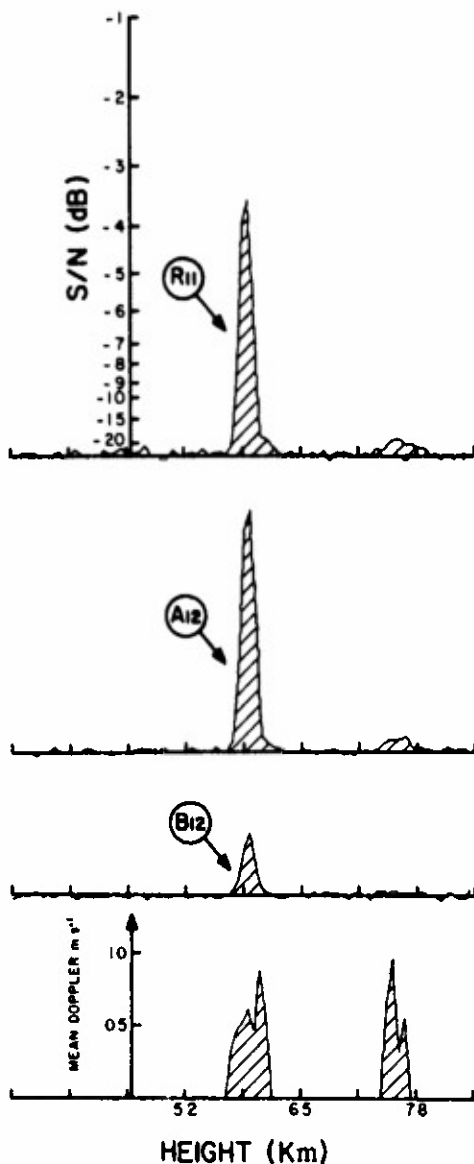


FIG. 13. Power term, $R_{11} = \langle I^2 + Q^2 \rangle$, and autocovariance real, A_{12} , and imaginary B_{12} terms for weak signals with signal-to-noise indicated for R_{11} . 32 000 samples contribute to the estimates evaluated at each range gate. The mean Doppler estimates are also shown.

well below the receiver noise, is illustrated in Fig. 13 which shows weak echoes at an altitude of approximately 7 km. The real and imaginary autocovariance terms are shown together with the $\langle I^2 + Q^2 \rangle$ power term. Fig. 13 shows the well-defined mean Doppler velocity (0.5 to 0.7 m s⁻¹ downward) obtained for two echoes (-96 dBm and -113 dBm). The fluctuation level of the autocovariance real and imaginary terms indicates that the mean Doppler uncertainty is about ± 1.5 and ± 16 cm s⁻¹ for the -96 dBm and -113 dBm echo, respectively. The theoretical expression for the variance, σ_m^2 , of a PP mean Doppler estimate for large S/N is [Zrnić, 1979]:

$$\sigma_m^2 = \frac{\sigma_v \lambda}{8(\pi)^{1/2} T} \quad (11)$$

where σ_v is the Doppler spectrum standard deviation, λ the radar wavelength, and T the signal dwell-time. With $\lambda = 3$ mm, $T = 3.2$ s, and $\sigma_v = 1$ m s⁻¹, $\sigma_m = 0.9$ cm s⁻¹.

This theoretical precision of the mean Doppler estimate was compared with the time stability of actual measurements of mean Doppler obtained in stratified cloud conditions for which steadiness of the velocity profiles is expected. Two examples of data obtained in such stratified conditions are shown in Fig. 14. Persistent fine structures in the two profiles are observed. With an echo translation speed of 5 m s⁻¹ and a radar beam cross section of 5 to 50 meters (1 to 10 km range), the profiles should be nearly statistically independent. Above the 0°C level (4 km altitude) where particles are expected to be ice crystals, 60% of the profile-to-profile peak velocity differences are less than 3 cm s⁻¹, and 85% are less than 6 cm s⁻¹. Between the 4 km altitude and ground level, in a region where liquid droplets are expected, 60% of the same velocity differences are less than 2 cm s⁻¹ and 90% less than 5 cm s⁻¹. There are signs of convection above 6 km and some of the velocity variability may be due to actual change of the velocity in 5 seconds. Further statistical analysis of profile to profile velocity differences indicates that the standard deviation of the 5-second velocity difference is typically less than 1.3 cm s⁻¹ in S/N > 10 dB regions. This is slightly greater than that predicted by Eq. (11) and may be explained by actual time variability of the mean vertical velocity.

4. Observations

In this section we present selected observations to illustrate the capabilities of the 3 mm wavelength Doppler radar. The radar was originally assembled and tested in Miami. Observations of thunderstorms in the Miami area were made just after testing of the radar. The thunderstorms were at a 20 to 30 km range. With the high humidity conditions (6 cm of precipitable water and 28 g m⁻³ specific humidity at ground level),

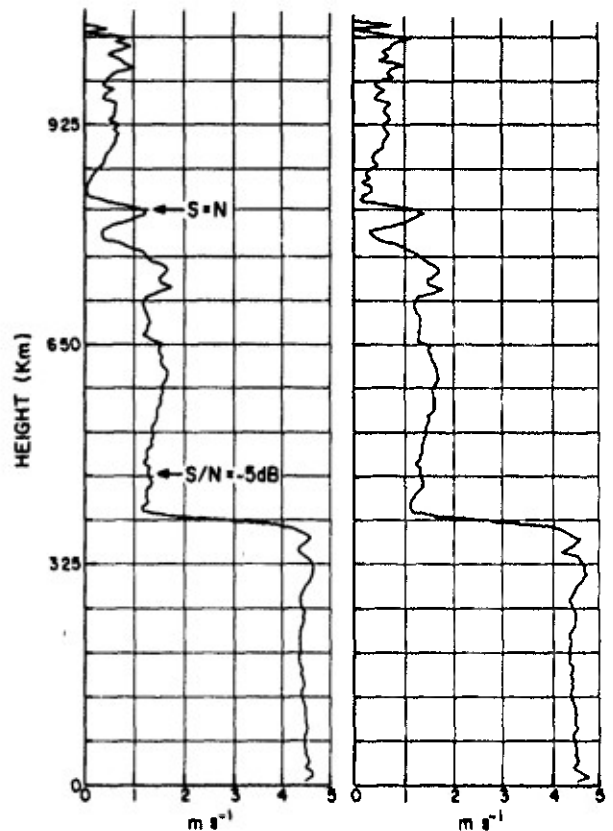


FIG. 14. Vertical profiles of mean Doppler observed in a stratified cloud which may contain very light precipitation. The two profiles are obtained from processing of two independent sets of data taken 5 seconds apart. Note the sudden acceleration of the mean Doppler velocity at the 3.9 km altitude associated with particle melting.

the one-way zenith absorption was almost 3 dB and the one-way signal attenuation at the ground was 2.5 dB km⁻¹. The two-way absorption between a thunderstorm at 20 km and the radar was 12 dB for a 30° elevation angle, increasing to 50 dB for a 7° elevation angle. In such high humidity conditions, the minimum elevation angle for which echoes were detected was 20° to 30° so only the top of thunderstorms could be observed. For example, a storm at 20 km observed with a 34° elevation angle (altitude in the storm 11.2 km), produced a -71 dBm echo. With an estimated two-way clear air absorption of 11 dB, and an additional estimated attenuation of 10 dB (2 dB km⁻¹ two-way, 5 km depth) in an intervening cell revealed by the presence of an echo, the backscattered signal intensity in the storm core was estimated to be -50 dBm. This is equivalent to a 26 dBZ radar reflectivity which is reasonable for targets at a height of 11 km in a Florida thunderstorm, and also considering the virtual 20 to 28 dBZ maximum which can be observed at 94 GHz. Scanning horizontally and vertically in search of the strongest echo in the storms, indicated that the maximum echo intensity at a mean range of 20 km was

about -70 to -75 dBm and was observed at 30 to 40° elevation angles.

Observations using a vertically pointing beam were made later at Miami and also at Boulder, Colorado (in association with the National Center for Atmospheric Research). Cirrus layers were always detected with the millimeter-wave radar, even if they were not observed visually. This must be due to the fact that most ice particles are large and likely to be efficient Mie scatterers at the short 3-mm wavelength (see Fig. 9). Ice particles in cirrus are prisms with a typical length of 0.5 mm and a ratio of length to breadth varying from one to five (see the classical study by Weickman, 1947, for instance) and clusters of crystals reaching a size of 2 mm can be found. Note that a cirrus cloud containing one spherical ice particle of 2 mm size (Mie backscattering cross section 2 mm²) per m³ has a 2×10^{-8} cm⁻¹ reflectivity equivalent to approximately 0 dBZ at $\lambda = 3$ mm. In comparison, a fair weather cumulus having the same water content and with droplet size distribution extending to 10 to 15 μ has a reflectivity equivalent to -40 to -35 dBZ.

Observations of vertical velocity in cirrus clouds at altitudes of 7 – 10 km indicated that particles are typically moving downward with a velocity on the order of 0.5 to 1 m s⁻¹, sometimes reaching 2 m s⁻¹. Occasionally, upward motion of approximately 1 m s⁻¹ was observed but only at the cirrus top with downward motion observed below. Since cirrus clouds are so well observed at $\lambda = 3$ mm, a Doppler radar operating at this wavelength may be an excellent tool for observations of cirrus kinematics and could provide insight into high altitude turbulence.

Radar observations using the same vertically pointing radar beam mode were also made at the Miami site on a cloud apparently related to the outflow of a dissipating thunderstorm. The thunderstorm was located approximately 30 km West of the radar site and the first echo seen by the radar came from a high altitude (12 to 14 km) cirrus cloud which was probably an extension of the storm anvil. Later, the echo developed downward and finally reached the ground. The downward development of the cloud seemed to be related to the sinking motion of ice crystals which appeared first in the cirrus layer 10 to 12 km over the radar. There was never any significant precipitation on the ground, although a few sparse small drops (diameter less than 1 mm) were observed a few minutes before the observations were terminated.

Stratified precipitation is usually characterized by the presence of a well defined "bright band" (Austin and Bemis, 1950), or more properly "melting band" (MB), which appears as a maximum of radar reflectivity 50 to 150 m below the 0° C level. This enhancement of radar reflectivity is attributed partly to the increase of the $|K|^2$ term in the expression of S , associated with the change from ice to water. The passage of precipitation particles through the 0° C altitude level is also

characterized by a sudden increase of their terminal velocity as they evolve from a high drag, low density ice crystal-snowflake structure to a high density droplet or raindrop (i.e., Lhermitte and Atlas, 1963).

Although many MB observations with centimeter-wave radars have been done in the past, we were delighted to find that a MB could be clearly identified using a 3-mm wavelength radar for which particles larger than 0.8 mm are not Rayleigh scatterers. Samples of mean Doppler velocity vertical profiles observed with our millimeter-wave radar in the cloud mentioned above are presented in Fig. 14 and also in Fig. 15 where vertical profiles of mean signal intensity range, normalized to 1 km, and spectral variance are also shown. The most striking feature in the velocity profiles is indeed the drastic change of mean Doppler from approximately 1.2 m s⁻¹ to approximately 4.5 m s⁻¹, when particles go through the melting level. These observations were made at a time when the parent storm had almost completely dissipated and the vertical velocity profiles were fairly steady. This is confirmed by inspection of Fig. 14 which exhibits remarkable similarity for two velocity profiles taken five seconds apart.

At the altitude where particle melting is suspected from the increase of mean Doppler, there is a sudden 6 to 8 dB reflectivity increase. Further inspection of many profiles acquired successively at five-second time interval, indicates that this very localized reflectivity increase attributed to melting was between 6 and 9.5 dB with a remarkably repeatable slope of 0.6 dB/10 m. The presence of such a reflectivity enhancement attributed to melting indicates that the particles are Rayleigh scatterers, i.e. they are smaller than 1.5 mm (see Fig. 9). Detail study of the reflectivity and velocity vertical profiles indicates the sharp reflectivity change occurs at 30 to 50 m above the altitude at which particles start to accelerate, and is completed at an altitude where a 2.8 – 2.9 m s⁻¹ mean Doppler (middle of the accelerating curve) is observed. There is no significant decrease of reflectivity just below the MB as seen in classical observations of MB by centimetric wavelength radars (i.e., Lhermitte and Atlas, 1963).

Previous observations of the MB in precipitation conditions showed a systematic downward increase of radar reflectivity starting a kilometer or so above the 0° C level MB. This is not observed here. Rather, a continuous downward reflectivity decrease of both signal intensity and vertical velocity is observed starting a few hundred meters above the MB. This may indicate that the cloud particles we observe just above the MB are single crystals (or more likely prisms) having a small collision efficiency with the surrounding supercooled droplets because of their smooth and simple shape and their small terminal velocity. On the contrary, the large snowflakes observed using a microwave radar in precipitation conditions have a complex structure and a substantial terminal velocity. The snowflakes reside in a high liquid water environment and they are likely to

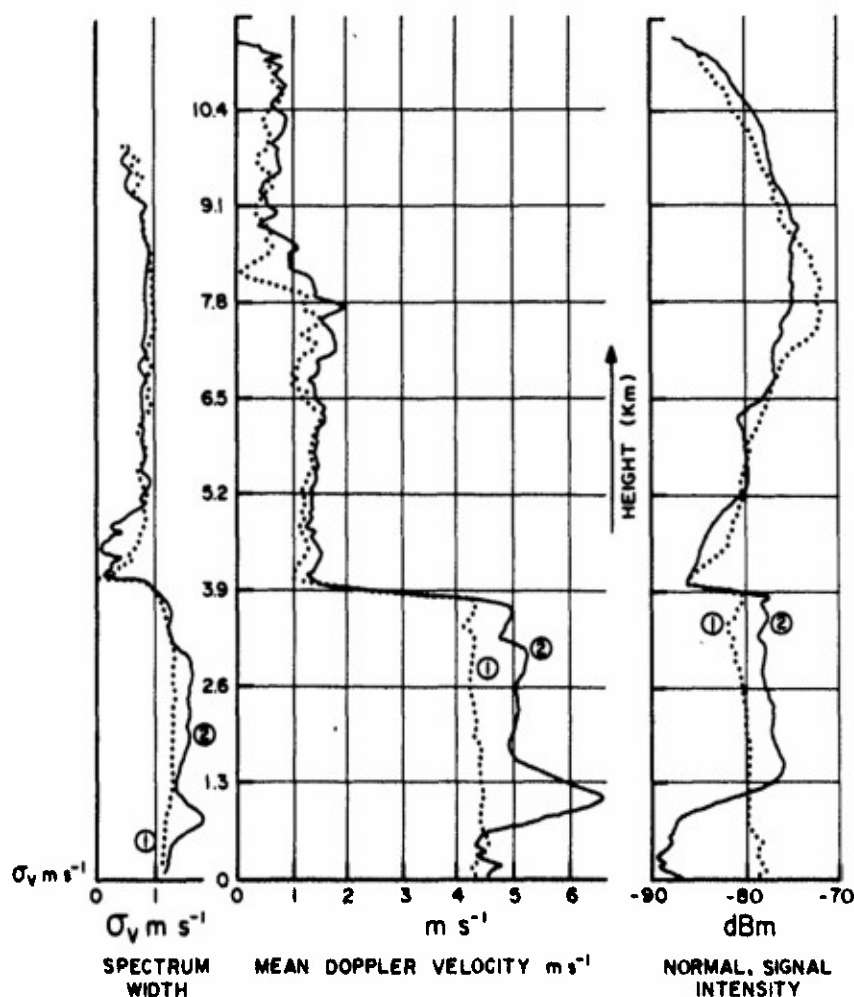


FIG. 15. Vertical profiles of radar signal intensity corrected for range (right), mean Doppler velocity (center), and spectrum width (left). Profiles labeled 2 are observed 10 minutes after profiles labeled 1.

grow rapidly through capture (riming) of the surrounding cloud droplets, which results in an increase of both radar reflectivity and mean Doppler velocity in the layer just above the MB.

Our millimeter-wave radar observations indicate that at higher altitudes above the MB, the velocity and reflectivity profiles remained fairly steady over a long period of time (one hour). However, below the MB, there are significant time variations of the velocity and reflectivity profiles over 5 to 10 minute periods. This is illustrated by the profiles presented in Fig. 15 which are observed 10 minutes apart. In the profiles labeled 1, the mean Doppler velocity, the radar reflectivity, and the spectrum width below the MB do not exhibit much variation with altitude. The spectral width has an average value of (1.2 m s^{-1}) which is comparable with the value predicted for a few millimeter per hour M-P rainfall not observed at the ground. This relatively high spectrum width may be due to the presence of a

large concentration of cloud droplets coexisting with another much smaller population of 0.5 mm to 1 mm diameter raindrops falling at 4 to 6 m s^{-1} .

The vertical profiles labeled 2 which are observed 10 min after profiles 1 are quite similar to profiles 1 above the MB. However, below the MB, velocity profile 2 exhibits greater velocity ($5\text{--}6.5 \text{ m s}^{-1}$) than that observed in profile 1, and also much greater velocity and reflectivity variations with height. Just below the MB layer, the range normalized signal intensity in profile 2 is only slightly higher than that observed in profile 1 at the same altitude (-86.5 dBm to -77.5 dBm instead of -87.0 dBm to -80.5 dBm). However, below the 1.3 km altitude, there is a significant decrease of radar reflectivity. Also, the increase of mean velocity across the MB is appreciably greater ($1.3\text{--}5 \text{ m s}^{-1}$ instead of $1.1\text{--}4.2 \text{ m s}^{-1}$). The greatest difference with respect to profile 1 is the Doppler velocity maximum at an altitude of approximately 1.2 km.

In the absence of significant air vertical velocity, a mean velocity increase must relate to a corresponding increase in particle size and, for Rayleigh scatterers, a radar reflectivity increase. However, inspection of velocity profile 2 indicates that the velocity maximum at 1.2 km is not associated with a corresponding increase of signal intensity. The only rational explanation for this behavior is that scatterers producing the reflectivity maximum are indeed larger, but these particles have a Mie backscattering cross section decreasing with an increase of their size. The altitude at which a weaker signal intensity is observed coincides with a mean Doppler of $5\text{--}6\text{ m s}^{-1}$. This is in agreement with Fig. 9 which shows a decrease of the backscattering cross section S , when particle size increases from 1.3 mm (terminal velocity 5 m s^{-1}) to 1.8 mm (terminal velocity 6 m s^{-1}). There is also a local spectral variance maximum at an altitude of about 1.1 km which may be due to the flattening of the Doppler spectrum associated with a depression in the velocity spectrum center created by the decrease of backscattering cross section for particle sizes between 1 and 2 mm. These preliminary observations of a MB observed with a millimeter wave Doppler illustrate the capability of the radar and also the need for further studies.

Observations were also made inside precipitating thunderstorms at Boulder, Colorado. A thin nylon cover could effectively protect the radar against rain without producing appreciable attenuation of the 94-GHz signal. During the observations only light rainfall occurred, although sparse 4 to 5 mm raindrops could be occasionally observed. Figure 16 shows an example of updraft structures observed on a thunderstorm overhang. The vertical profiles were obtained every 5 seconds and exhibit notable variations of both mean Doppler and signal intensity in the time interval shown. Figure 17 shows the time-height presentation of the updraft event which lasted 2 to 3 minutes (see captions for a discussion of the data).

5. Conclusion

A 3.2-mm wavelength (W-band) is about the shortest wavelength that can be used for a meteorological Doppler radar. Radar components are available off-the-shelf and the sensitivity of the radar for small size hydrometeors is comparable to that of a K_a -band radar. However, the W-band radar has the advantage of reduced size, weight and power requirements. The use of a gridded Klystron oscillator instead of a magnetron also provides a more efficient Doppler system, as the phase noise is considerably reduced. The use of a signal integrator and a high pulse-repetition rate (10 kHz) provides an effective processing gain of approximately 20 dB compared with single pulse data, so that our radar should detect a -50 dBZ cloud reflectivity at three kilometer range and -40 dBZ at 10 km. Radar

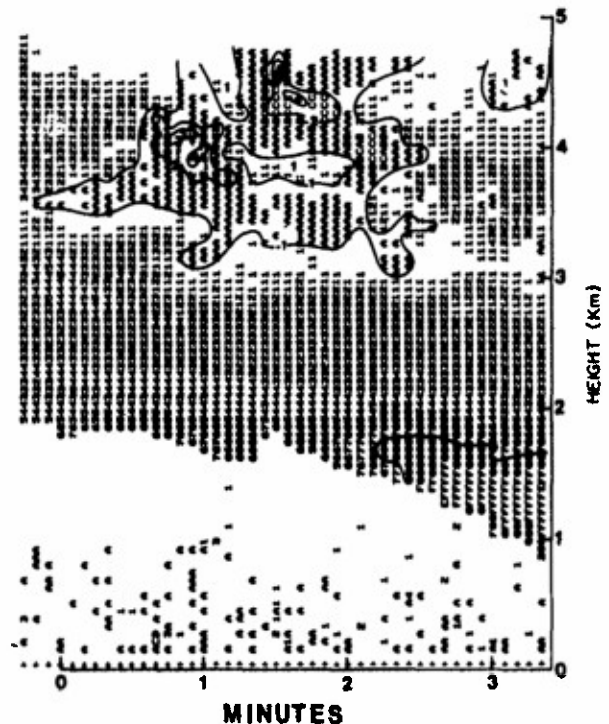


FIG. 16. Time-height presentation of mean Doppler velocity in a thunderstorm outflow. The numbers indicate downward motion in m s^{-1} . The letters indicate upward motion with $A = 1\text{ m s}^{-1}$, $B = 2\text{ m s}^{-1}$, etc. The echoes below the cloud layer are clear air targets showing a primarily upward motion. Note the aliased velocity above 8 m s^{-1} in the bottom right of the figure, $G = 8\text{ m s}^{-1}$, $F = 9\text{ m s}^{-1}$, etc.

sensitivity estimates derived from observations of thunderstorm tops at a range of 15–20 km in high humidity conditions indicate that the radar performance agrees with the radar equation in this paper and the radar characteristics. Also, all cirrus layers are detected and nearly all clouds are above the freezing level. We have a very limited experience in observing fair weather cumulus clouds, which seem to be detected only if their base shows some sign of darkness indicative of their vertical development. This is, however, a very subjective estimate and we are planning more systematic experiments in conjunction with K_a -band and X-band radars and also aircrafts for particle sampling.

Mie backscattering oscillations and their effects on mean Doppler and reflectivity are important at such a short wavelength because the transition from Rayleigh to Mie scatterers occurs for relatively small ($D \sim 0.8\text{ mm}$) particles. At 94 GHz, the equivalent radar reflectivity factor, Z_e , cannot exceed 30 dBZ, even for the highest rainfall rates. At 3-mm wavelength, backscattering maxima occur for 1.1, 2.2 and 3.3 mm diameter raindrops, and backscattering minima for 1.8 and 3.9 mm diameter. The 3-mm wavelength is therefore an attractive choice for multiwavelength-derived drop size

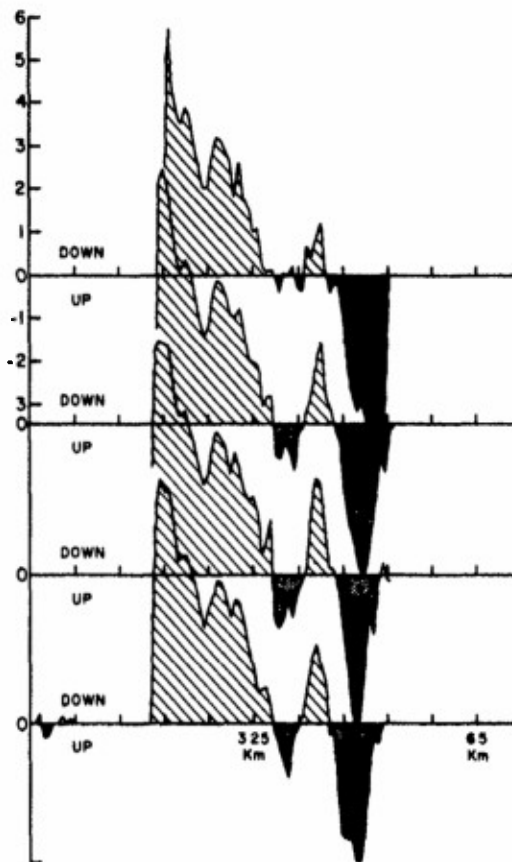


FIG. 17. Selected vertical profiles of mean Doppler through downdraft and updraft regions, observed every 5 seconds.

distribution measurements if the W-band observations are done jointly with K_a and X-band Doppler radars. The drops size distribution can be measured using the complete spectral information available at the three wavelengths with vertically pointing observations. Such a multiwavelength experiment can produce much needed information on raindrop size distribution even in thunderstorms.

Acknowledgments. Dr. Walter Flood's encouragement and constructive review of this work is appreciated. We are also grateful to Dr. R. Serafin, Mr. R. Carbone and Mr. C. Frush for their continuing encouragement and support during the experiments at the National Center for Atmospheric Research. Dr. D. Brown provided the Mie computations. This research

was supported by the Army Research Office, Contract DAAG29-84-0145.

REFERENCES

- Atlas, D., W. G. Harper, F. H. Ludlam and W. C. Macklin, 1960: Radar scatter by large hail. *Quart. J. Roy. Meteor. Soc.*, **86**, 468-479.
- Austin, P. M., and A. C. Bemis, 1950: Quantitative study of the "bright band" in radar precipitation echoes. *J. Meteor.*, **7**, 145-151.
- Hobbs, P. V., N. T. Funk, R. R. Weiss, J. D. Locatelli and K. R. Biswas, 1985: Evaluation of 35-GHz radar for cloud physics research. *J. Atmos. Oceanic Technol.*, **2**(1), 35-48.
- Joss, J., and A. Waldvogel, 1970: Raindrop distributions and Doppler velocities. *Preprints, 14th Conf. on Radar Meteorology*, Boston, Amer. Meteor. Soc., 17-20.
- Lhermitte, R., 1981: Millimeter wave Doppler radar. *Preprints, 20th Conf. on Radar Meteorology*, Boston, Amer. Meteor. Soc., 744-748.
- , and D. Atlas, 1963: Doppler fall speed and particle growth in stratiform precipitation. *Conf. Radar Meteorology*, Boston, Amer. Meteor. Soc., **8**, 297-302.
- , and E. Kessler, 1966: Estimation of the average intensity of precipitation targets. *Preprints, 12th Conf. Radar Meteorology*, Boston, Amer. Meteor. Soc., 23-27.
- , and R. Serafin, 1984: Pulse-to-pulse coherent Doppler sonar signal processing techniques. *J. Atmos. Oceanic Technol.*, **1**(4), 293-308.
- , and C. Frush, 1985: Millimeter wave radar for meteorological observations. *Preprints, 22nd Conf. on Radar Meteorology*, Boston, Amer. Meteor. Soc., 228-231.
- Liebe, H. J., 1985: An updated model for millimeter-wave propagation in moist air. *Radio Sci.*, **20**(5), 1069-1089.
- Marshall, J. S., and W. McK. Palmer, 1948: The distribution of raindrops with size. *J. Meteor.*, **5**, 165-166.
- Pasqualucci, F., B. W. Bartram, R. A. Kropfli and W. R. Moninger, 1983: A millimeter-wavelength dual-polarization Doppler radar. *J. Climate Appl. Meteor.*, **22**, 758-765.
- Ray, P. S., 1972: Broadband complex refractive indices of ice and water. *J. Appl. Optics*, **11**(8), 1836-1843.
- Shimabukuro, F., and E. Epstein, 1970: Attenuation and emission of the atmosphere at 3.3 mm. *IEE Trans. Antennas Propag.*, **AP-1**(4).
- Sirmans, D., 1975: Estimation of spectral density mean and variance by covariance argument techniques. *Preprints 16th Conf on Radar Meteorology*, Boston, Amer. Meteor. Soc., 6-13.
- Srivastava, R. C., A. R. Jameson and P. Hildebrand, 1979: Time computation of mean and variance of Doppler spectra. *J. Appl. Meteor.*, **18**, 189-194.
- Weickman, W. K., 1947: Die Eispähse in der Atmosphäre, Reports and Translations, No. 716, Ministry of Supply (A), Völknerode, 244-247.
- Woodman, R. F., and T. Hagfors, 1969: Methods for measurements of vertical ionospheric motions near the magnetic equator by incoherent scattering. *J. Geophys Res Space Phys.*, **75**, 1205-1212.
- Zrnić, D. S., 1979: Estimation of Spectral Moments for Weather Echoes. *IEEE Trans on Geosci Electron.*, **GE17**(4), 113-128.